National Library of Canada
Acquisitions and Bibliographic Services Branch
395 Wellington Street
Ottawa, Ontario
K1A 0N4

Bibliothèque nationale du Canada
Direction des acquisitions et des services bibliographiques
395, rue Wellington
Ottawa (Ontario)
K1A 0N4

Your file Votre référence

Our file Notre référence

NOTICE

The quality of this microform is heavily dependent upon the quality of the original thesis submitted for microfilming. Every effort has been made to ensure the highest quality of reproduction possible.

If pages are missing, contact the university which granted the degree.

Some pages may have indistinct print especially if the original pages were typed with a poor typewriter ribbon or if the university sent us an inferior photocopy.

Reproduction in full or in part of this microform is governed by the Canadian Copyright Act, R.S.C. 1970, c. C-30, and subsequent amendments.

AVIS

La qualité de cette microforme dépend grandement de la qualité de la thèse soumise au microfilmage. Nous avons tout fait pour assurer une qualité supérieure de reproduction.

S'il manque des pages, veuillez communiquer avec l'université qui a conféré le grade.

La qualité d'impression de certaines pages peut laisser à désirer, surtout si les pages originales ont été dactylographiées à l'aide d'un ruban usé ou si l'université nous a fait parvenir une photocopie de qualité inférieure.

La reproduction, même partielle, de cette microforme est soumise à la Loi canadienne sur le droit d'auteur, SRC 1970, c. C-30, et ses amendements subséquents.

Canada

UNIVERSITY OF ALBERTA

LABORATORY MEASUREMENTS OF ULTRASONIC IMPEDANCES ON CANDIDATE ROCKS ASSOCIATED WITH CRUSTAL SEISMIC REFLECTORS AT GRANITE LAKE, SASKATCHEWAN

by

© JOSEPH B. MOLYNEUX

A THESIS

SUBMITTED TO THE FACULTY OF GRADUATE STUDIES AND RESEARCH IN PARTIAL FULFILLMENT OF THE REQUIREMENTS FOR THE DEGREE OF

MASTERS OF SCIENCE

IN

GEOPHYSICS

DEPARTMENT OF PHYSICS

EDMONTON, ALBERTA

Spring 1994

National Library
of Canada

Acquisitions and
Bibliographic Services Branch

395 Wellington Street
Ottawa, Ontario
K1A 0N4

Bibliothèque nationale
du Canada

Direction des acquisitions et
des services bibliographiques

395, rue Wellington
Ottawa (Ontario)
K1A 0N4

Your file Votre référence

Our file Notre référence

The author has granted an irrevocable non-exclusive licence allowing the National Library of Canada to reproduce, loan, distribute or sell copies of his/her thesis by any means and in any form or format, making this thesis available to interested persons.

L'auteur a accordé une licence irrévocable et non exclusive permettant à la Bibliothèque nationale du Canada de reproduire, prêter, distribuer ou vendre des copies de sa thèse de quelque manière et sous quelque forme que ce soit pour mettre des exemplaires de cette thèse à la disposition des personnes intéressées.

The author retains ownership of the copyright in his/her thesis. Neither the thesis nor substantial extracts from it may be printed or otherwise reproduced without his/her permission.

L'auteur conserve la propriété du droit d'auteur qui protège sa thèse. Ni la thèse ni des extraits substantiels de celle-ci ne doivent être imprimés ou autrement reproduits sans son autorisation.

ISBN 0-612-11290-X

Canada

UNIVERSITY OF ALBERTA

RELEASE FORM

NAME OF AUTHOR: Joseph Benedict Molyneux

TITLE OF THESIS: Laboratory Measurements of Ultrasonic Impedances on Candidate Rocks Associated with Crustal Seismic Reflectors at Granite Lake, Saskatchewan.

DEGREE: Master of Science

YEAR THIS DEGREE GRANTED: 1994

Permission is hereby granted to the University of Alberta Library to reproduce single copies of this thesis and too lend or sell such copies for private, scholarly or scientific research purposes only.

The author reserves all other publication and other rights in association with the copyright in the thesis, and except as herein before provided neither the thesis nor any substantial portion thereof may be printed or otherwise reproduced in any material form whatever without the author's prior written permission.

(Signed)..... J. B. Molyneux .....

Permanent address

Brough farm

Asmall lane, Ormskirk

Lancs., U.K., L40 8JL

Date: 22nd April. 1994

THE UNIVERSITY OF ALBERTA

FACULTY OF GRADUATE STUDIES AND RESEARCH

The undersigned certify that they have read, and recommend to the Faculty of Graduate Studies and Research for acceptance, a thesis entitled **Laboratory Measurements of Ultrasonic Impedances on Candidate Rocks Associated with Crustal Seismic Reflectors at Granite Lake, Saskatchewan** submitted by Joseph B. Molyneux in partial fulfillment of the requirements for the degree of **Master of Science** in **Geophysics**.

Dr. D. R. Schmitt (Supervisor)

Department of Physics

Dr. E. Nyland

Department of Physics

Dr. P. Robertson

Department of Civil Engineering

Dr. T. Chacko

Department of Geology

Date: 14th April 1994

To my parents and family...

ABSTRACT

The section of the Trans-Hudson Lithoprobe reflection line 9 near Granite Lake exhibits a set of three strong seismic reflectors dipping eastwards to depths of over 4 seconds of two way travel time. By extrapolation to the surface it is seen that these reflectors extend into the vicinity of highly sheared metasedimentary zones surrounded by granodiorite plutons. Ultrasonic velocity measurements were carried out on representative rock samples acquired from outcrop along and near to the seismic profile. Eighteen surface samples had ultrasonic velocity measurements performed on up to three orthogonaly oriented cores to pressures of 2000 bar of hydrostatic confinement. Density values of the cores range from 2640 to 2940 kg/m^3, and ultrasonic velocities from 5.7 to 7.1 km/s, with the greatest rock property variations occurring in the metasedimentary layers. The largest impedance changes, which are a measure of the size of a seismic reflector, occur between the metasediment-granodiorite contacts and in the locality of shear zones produced by ductile deformations. These interfaces display reflection coefficients above 0.05. A second observation is that the velocities in samples taken progressively closer to a shear zone, over a 350 meter distance, display a decreasing trend of velocity and impedance values towards the mapped position of the shear zone.

The laboratory constrained vertical extent of the metasedimentary package is 0.23 seconds which correlates well with the 0.22 seconds seen in the seismic data. This suggests that the metasedimentary region is probably the source region of the main seismic reflections with additional complications produced by the shear zones.

ACKNOWLEDGMENTS

I would like to thank the following organizations for there financial support of this project: the Commonwealth Scholarship of Canada (especially Anna Mastelloto), the Lithoprobe Supporting Science Program, Shell Science and Engineering Research Council and the Alberta Oil Sands Technology and Research Authority.

I would also like to thank Dr. T. Evans for use of his drill press, Craig Hickey for doing allot of the preparatory work on this project and Jay Haverstock, Brain Madu and Len Tober for there help in getting the laboratory configuration up and running.

I further would like to acknowledge the extraordinary efforts of my supervisor Doug Schmitt, and the friendship and academic assistance provided by my colleagues: Ahmed Kebaili, Gilbert Dubuc, Yanqun Wang, Yongyi Li, Mike Burianyk and "The Lads" in theory.

TABLE OF CONTENTS

Chapter		Page
1.	INTRODUCTION	1
2.	GEOLOGICAL AND THEORETICAL BACKGROUND	9
	2.1 Continental tectonic setting	9
	2.2 Regional tectonic setting	10
	2.3 Local tectonic setting	11
	2.4 Reflection seismic	12
	2.5 Predominant geological features of the Granite Lake region	13
	2.6 Site positioning	14
	2.7 Reflection coefficients	18
	2.8 Small scale wavelength related phenomena	19
	2.9 Anisotropy	20
	2.10 Seismic resolution	22
3.	EXPERIMENTAL PROCEDURE	28
	3.1 Introduction	28
	3.2 Sample preparation	28
	3.3 Density measurements	32
	3.4 Microcracks	35
	3.5 Laboratory configuration and ultrasonic velocity measurements	39
	3.6 Pressure vessel	42
	3.7 Ultrasonic travel time measurements	44
	3.8 Travel time correction of the end caps	46
	3.9 Resulting velocity-pressure curves	49

3.10 Temperature effects 49

3.11 Mineral point count 51

3.12 Experimental repeatability 52

4. RESULTS 70

4.1 Introduction 70

4.2 Spatial impedance distribution 71

4.3 Velocity, density and mineralogical variations 73

4.4 Formation of reflection coefficient 75

4.5 Description of seismic data 77

4.6 Constraining the metasedimentary reflection package 79

4.7 Introduction to shear zones 82

4.8 Eastern metasedimentary shear zone 83

4.9 Central shear zone 85

4.10 Granite Lake shear zone, and the western pluton 86

4.11 Multiple reflectors 87

4.12 Theoretical interference effects 88

4.13 Interference effects in metasedimentary units 89

4.14 Corrections to measured velocities and impedances 90

4.15 Synthetic seismic 93

5. CONCLUSION 109

BIBLIOGRAPHY 115

APPENDIX 120

LIST OF TABLES

Table		Page
1.	Tectonic history associated with the Granite Lake area	25
2.	Core dimensions	56
3.	Velocty and impedance results	57
4.	End cap callibration history	62
5.	Mineral point count	68
6.	Reflection coefficients at estimated two-way travel times	99
7.	Shear related phenomina	103
8.	Reflections associated with the granodioritic sample 15a	105
9.	Velocity and reflection model	108

LIST OF FIGURES

Figure		Page
1.1	Geologic map of North America (adapted from Hajnal et al. 1993) focusing on a section of the Trans-Hudson Orogen. Lithoprobe seismic lines 9 and 10 are also shown with the test site marked on the eastern end of line 9. NFSZ--Needle Falls shear zone. WB--Wathman batholith. GCT--Guncoat thrust. GCG--Guncoat gneiss (high strain zone). SF--Stanley fault. HSZ--Hartley shear zone. TFZ--Taberner fault zone. PSD--Pelican slide detachment. HLB--Hanson Lake block. SWF--Sturgeon Weir fault. ACF--Annabel Creek fault. Geology beneath Phanerozoic cover is projected with the help of a vertical magnetic gradient map.	5
1.2	Seismic section of Trans-Hudson Lithoprobe data, line 9. Vertical axis display two-way travel time in seconds and the horizontal axis denote the common depth point positions (CDP) spaced 25 meters apart along highway 106. Reflection packets "a", "b" and "c" are marked with "a" being the reflector analyzed in detail.	6

1.3 Detailed geological map of the Granite Lake area (adapted from Ashton et al. 1988). Geological regions are bounded by dot-dash lines, Granite Lake shore by dashed lines, shear zones are denoted by thin solid lines and highway 106 by the thick solid line trending in east-west direction. The metasediments form an "L" structure in the center of the diagram, bounded by granodioritic plutons. To the far left and right of the granodiorites are more metasedimentary units. Rock sample positions are indicated by circled dots and labeled solid squares on the highway represent common depth points (CDP), extrapolated from the seismic sections [figures 1.2 and 4.7]. CDP locations are given for two selected samples as a reference: 7

CDP	LATITUDE	LONGITUDE	ELEVATION (m)
1755	54° 50' 36.55"	102° 30' 52.41"	353.7
1645	54° 51' 43.27"	102° 28' 25.07"	340.4

2.1 Relation of surface samples to depth. The schematic shows a section of the test site with geological units alternately shaded and the surface sample positions denoted by dots. Line (i) represents the path of the reflected sound energy. Line (ii) represents the projection of surface velocities to vertical in order to simulate a wellbore. 26

2.2 Klauder wavelet. Upper and lower frequencies 56 Hz and 12 Hz respectively, with a positive 1000 millisecond time shift and a Rayleigh resolution limit of b/2. 27

3.1 A layered rock sample cut with one set of faces parallel to the foliation plane. Straight solid lines represent foliation planes, or layering of the constituant materials. Lineation is shown from the orientation of long and thin crystals, such as hornblendes, denoted in the diagram by the wavy lines. The lower diagram is cut with no faces parallel to foliation, so no lineation direction can be seen. 53

3.2 Thin section of sample 2. Dark patches indicate hornblende crystals which is the major mineral component. Horizontal width of figure is 2.0 mm . 54

3.3 Thin section of sample 12. Dark grey patches and lighter grey patches indicate hornblende and plagioclase crystals respectively, which are the major mineral components. Horizontal width of figure is 2.0 mm. 55

3.4 Graph to illustrate the effects of micro cracks on physical rock properties such as acoustic velocity. The micro cracked rock is asymptotic to the intrinsic mineral properties at high pressures, at which point the microcracks have substantially closed. 58

3.5 Velocity pressure run of a typical sample. The lower curve is observed during pressurization and the upper curve is observed during depressurization. 59

3.6 Endcap housing of the piezoelectric ceramics. The aluminum mount helps protect the cell from physical damage. With this arrangement the tygon tubing forms a seal around the end cap and the core sample ensuring no hydrostatic confining fluid leaks into the sample. 60

3.7 Schematic cross section of the pressure vessel. Two sealing caps are arranged at either end of the pressure vessel and bolted in place. The transducer feed through wires are displayed in the enlarged circle, with a small notch preventing the wire from blowing out under pressure. The wire is also set in epoxy glue and the feed through is threaded into the main body of the pressure vessel. 61

3.8 End cap calibration. The graph displays travel time data for both pressurization and depressurization. Longer travel times at a given pressure were observed during pressurization. These data are modeled with a second order polynomial of coefficients shown in the legend and with a correlation co-efficient of 0.99591. 62

3.9 End cap calibrations. The legend displays the dates of the calibration runs. 64

3.10 Velocity vs. pressure for three cores. In each case, the lower curve represents pressurization and the upper depressurization. 65

3.11 Temperature measurement. Thermocouple arrangement is set up with copper and constantan wires. The fused wire joint in the pressure vessel moniters temperature by a calibrated relationship with the millivolt reading. A second fused joint is the reference junction maintained at 0 °C by ice water and monitored by a thermometer. 66

3.12 Observed temperatures during pressurization and depressurization. Thermocouple response is shown with readings taken both directly after a pressurization and again three to four minutes later. At 2000 bar pressure the system was left to thermally equilibriate for one hour at constant pressure before depressurization. 67

3.13 Mineralogy of the rock samples, shown in a spatial distribution. Only the major mineral modal percentages are shown, described in the legend and the trends of plagioclase and quartz are clearly marked. Distances are measured along highway 106 relative to the metasediment contact of the east side on the easterly granodiorite. The shaded area represents the metasedimentary band and the dashed lines the shear zones. 69

4.1 Impedance vs. position along the seismic profile. Distances are measured along highway 106 relative to the metasediment contact on the east side of the eastern granodioritic pluton. Solid circles denote cores aligned parallel to foliation, or parallel to foliation and lineation, as in section 3.1.1 . Squares denote cores perpendicular to foliation, and triangles represent cores aligned parallel to foliation yet perpendicular to lineation. The shaded area represents the metasedimentary band and the dashed lines represent the shear zones. Impedance error bars are also shown. 95

4.2 Impedance for core aligned perpendicular to foliation vs. position along seismic profile. Distances are measured along highway 106 relative to the metasediment contact on the east side of the easterly granodioritic pluton. The shaded area represents the metasedimentary band and the dashed lines represent the shear zones. Vertical impedance errors are shown on the labeled cores. 96

4.3 Ultrasonic velocity at 2000 bar vs. bulk density for all the core data. Granodiorites are shown as hollow circles, and metasediments are denoted by solid triangles. Lines of constant impedance are shown as dotted lines. The axes of the ellipses indicate the uncertainties in density and velocity. 97

4.4 Ultrasonic velocity at 2000 bar vs. bulk density for core alligned perpendicular to foliation only. Granodiorites are shown as hollow circles, metasediments are denoted by solid triangles and lines of constant impedance are shown as dotted lines. The axes of the ellipses indicate the uncertainty in density and velocity. 98

4.5 Seismic migration effects. In diagram (i) the solid flag represents the position of a true ray path from source to receiver which is normally incident to the dipping reflection interface. The dashed flag represents the artificial ray path of vertically oriented migrated ray. In diagram (ii), the solid flags have the unmigrated reflection response, corresponding to normally incident rays of (i), which are swept on a radius until they form tangents with the inclinded reflection plane. The dashed flags now display migrated seismic traces, corresponding to the artifical vertical ray paths in (i), at their new migrated lateral offsets. 100

4.6 Schematic of reflector positioning. A velocity profile is shown at increasing values of depth. The '*' denotes the velocity of a given core and the dashed lines show the placement of the reflector mid-way between core positions. The depth axis can be converted to a time scale with the discrete velocity function. 101

4.7 Expanded seismic section. The vertical axis denotes two way travel time in seconds, and the horizontal axis is the common depth point position (CDP) spaced 25 meters apart along highway 106 . The major reflection packet studied in the thesis is denoted as a(i) and a(ii), the near surface and deeper parts of the reflection packet, respectively. The proposed seismic response of the Granite Lake brittle shear zone labeled is "s", and extrapolates to CDP 1850, whereas a(i) extrapolates to a surface position between CDP 1813 and CDP 1748. 102

4.8 Velocities for cores aligned perpendicular to foliation vs. position along seismic profile. Distances are measured along highway 106 relative to the metasediment contact on the east side of the easterly granodioritic pluton. The shaded area represents the metasedimentary band and the dashed lines represent the shear zones. Vertical velocity errors are shown on the labeled cores. 104

4.9 Sythnthetic seismogram I. Klauder wavelet (12 to 56Hz range) convolved with the reflection profile of Table 6. Time graduations in 500 millisecond intervals. 106

4.10 Sythnthetic seismogram II. Klauder wavelet (12 to 56Hz range) convolved with the reflection profile of Table 9. Time graduations in 500 millisecond intervals. 107

GLOSSARY

Accessory mineral: A mineral whose presence in the rock is not essential to the proper classification of the rock, which are generally found in sedimentary rocks as heavy minerals.

Accreted arc: A region between lithospheric plates were new material is deposited.

Allochton: A mass of rock that has been moved a long distance from its place of origin, commonly by tectonic processes.

Alluvial: Deposited by a stream or running water.

Arc Basin: A large troughed segment of the top plate of a subduction zone directly behind the collision zone between two plates.

Arenite: A sedimentary rock formed by more than 50% sand-sized particles.

Asperites: Microscopic defects causing surface roughness.

Amisk: Geologic unit in the region of the Trans-Hudson Orogen of an early Proterozoic age. Volcanics and volcanic derived sedimentation, which was metamorphosed to its present state.

Biotite: Common mineral of the mica group. Black in hand samples and black or green in thin section.

Block faulting: Crustal fracturing into elongated blocks bounded by normal faults.

Breccia: Coarse grained angular clastic rock in a fine matrix or cement.

Cataclastic: Defining a clastic rock whose fragments are the product of fragmentation of a preexisting rock

CDP: Common depth point. A term used in reflection seismology imaging a point on a flat reflector laterally equidistant from a seismic source and receiver.

Clastic: Defining a rock consisting of fragments from preceding rock or rocks.

Clinopyroxene: Calcium rich mineral of the pyroxene family

D1 to D7: Geologic classification of tectonic regimes unique to the Trans-Hudson Orogen, in chronological order of decreasing age from 1 to 7.

Dextral: Relative clockwise motion between two geologic plates.

Diorite: Plutonic rock of low quartz and feldspar content but high plagioclase amounts.

Fanglomerate: Cemented deposits of alluvial fan.

Feldspar: Mineral of K or Na-Ca Al-silicates.

Garnet: Any mineral from the group of high-grade (high temperature and pressure) metamorphic Ca, Al, Fe, Cr, and V silicates of the general formula $X(SiO_4)_3$ where X = Fe_3Al_2, Ca_3Fe_2 etc. Displays a glass like luster and has no cleavage planes.

Gneiss: Foliated rock formed by regional metamorphism, generally with less than 50% minerals showing a preferred orientation.

Granodiorite: Plutonic rock consisting mainly of quartz, feldspar and high plagioclase levels.

Hornblende: The most common amphibole mineral: $(Ca,Na)_{2-3}$ $(Mg,Fe,Al)_5$ $(Si,Al)_8$ $.O_{22}(OH)_2$, occurring in columnar, fibrous, or granular form.

Intercalated: layered material that exists between other layered material.

Island arcs: Volcanic derived elevated body on the top plate of a subducting zone

Isoclinal: Describes a fold with parallel limbs.

Laurasia: The late Paleozoic, northern supercontinent, including North America and Eurasia, that separated from another supercontinent, the Gondwana, in the Triassic period (225-190 Ma)

Left Lateral fault: A fault which a block appears to have moved to the left when viewed from the opposite block.

Metasediment: Sedimentary rock that has been subject to metamorphism.

Missi: Geologic unit in the region of the Trans-Hudson Orogen of an early Proterozoic age. Erosional sedimentary deposits that have been metamorphosed.

Mylonite: A microbrecciated rock exhibiting shearing flow structures and is a product of intense shear metamorphism.

Orogen: A linear or bowed structure that has been subject to folding and other deformation processes, generally forming mountain belts.

Pluton: An intrusion of igneous rock of granitoid texture.

Polymictic: Clastic sediment composed of different minerals

Proterozoic: A geologic time period being the more recent of the two great divisions of the Precambrian (2.7 - 0.59 Ga), cf. **paleo**- old, ancient.

Sillimanite: Mineral formed at high temperature and pressure, of the form Al_2SiO_5, occurring as long, slender crystals.

Terminal collision: The conclusion of plate motion whereby plates are locked. However, stress fields may still pervade.

Tonalite: Plutonic rock, rich in plagioclase, and poor in alkali feldspar

Turbidite: A sedimentary rock of bed structures with graded levels of clast size, formed by deposits from sediment laden water.

TWTT: Two way travel time. Refers to the time for a seismic signal to travel from the surface to a buried reflector and back again to the surface.

Wacke: Rock fabric indicator denoting a poorly sorted sandstone, rich in chemically unstable mineral grains and rock fragments in an abundant matrix of silt and clay.

CHAPTER 1

Introduction

The relationship between the elastic wave properties of surface rock samples and the reflection character observed in a seismic reflection profile of the Trans-Hudson Orogen Lithoprobe transect is studied in this thesis. Seismic reflections are a consequence of variations in elastic wave impedances. With experimental data of this impedance structure derived from surface rock samples it is possible, in principle, to determine the cause of seismic reflectors and thereby assist in the geologic interpretation of these reflectors. In the absence of a continuous record of the impedance variations with depth, the physical properties of the rocks were sampled in comparatively sparse manner at outcrop. This approach has many disadvantages related to the amount of the available representative rock sampling acquired,but can provide a preliminary examination. In the present study the ultrasonic velocities and densities of rock samples taken from regions of ductile and brittle shear zones in the crust provide an indication of how seismic velocities are affected by such shearing phenomena compared to those of surrounding relatively unsheared media. The results indicate that seismic velocities are lower than normal very close to the shear zone, and this could produce the observed seismic reflections.

As part of the Trans-Hudson Orogen Lithoprobe Transect, a reflection seismic profile was acquired over 300 km of highway centered approximately on the town of Flin-Flon, Manitoba [figure 1.1] . The record from this profile (denoted as line 9) displays reflection data to 16 seconds of two way travel time (TWTT). A set of three strong parallel reflectors are observed which extend to over 4 seconds TWTT. These structures dip gently eastwards and when extrapolated to the surface project to a region which consists of a banded metasedimentary unit bounded on either side by two granodiorite plutons and is located approximately 35 km west of Flin-Flon, Manitoba near Granite

Lake, Saskatchewan. The present study concentrates on the central and most prominent reflector hereafter referred to as the Granite Lake reflector and is denoted as "a" in figure 1.2 . In geologic maps of the area there are three shear zones mapped. The two most easterly are primarily ductile zones formed by the "plastic deformation" of the rocks and are located within the metasediments which strike nearly perpendicular to the seismic profile. The third is a brittle shear zone, formed by brittle fracturing of rock under intensive shear, and lies entirely within the western granodioritic pluton shown in figure 1.3.

To make measurements of the impedance, rock samples were collected from outcrop along the highway in the locality of the metasediments and the surrounding plutons. Ultrasonic compressional velocity measurements were carried out on these samples subject to confining pressures of up to 2000 bar which corresponds to overburden pressures expected at 7-8 km depth. By measuring the dimensions and mass of the actual test rock the calculation of the rock's bulk densities can be evaluated. In unfractured, dry, low porosity crystalline rock the two most important properties governing seismic reflectivity are the rock's velocity and mass density. The product of these parameters is referred to as the elastic wave impedance of the rock; differences in this impedance control the strength of a reflection. As a result, the depths at which there are large impedance contrasts will correspond to large reflection coefficients and should highlight prominent reflectors seen in the seismic section. By a comparison of the variations of the physical properties of the surface samples, the larger scale geologic features can be related to the seismic reflection data.

The area of study is an area of much geologic interest. Regionally, the test site is situated in the Trans-Hudson Orogen (THO) [figure 1.1], which is a large area of compressionaly deformed metamorphic and igneous rocks spanning over 1500 kilometers of central and northern America in a north-south direction. This zone of folding and shear deformation bounds the Hearne and Wyoming provinces on its west, and the Superior

province on its east [figure 1.1]. The rocks in the THO were metamorphosed in the early Proterozoic, and in particular have been dated at 1.91 - 1.85 Ga. years old (Ga. = 10^9 years previous) at the test site; a complete description of the geologic and tectonic history is given in chapter 2.

The 7 by 10 km area of study is located at a bend in a series of locally "L" shaped metasedimentary layers. The metasediments and the surrounding plutons trend in a north-south manner directly north of the study area, and in an east-west direction east of the study area. However, the locally northeast-southwest trending seismic profile intersects nearly perpendicular to the trend of the geologic layers indicating that the reflections seen in the seismic are from the same plane as the geologic structures and are not from reflections out of the plane of the two dimensional seismic profile.

In chapter 3 the experimental procedure to obtain the ultrasonic compressional wave velocities and the rock impedances is described. Ultrasonic velocity measurements were developed to a reproducibility of better than 2%. In the measurements, a piezoelectric ceramic produces a 1 MHz compressional ultrasonic pulse that propagates through the sample to be received by a second ceramic. The velocities were then determined from the 'time of flight' of the transmitted pulse and from the length of the sample. Hydrostatic confining pressures of up to 2000 bar were applied during velocity measurements by a hand operated pump connected to a steel pressure vessel of 3.9 cm internal diameter and 19.0 cm internal length.

Chapter 4 presents the results of the experimental data and discusses the errors involved with the experimental configuration and technique. In the analysis three possible causes of the seismic reflection arise as determined from variations in the impedance distribution of the rock samples along the profile. First, the granodiorite-metasediment boundary may have local differences in mineralogy to cause a large variation in both velocity and density producing reflection coefficients as high as 0.05 . Such a strong reflection coefficient would explain the reflector "a" seen in the seismic [figure 1.2].

Alternatively, two ductile shear zones transect the metasediments and there is some evidence in the results that these intense deformations may have affected the intrinsic elastic properties which would also result in an impedance anomaly causing a reflection. A final source of the reflections are tuning effects associated with the parallel layered structure of the metasediments of appropriate widths and impedance contrasts to exhibit multiple reflections and interference effects.

Chapter 5 amalgamates all the previous points mentioned and discusses the relative confidence of the differing suggested ideas for the cause of the seismic reflector. Additionally, further improvements and suggested follow up works are discussed in this section.

Relatively little work has been performed on the rock properties of shear zones. However, there is now an apparent surge of research activity in this area: see Jones & Nur (1982), Christensen and Szymanski (1988), Burke & Fountain (1989), Mainprice & Casey (1990), Fountain (1993), Rey et al. (1993), Fountain et al. (1993).

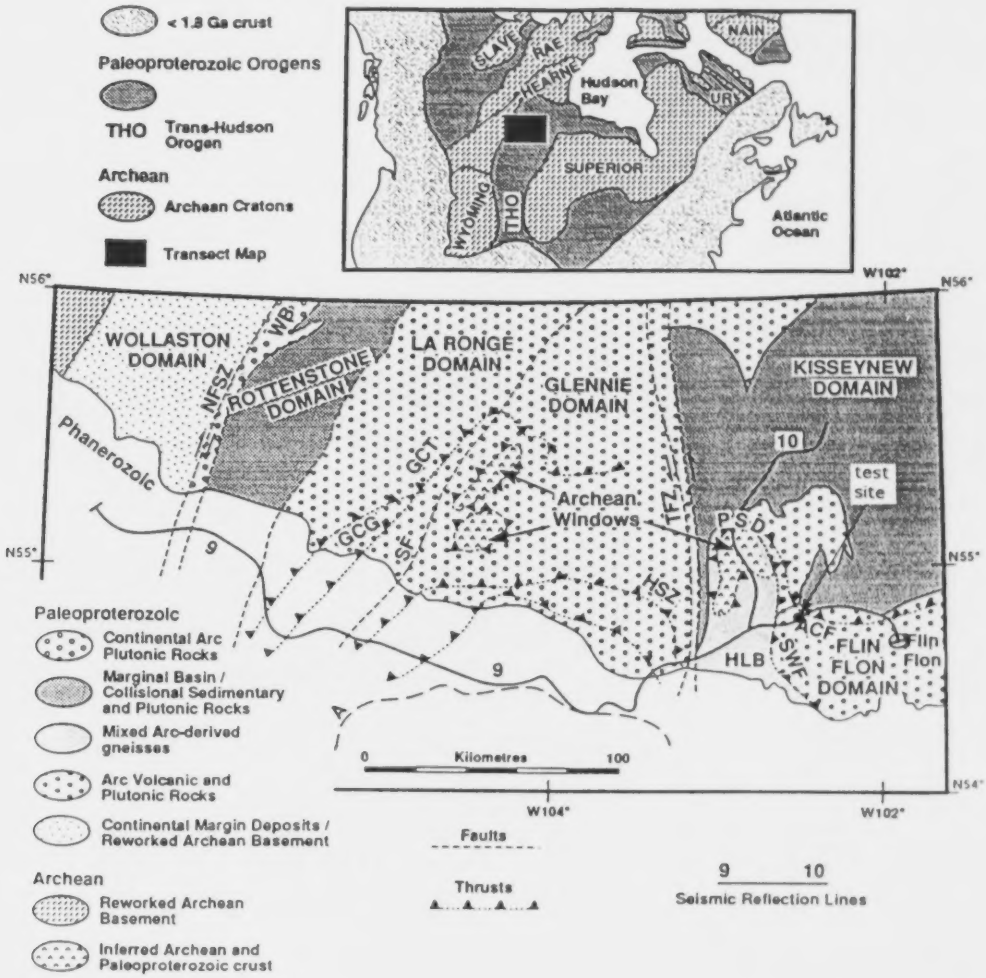

Figure 1.1 . Geologic map of North America (adapted from Hajnal et al. 1994) focusing on a section of the Trans-Hudson Orogen. Lithoprobe seismic lines 9 and 10 are also shown with the test site marked on the eastern end of line 9. NFSZ--Needle Falls shear zone. WB--Wathman batholith. GCT--Guncoat thrust. GCG--Guncoat gneiss (high strain zone). SF--Stanley fault. HSZ--Hartley shear zone. TFZ--Taberner fault zone. PSD--Pelican slide detachment. HLB--Hanson Lake block. SWF--Sturgeon Weir fault. ACF--Annabel Creek fault. Geology beneath Phanerozoic cover is projected with the help of a vertical magnetic gradient map.

Figure 1.2 . Seismic section of Trans-Hudson Lithoprobe data, line 9. Vertical axis display two-way travel time in seconds and the horizontal axis denote the common depth point positions (CDP) spaced 25 metres apart along highway 106. Reflection packets "a", "b" and "c" are marked with "a" being the reflector analyzed in detail.

Figure 1.3 . Detailed geological map of the Granite Lake area (adapted from Ashton et al. 1988). Geological regions are bounded by dot-dash lines, Granite Lake shore by dashed lines, shear zones are denoted by thin solid lines and highway 106 by the thick solid line trending in east-west direction. The metasediments form an "L" structure in the center of the diagram, bounded by granodioritic plutons. To the far left and right of the granodiorites are more metasedimentary units. Rock sample positions are indicated by circled dots and labeled solid squares on the highway represent common depth points (CDP), extrapolated from the seismic sections [figures 1.2 and 4.7]. CDP locations are given for two selected samples as a reference:

CDP	LATITUDE	LONGITUDE	ELEVATION (m)
1755	54° 50' 36.55"	102° 30' 52.41"	353.7
1645	54° 51' 43.27"	102° 28' 25.07"	340.4

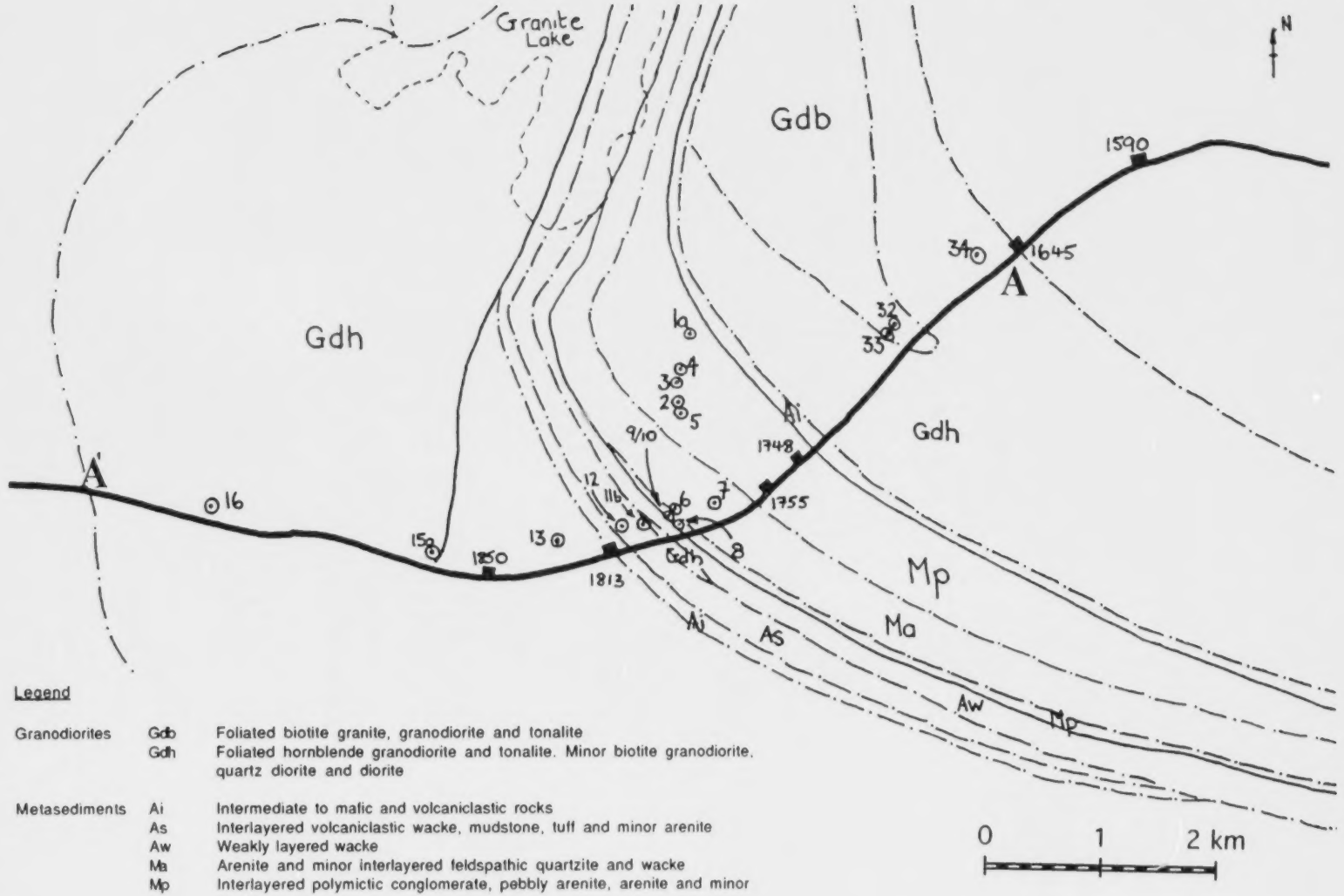

Legend

Granodiorites	Gdb	Foliated biotite granite, granodiorite and tonalite
	Gdh	Foliated hornblende granodiorite and tonalite. Minor biotite granodiorite, quartz diorite and diorite
Metasediments	Ai	Intermediate to mafic and volcaniclastic rocks
	As	Interlayered volcaniclastic wacke, mudstone, tuff and minor arenite
	Aw	Weakly layered wacke
	Ma	Arenite and minor interlayered feldspathic quartzite and wacke
	Mp	Interlayered polymictic conglomerate, pebbly arenite, arenite and minor wacke

CHAPTER 2

Geological and Theoretical Background

2.1 Continental tectonic setting

The Trans-Hudson Orogen (THO) is a tectonic feature of the Canadian shield which separates the Wyoming and Hearne provinces from the Superior provinces as shown in figure 1.1 . These surrounding provinces are all of Archean age (>2.5 Ga.) whereas the THO displays younger rocks of an early Proterozoic age, between 2.5 and 1.6 Ga. (1 Ga. = 10^9 years ago), as described in Hoffman (1989).

The reader should note that there is a glossary of geologic and technical terms at the start of this thesis.

The Ungava segment of the orogen in northern Quebec to the far north west of the Kisseynew domain displays U-Pb zircon dating that suggests oceanic rifting occured around 2.1-2.0 Ga [Lewrey (1993)]. At this time, and throughout much of the Proterozoic, most of what is now the northern end of the east-west striking THO [figure 1.1] would have been submerged beneath the present day Hudson Bay Basin which was a vast sea like expanse during the Proterozoic [Hoffman (1989)]. Indeed, most of the sedimentation mentioned in the following geologic history is derived in association with the marine environment of this large sea like area. Terminal collision of the accreted arcs in the THO between the relatively northward trending Superior province, with respect to the Hearne province, probably occurred between 1.83 and 1.79 Ga. [Lewrey (1993)] with post collision deformation occurring between 1.79 and 1.72 Ga.

2.2 Regional tectonic setting

Arc magmatism in the general region of the transect began around 1.9 Ga. as described by Hajnal (1994) and is presumably associated with the collision events of the Superior craton with the Hearne and Rae provinces, described later as the D3 to D7 collision events. Recent U-Pb zircon dating [Hoffman (1988)] showed the earliest volcanism at 1.91 Ga. in the location of Lynn Lake [figure 1.1] followed by later periods of volcanism in the La Ronge, Glennie Lake, Hanson Lake, and Flin Flon Belts. Plutonism occurred throughout the region between 1.88 and 1.83 Ga. with partial remelting of the Kisseynew gneiss belt between 1.82-1.81 Ga. This plutonism is broadly coeval with marine-continental sedimentation of unsorted coarse grained material (conglomerates) in association with the postorogenic sedimentary filling of the marginal basin centered in the Kisseynew domain [Lucas (1993)]. Hoffman (1988), suggests that volcanic "Amisk" rocks and related plutonism occurred at the same time as the turbiditic sedimentation from the edge of a continental shelf. These sediments in turn were overlain 60-70 Ma later by low energy alluvial "Missi" fanglomerates 1.83 Ga., [Hoffman (1988)] where fanglomerates describe the sedimentary deposits produced by the deposition from a narrow river valley into a broad plain or basin presumably of the Hudson Bay Basin in this case.

In summary, the main structural processes involved in the formation of the present regional geologic structure are in chronological order as follows: 1) oceanic rifting and sea floor spreading, 2) subduction of oceanic plates in a north-south manner with associated accretion of small volcanic islands onto the continent, 3) deformation of the hot rock by the generally north-south compressional regimes, and associated plutonism (huge volumes of hot magmatic material rising like bubbles through the more dense crustal rock and cooling to form homogeneous granitic rocks).

2.3 Local tectonic setting

The region of interest in this study is located within the THO and hereafter will be referred to as the Granite Lake region [figure 1.3]. Within the Granite Lake study region, the rocks were derived from ancient island arcs and metamorphosed sedimentary terrains of ages between 1.91 and 1.85 Ga. The volcanic Amisk and the alluvial Missi make up the bulk of the metasediments of the Granite Lake region. While the Missi rocks were being deposited, it is believed that the Flin-Flon belt was elevated as a consequence of lithospheric flexure of the island arc land mass between the converging plates of the Superior province with the Hearne. With this topography supplying a source of the sediments the Missi group of rocks is formed from a series of river deposits into the Hudson basin which is seen in the present day structure of the overlaying volcanic Amisk.

Various tectonic folding phases evident in the rocks within the Granite Lake region are referred to chronologically as D1 through D7 by Reilly et al. (1993). In identifying the tectonic phases it is difficult to describe each event precisely, as subsequent tectonic events superimpose on the older rock fabrics to varying degrees. Most of the major folding occurred during the volcanic phase that produced the Amisk rocks and the subsequent cooling period during which time the sedimentary Missi group was deposited. Ductile deformations are pervasive through much of the tectonic history of the Amisk and Missi formation as all rock was relatively hot. Indeed, the local metamorphism temperatures were approximately 550° C [Gordon et al. (1993)] and rocks within such temperature environments are no longer brittle but deform ductily under the influence of shear stress [Rey et al. (1993)].

The deformation histories identified by Reilly et al. (1993), and Ashton (1993) are shown in Table 1. Both histories use slightly different geologic chronology labeling schemes but Table 1 relies on that of Reilly et al. (1993).

2.4 Reflection seismic

The portion of the east-west trending Lithoprobe THO transect reflection profile line 9 shown in figure 1.2 (presently unpublished seismic data reprocessed by Bezdan and Hajnal (1993)) is the motivation for the present study. The study seeks to constrain the source and position of the strong eastward dipping reflections seen to project to the surface between common depth points 1600 to 2000 with laboratory derived impedances of surface rock samples. The seismic acquisition parameters are described by Lucas (1993). Briefly, four vibrator trucks swept 8 times at a given shot point with a 14 second linear upsweep from 12 - 56 Hz (the reader is referred to Yilmaz (1993) for a description of this process). The seismic data was acquired with a 240-channel telemetry acquisition system of a 50 m geophone group spacing, and a 100 m source group spacing. The seismic profile shown in figure 1.2 was migrated assuming a constant velocity of 6 km/s.

One of the striking features of the reflection profile is a set of three parallel coherent reflectors dipping gently to the east to depths of over 4 seconds two way travel time in figure 1.2 . The central reflector of the three is denoted as "a", and is the target of our investigation and this extrapolates to common depth point (CDP) 1800 at the surface in figure 1.2. This point is 35 km west of Flin Flon along highway 106 and lies 2 kilometers to the south of Granite Lake [figure 1.3]. The surface geology in this region consists of granodiorite-metasediment contacts, ductile shear zones, and brittle shear zones. The two other reflectors seen in the seismic, "b" and "c", are each laterally displaced from the central one by approximately 5 km, and these also appear to extrapolate into the vicinity of other metasediment-granodiorite boundaries. However, the seismic line geometry for these cases are not as straightforward as for reflector "a".

2.5 Predominant geological features of the Granite Lake region

The main geologic regions of the test site and the sample locations are shown in the geologic mapping of Ken Ashton and coworkers [Ashton et al. (1988)] in figure 1.3 . The main geologic features are two granodioritic plutons which surround a central belt of broadly defined metasediments. These metasediments consist of both the volcanic Amisk and the sedimentary Missi groups which were both deformed by the D1 to D7 tectonic events described earlier. The full geologic map of Ashton et al. (1988) show that the planes of foliation generally dip towards the northeast in a direction perpendicular to the northwest strike of the metasediments. The seismic profile at this point is generally northeast-southwest and intersects the metasediments below the corner of the 'L' shaped metasedimentary belt. We assume that the foliation planes in the rock fabrics are associated with the folding and shearing of the D3 to D6 events, and as such all the geological features studied in the metasediments are parallel to foliation. Indeed, the foliation dip angle with respect to horizontal in this region varies between 20 and 45° and this is consistent with the 22° dip of the reflectors calculated from the seismic section [figure 1.2]. As a result, if the structures observed in the seismic profiles follow the geologic foliation trends then the seismic line near Granite Lake is nearly perpendicular to the strike of these trends. It was this coincidence of the orientation of the seismic line with that of the geological structure, together with the relatively good outcrop exposure which motivated sampling at the Granite Lake section of the seismic profile.

Further, two ductile shear zones lie within, and strike parallel to the metasedimentary band. It is presumed that whatever caused the stress field aligning the foliation planes during folding and other deformational regimes also produced the shear zones. Indeed, these ductile shear zones were presumably formed at weak points in the sedimentary layers [personal communication, Ashton (1994)]. On a broad scale these shear zones appear in outcrop to be a few tens of meters wide measured perpendicular to

the strike of the metasedimentary bands. In the rock fabric, the shear zones are distinguished by stretching of the mineral crystals and by a decrease in the mineral size with proximity to the shear zone, such as described in Rey et al. (1993). Larger scale observations show that the clastic features become stretched under increasing shear regimes. However, it is difficult to discern the true mappable horizontal extent of the shearing seen at the surface due to the lack of continuous outcrop in this region.

A third shear zone lies one kilometer from the west edge of the metasediments and is referred to as the Granite Lake shear zone. It trends nearly north-south in contrast to the generally northwest-southeast trending shear zones located in the metasedimentary layers. The Granite Lake shear zone, however, was produced by a more brittle deformation of the rocks at relatively low temperatures around 250° C [personal communication, Ashton (1994)] late in the Proterozoic geologic history of the region. On initial formation of the brittle fault zone, fluids presumably permeated through the broken structure and deposited calcite and quartz into cataclastic fault zone material. Such veins are indeed apparent in this shear zone in addition to a left lateral displacement which is indicative of a brittle shearing event.

2.6 Site positioning

It is important to describe how sampling the physical properties of surface samples might correspond to the response of dipping geologic structures indicated in both seismic data and from geologic mapping. The geologic interfaces dip gently to the northeast in our section due to the D3 tectonic event [Table 1]. If these geologic interfaces remain continuous at depth, then by measuring the pressure-velocity response of the surface rock in a specific geologic layer one can theoretically extrapolate this material property to obtain the velocity at depth. This geometry is described in figure 2.1 whereby the

ultrasonic velocities measured on the surface samples are taken to represent the velocity down into the earth along structural dipping structures. As a result the vertical velocity function at a given point is the projection of the measured velocities down the dip of the layer to the vertical at the surface point discussed. This simulates the velocities that might be measured along a hypothetical vertical borehole and this information is useful in modeling the seismic response later in chapter 4. A second important point to be remembered is that the seismic rays imaging the dipping structural features have traveled along a path perpendicular to the dip but are plotted in a vertical manner at the point they were recorded in a seismic trace. Consequently, a representative seismic profile requires that the seismic data be migrated [Yilmaz (1993)]. Regardless, in the analysis of the laboratory seismic data it is expected that those cores aligned perpendicular to the dipping foliation planes will also parallel the direction that the seismic wavelets traveled. As a result, those core cut perpendicular to foliation will be most representative of the actual seismic velocities and hence will be of most use in the interpretation of the seismic profile in figure 1.2 .

The process of choosing appropriate rock samples in the field is governed by a series of compromises. Ideally, one would like to obtain a continuous data set displaying the variations in the velocities and densities of the rocks through the earth perpendicular to the orientation of the reflector. The real situation required sampling from surface outcrop which was relatively sparse, and in many cases difficult to access.

Sampling occurred along and near highway 106 which coincides with the seismic reflection data acquisition line. From east to west the surface geology varies from a granodioritic pluton then through a band of metasediments and finally into another granodioritic pluton [figure 1.3]. It was noted that the reflector appeared to spatially correlate with the mapped position of the metasediments. As the pluton appeared homogeneous it was felt that dense sampling of the surrounding granodiorites would not be as productive as more intensive sampling of the complex metasediments. Indeed, in

each granodiorite only three locations were sampled in contrast to the 12 locations within the metasediments. Generally the rocks classed as the granodioritic plutons correspond to Gdh regions labeled in figure 1.3. These granodiorite bodies are large, up to 5 km wide and extend for tens of kilometers perpendicular to highway 106. These light gray rocks appear relatively uniform in modal composition and have a granular texture. However, the more easterly pluton contains a substantial region of Gdb in which the rock is slightly darker in color than the other rocks in this locality and are classified as foliated biotite granites, granodiorites and tonalities [figure 1.3]. The region of this "Gdb" rock is sufficiently large and continuous such that it was considered to be a potential reflector in the seismic profile.

The relatively dark fine grained metasediments consist of many geologic bands which extend along strike for more than 5 km perpendicular to the seismic profile. The following description of the differing metasedimentary units along highway 106 from west to east is taken from Ashton et al. (1988) in figure 3:

(i) *Ai*: intermediate to mafic volcanic volcaniclastics.

(ii) *As*: interlayered volcaniclastic wacke mudstone and tuff and minor amounts of arenite (i.e. more than 50 % sand sized particles).

(iii) *Gdh*: Foliated hornblende granodiorite and tonalite. This specific body extends less than 500 m perpendicular to the profile.

(iv) *Aw*: Weakly layered wacke.

(v) *Mp*: Interlayered polymictic (clasts of various mineralogy) conglomerate, and finally pebbly arenite, arenite & minor wacke.

(vi) *Ma*: Arenite and minor interlayered feldspathic quartzite & wacke.

(vii) *Mp*: similar to (v).

(viii) *Ai* similar to (i).

Classifications (i)-(iv) are of the Amisk group, except for the small *island* of Gdh hornblende granodiorite, referred to as (iii) above. The remaining metasediments are generally from the Missi group except for a small band approximately 100 m wide of Ai (viii) and Mp (vii) rocks which appear misplaced in the stratigraphic sequence as the Amisk is over 60 Ma. older than the normally overlying rocks of the Missi group. This could be due to the folding process of tectonic events which caused the original sediment deposits to be overturned.

The relative positions of the sample sites are accurate with respect to the map and with the exact positioning performed by GPS (Global Positioning System) which is optimally accurate to a few tens of meters. Somewhat naively, the sampling collection was performed under the assumption that there would be strikingly obvious rock variations in the field that corresponded exactly to the geologic map of Ashton et al. (1988). However, it was difficult to discern to the untrained eye which geologic unit was being sampled as the metasediments were often very similar in bulk appearance.

The geologic map of figure 1.3 is not "pin point" accurate but it is an interpreted extrapolation of the various rock types expected between the various outcrops that the mapping geologist discovered. As a result, the geologic map is developed not only from a simple plotting of the locations at which the various rocks types are formed but also includes substantial interpretation based on the geologist's experience. Generally, the geologic regions are accurately delineated in figure 1.3 with respect to highway 106, where outcrop is easily accessible and fresh outcrops are exposed as a product of road construction [personal communication, Ashton (1993)]. As a result, those samples taken near the road are accurately placed in their specific geologic zones to within the accuracy of the GPS. The rest of the geologic map is less well constrained as the geologic map is an extrapolation of isolated contacts found in the heavily bush covered area.

Accepting this sampling limitation, we attempted to obtain as many metasedimentary samples from as many metasedimentary units as possible. Not all the

geologic bands, seen in figure 1.3, were visible by the side of highway 106 and also many of the samples that were collected came from outcrop a few meters or less in dimension. However, all the larger geologic zones were sampled at least once. Interestingly, in the largest metasediment band five samples were taken at approximately 50 m interval spacings progressively closer to the easternmost shear zone and these may show a trend in the velocity and impedance response of the rock associated with the shear zone.

2.7 Reflection coefficients

The reflection of a compressional wave by a geologic interface is usually assumed to be described by the simple conventional model [Yilmaz (1993)], in which seismic rays are both reflected and transmitted by an abrupt change in seismic impedance. The seismic impedance, I, for a given rock type is equal to the product of its density and wave velocity. At an interface between two rock types of differing impedances, the amplitude of the normally reflected wave is given by the well known reflection coefficient R assuming normal vertical incidence:

$$R = \frac{I_2 - I_1}{I_2 + I_1} \qquad (1)$$

where the two layers have impedances I_1 and I_2, and the wave is initially in layer 1. It must be noted that the I_1 and I_2 values described here only apply as long as the seismic wave is perpendicularly incident on the impedance contact; the reflection coefficient is more difficult to describe if the wave is incident at any other angle.

By measuring the acoustic impedances of cored rock samples taken from the surface one can map out the acoustic impedances of the rocks at depth. This approach has been taken by several authors such as Christensen and Szymanski (1988) and Fountain

(1993) in a variety of geologic regions. One can then look at the impedance profile and estimate the reflection coefficients at depth related times. The larger the impedance contrast the larger the reflection coefficient.

Using the largest reflection coefficients, which produce the strongest reflections, the seismic profile may be modeled by convolving an assumed input wavelet from the shot site with the impedance relationship in terms of the time it takes a seismic wave to travel to the reflector and return. Mathematically, this is described by:

$$O(t) = R(t) * W(t) \tag{2}$$

where R(t) is the normalized reflection coefficient profile in time, W(t) is the assumed input seismic source pulse, O(t) is the observed synthetic seismogram, and "*" denotes the convolution operation [Yilmaz (1993)].

2.8 Small scale wavelength related phenomena

Ultrasonic measurements are performed on test core samples at very different frequency than that of the reflected seismic waves. Seismic wavelets tends to have dominant frequencies below 200 Hz, whereas ultrasonic measurements are typically in the range of 75 - 3000 kHz [ASTM standards (1993)]. The characteristic wavelength of input source is simply derived from dividing the velocity of the propagating media by the dominant frequency of the transmitted pulse. For seismic input pulses the wavelengths are tens of meters, in contrast to the subcentimeter wavelengths for a crystals oscillating in the MHz range. Indeed for the 1 MHz crystals used in our experimental set up, and with sample velocities ranging from 5.7 to 6.9 km/s, the characteristic wavelength vary between about 5.7 and 6.9 millimeters.

With coarse grained rock the ultrasonic pulses may scatter from the grains and degrade (i.e. attenuate) the received signal. This effect is noticeable when the size of the rock matrix minerals become comparable to the characteristic wavelength of the input source. For wavelengths much larger than the crustal grains, the transmitted pulse is essentially transparent to the individual grain component contacts and travels through the sample at some average velocity. Therefore when choosing an ultrasonic source one must evaluate what frequency of crystal to use to produce a wavelength of appropriate length. In our experiment the characteristic wavelength was on average 6 mm which was generally amply larger than the millimeter and sub-millimeter average grain size in the rock samples tested.

2.9 Anisotropy

The Websters American Dictionary defines anisotropy as: "exhibiting properties with different values when measured along axes in different directions". In the present study compressional wave velocities are measured in up to three orthogonal planes, and hence the velocity anisotropy of the rock samples can be measured. This is particularly important for foliated and lineated metamorphic rocks whose texture consists of oriented mineral grains with the minerals themselves being highly anisotropic. Birch (1960, 1961) did much of the pioneering work in this area of ultrasonic rock velocity measurements building on the very early work of Zisman (1933b) and others. Velocity anisotropy shall be defined for purposes of this study as:

$$\text{Velocity anisotropy} = \frac{1}{2}\left(\frac{V_{max}-V_{min}}{V_{max}+V_{min}}\right)100\% \qquad (3)$$

where V_{max} and V_{min} are the maximum and minimum velocities measured in different orientations on the rock sample. In a similar manner the impedance anisotropy may be defined as:

$$\text{Impedance anisotropy} = \frac{1}{2}\left(\frac{I_{max}-I_{min}}{I_{max}+I_{min}}\right)100\% \qquad (4)$$

where I_{max} and I_{min} are the maximum and minimum impedances.

Anisotropic effects are somewhat related to the wavelength of the propagating elastic wave energy. At wavelengths of the grain scale the wavelet travels along the fastest path through the higher velocity grains according to Fermat's principle. Therefore, in the case of a foliated sample of alternately layered "fast" and "slow" material with the input ultrasonic signal receiver configuration along the foliation axis the first arrival energy would propagate through the "fast" medium. However, if the signal were transmitted perpendicular to foliation the signal would pass through alternate layers of "fast" and "slow" material and thus the sample would show a lower aggregate velocity than the previous case and so a comparison between these two propagation directions would indicate velocity anisotropy.

2.10 Seismic resolution

It is possible that impedance interfaces may be so closely spaced that the reflected wavelets in a seismic trace cannot be discerned as separate reflection events. What follows is a brief discussion of the background describing the various limits of this spatial resolution phenomena and the applications to seismic investigations.

This resolution problem was first addressed by Lord Rayleigh and is described in Kallweit and Wood (1982), who looked at the diffraction effect of light passing through an optical aperture which was imaged on a distant screen. The resulting diffracted light, rather than being sharply defined has a more diffuse intensity distribution described by a sinc function. When two such apertures (or slits) are placed side by side and are illuminated, and the resulting intensity distribution pattern is noted. The Rayleigh criterion of resolution, which was derived from this experiment, suggests that two separate light beams are indistinguishable from one another if they are separated by less than the peak to trough separation of the sinc function. At this point the two wavelets appear as one singular peaked feature with this defined separation called the Rayleigh criterion of resolution. Seismic responses are governed by similar criterion with the added complication that the seismic wavelets also have negative displacement, compared to the completely positive intensity distribution caused by the diffracted wavelets. In this seismic case an identical Rayleigh separation shows two *barely* discernible peaked structures.

The Ricker limit [Ricker (1953)] defines a separation whereby the two superimposed zero phase wavelets (such as a sinc function) just start to flatten and no individual peaked features from the original wavelets are discernible. This equates to a separation of the inflection points of the main wavelet lobe. Building on this, Widess (1973) noted that if synthetic wavelets were convolved with opposite polarity delta functions that the resulting output could discern between beds thinner than 1/8 of a

wavelength by noting the changes of amplitude of the composite reflection. Kallweit and Wood (1982) investigated the three criterion of Rayleigh, Ricker and Widess in an attempt to formulate a general resolution limit for the minimum time separation between two reflective interfaces. They examined the case of resolving a thin wedge with two positive oriented zero phase wavelets (described by different functions such as Ricker, Ormsby and sinc functions commonly used in seismic modeling), and a second case of opposite polarity wavelets. Kallweit and Wood (1982) discovered that only one set of resolution parameters were required to formulate a resolution criterion, described below.

The "Klauder" wavelet used in the Lithoprobe seismic data has a continuous frequency spectrum between 12 and 56 Hz and may be mathematically described as:

$$w(t) = \frac{2f_u \sin 2\pi f_u t}{2\pi f_u t} - \frac{2f_l \sin 2\pi f_l t}{2\pi f_l t} \qquad (5)$$

where f_u and f_l are the upper and lower frequency limits, respectively [figure 2.2]. With the peak to trough distance of the wavelet labeled as "b" [figure 2.2] the Rayleigh criterion (T_{Ra}) of a wavelet separation is b/2 seconds two way travel time and a similar "Ricker" criterion, T_{Rk}, with both formally defined below:

(Rayleigh) $$T_{Ra} = \frac{b}{2} \cong \frac{1}{1.4\, f_u} \qquad (6)$$

and,

(Ricker) $$T_{Rk} \cong \frac{1}{1.5\, f_u} \qquad (7)$$

for a frequency range band ratio (f_u/f_l) of more than 4, which is the case with our seismic data. Kallweit and Wood (1982) suggest that the theoretical resolution limit of seismic reflection data is the Ricker criterion of equation (7), but a more practical

resolution limit used on real "noisy" data should be the Rayleigh criterion (6). With the 12-56 Hz seismic vibrator source used in the seismic data input the practical Rayleigh resolution layered reflectors derived from equation (6) is 0.0128 seconds two way travel time which combined with the average representative velocity of the core samples of 6.08 km/s, yields a resolvable result from reflecting interfaces spaced more than 39 meters apart.

Additionally, the dominant frequency of the seismic data, as defined from Widess (1973), is the reciprocal of the time between the first minimas of the symmetric time domain wavelet. Thus, adapting the Rayleigh resolution equation (6) the predominant frequency for a constant box car source, as used in our seismic data set, is approximately 0.7 the upper frequency of the wavelet. This corresponds to 40 Hz in our 12-56 Hz linear sweep vibrator data, with a characteristic wavelength (assuming an indicative average core velocity of 6.08 km/s velocity) of 150 meters.

Table 1 Tectonic history associated with the Granite Lake area

Event	Time (Ma)	Trend direction	Comments
D1	1906-1853	N	Ductile compressional deformation evident. Both D1 and D2 events occur during the time of arc aggregation, after oceanic rifting.
D2	1850 -1838	N-E	Brittle-ductile deformation.
D3a,b	post 1842	E	Consists of folded structures and brittle-ductile shear zones . The north-south shortening produced the foliation dip in the metasedimentary bands seen in geologic outcrop in the Granite Lake study area.
D4a,b	?	N	Folded structures and brittle-ductile shear associated with east-west shortening, respectively. The initial east-west trending structures of D3 are now partially realligned in a north-south direction. This is presumed to be the cause of the "L" shaped metasedimentary belt [figure 1.3].
D5	?	N-NE	Block bounding faults caused by NW-SE shortening, probably coeval with the intial development of the Annabel lake shear zone [figure 1.1]and the ductile shear zones within the metasediments.
D6a,b	1806-1767	N	Oblique thrusting of the Kisseynew and Flin Flon belts southwestwards in a horizontally dextural fashion over the north-south trending Hanson Lake block contact to the west. This causes continuing shear in metasediments and the reactivation of the Annabel Lake shear zone situated a few kilometers east of the test site.
D7	post 1806	N-NE	Brittle faults caused by NW-SE shortening and the cooling of the rock samples after peak metamorphism of the D3-D4 period in the Flin Flon belt. Probably was the cause of the Granite lake shear zone.

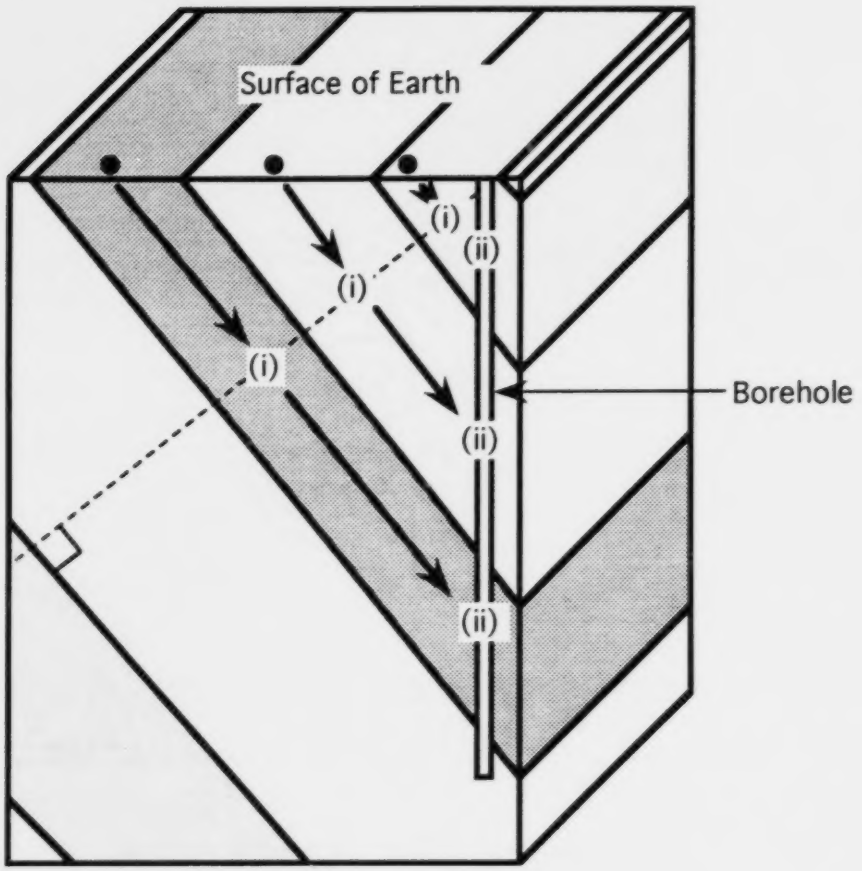

Figure 2.1 . Relation of surface samples to depth. The schematic shows a section of the test site with geological units alternately shaded and the surface sample positions denoted by dots. Line (i) represents the path of the reflected sound energy. Line (ii) represents the projection of surface velocities to vertical in order to simulate a wellbore.

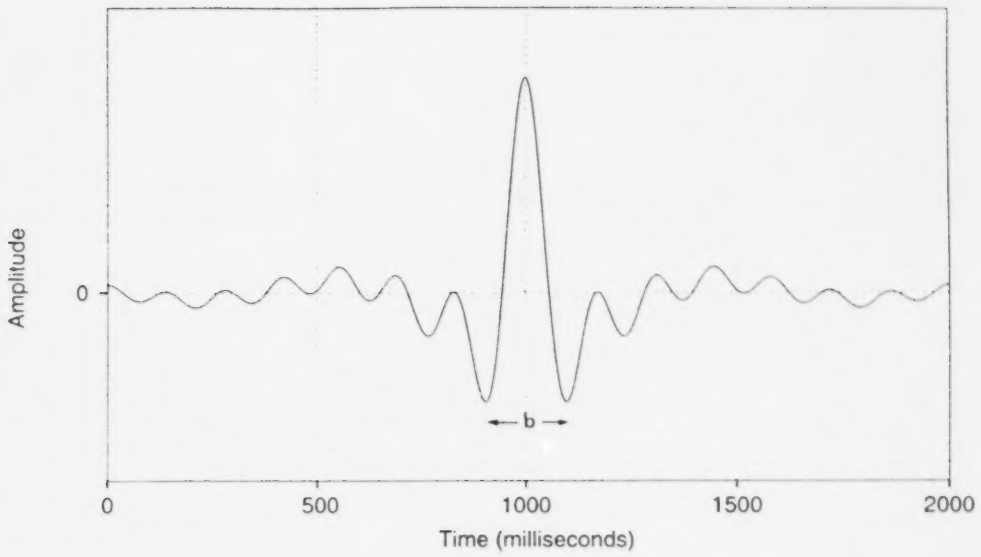

Figure 2.2 . Klauder wavelet. Upper and lower frequencies 56 Hz and 12 Hz respectively, with a positive 1000 millisecond time shift and a Rayleigh resolution limit of b/2.

CHAPTER 3

Experimental Procedure

3.1 Introduction

Surface samples from the geologic outcrop in the Granite Lake region are presumed to have a relationship to the subsurface structure imaged by the seismic line in the same region. The properties of compressional wave velocities, density measurements and the mineralogical components of selected surface rock samples may shed some light as to the positioning and cause of the seismic reflector. This chapter describes the methodology behind the acquisition of these parameters and discusses their relative accuracies.

3.2 Sample preparation

Samples collected from the field were cut into rough prisms of approximately 15 cm dimensions using a diamond tipped circular saw. One set of faces was cut parallel to the observed foliation as indicated in figure 3.1 which accomplished three goals . Firstly, the weathered external surface layer of the rock which may alter the intrinsic velocity response of the rock (as explained later in the chapter) was removed. Secondly, the foliation planes become much more visible on the freshly cut faces allowing a more accurate foliation direction to be delineated. Thirdly, any potential lineations in the rock fabric are exposed and marked. It is noted that lineation directions are displayed by a general alignment of relatively long and thin crystals, such as hornblendes and sheared plagioclases, which lie in the plane of the foliation. If the samples were cut in a plane oblique to that of the foliation, the face would show no lineation as only the tips of the

'long' crystals would be exposed forming a series of dots rather than exposing the length of the crystals. In some cases lineation was not strong, but was marked on the sample and dealt with in a similar manner to those more obviously lineated samples as it was unsure whether these samples would display any velocity anisotropy associated with potential lineation directions.

In eight of the eighteen samples tested there was no visible lineation to the naked eye or under hand lens examination. As the ultrasonic source used to measure the velocity is a piezoelectric ceramic of 1 MHz dominant frequency, the wavelength of the input pulse is typically 6 mm (assuming a 6 km/s acoustic velocity). This is more than an order of magnitude larger than the smallest observable structure in the rock, so most likely any lineation too small to be visible at hand lens magnifications should be effectively homogeneous in its velocity response in any azimuth with respect to the plane of foliation, and would not be expected to display any lineation related anisotropy. As a result, when lineation was not observed on freshly cut foliation planes only two orthogonal cores were drilled; one being perpendicular and the other parallel to the foliation plane under the assumption that these directions would display the greatest variation in velocities. Otherwise, visibly lineated samples had cores drilled in three orthogonal planes. These planes are assumed to be aligned with the directions of the extreme velocity values within a rock sample and are:

(i) perpendicular to foliation,

(ii) parallel to foliation and perpendicular to lineation, and

(iii) parallel to foliation and parallel to lineation.

Experimentally, this approach was validated by observing the velocity anisotropy of the most strongly lineated and the visually least lineated samples 12 and 2, respectively. These were chosen out of a total suite of 18 sample sites shown in figure 1.3 .

In sample 2 no visible lineation was observed and core orientations (ii) and (iii) were taken from the parent block arbitrarily at 90° to each other in the plane of foliation. A thin section of this rock parallel to foliation, figure 3.2, also showed a lack of lineation under high magnification with an homogeneous distribution of minerals of no preferred orientation. In comparison, figure 3.3 shows a thin section again parallel to foliation of sample 12. This thin section displays a clear alignment of the elongated hornblende and plagioclase crystals on a millimeter scale. The velocity determinations yielded an anisotropy of less than 0.2% between core direction (ii) and (iii) in the non-lineated sample 2 which is well within the 2% velocity measurement uncertainty associated with this technique. However, the strongly lineated cores (ii) and (iii) of sample 12 displayed the second largest lineation anisotropy of 4.5%. This significant anisotropy is most probably linked to the preferred orientation of the lineated crystalline structure [Birch (1961)].

The largest lineation anisotropy of 7% was displayed by sample 8 which is characterized by small amounts of quartz veining and large hornblende crystals. In this sample, the velocity variations are attributed, in part, to heterogeneity of the parent sample rock due to a large hornblende crystal. As a result the high anisotropies associated with this sample are largely related to variations in mineral modal compositions rather than the lineation existing within the rock.

Cored samples were required for velocity evaluation in our experimental configuration. The coring process was performed using a diamond tipped tubular drill with a 2.54 cm internal diameter mounted in a drill press in Dr. T. E. Evans laboratory. The prismatic blocks were oriented and then clamped secure in order to allow drilling in the appropriate directions. Next, this core was clamped in a rock cutting saw in order to

cut the ends approximately parallel. However a more precise process is required to finish the core ends parallel and flat. If the cylindrical core sample is not ground flat at either end, the ultrasonic pulse signal (used in the laboratory velocity acquisition technique) will be scattered at the transmitting and receiving surfaces, reducing the received signal strength and increasing the relative level of unwanted noise. Additionally, if the ends are not parallel the transmitted signal will be incident upon the receiver at an oblique angle causing a reduction in the signal strength and making the length measurement, associated with velocity calculation, far more complex and potentially erroneous.

The core-end grinding set up consisted of the sample cores being secured vertically by means of a 'V' block and horse-shoe clamp with the 'V' block magnetically attached to a horizontally traveling table which is free to move in two perpendicular directions in the horizontal plane. Before grinding, the ends of the cores were 'blackened' with a permanent marker. As end grinding proceeds, the blackened area shows the untouched rock area and indicates that further grinding is required. During the grinding, rough cuts are first taken 0.1 mm deep with sweep spacing of 2.5 mm. On removal of all of the blackened end a final fine cut is performed removing 0.025 mm in a series of sweeps 1.3 mm apart. At this stage the end is flat and perpendicular to the axis of the core. The core was then rotated around with the same side being clamped to the 'V' block and the process repeated to grind the other end perpendicular to the core axis resulting in parallel core faces.

The ground samples exhibited a mean parallelism of 0.044 ± 0.036 mm of a standard deviation. This accuracy was ascertained by placing a dial gauge and the core on a precision table ground flat for machinist measurements. The individual errors in parallelism, displayed in Table 2, were calculated as the maximum deviation in the dial gauge readings from one face of the core whilst the other face was flat on the table. This analysis produced minimum parallelism errors of 0.025 mm to a maximum error of 0.18 mm with the largest deviations in parallelism resulting from the shortest cores. Also, the

statistical mode of parallelism error was found to be the lowest deviation discernible by the dial gauge system of 0.025 mm.

Short cores (< 30 mm) were generally obtained from small or awkwardly shaped blocks. With the difficulty in securing the small samples firmly during drilling, the resulting cores often had irregular sides. When clamping these cores in the grinding set up their sides often did not lie flat against the 'V' block and so when grinding both ends it was difficult to identically clamp the samples to ensure the ground ends were parallel to each other. This could produce an extreme velocity error of 1% assuming the velocity error is solely related to the possible error in parallelism [Table 2], but in most cases the velocity error associated with the non-parallel ends was less than 0.2%.

As both the density and velocity measurements, ultimately required for the seismic interpretation depend on the dimension of core length and it is essential that these errors be reduced to a minimum. The 0.2% length error is satisfactorily small and has a negligible effect on the measured velocities.

3.3 Density measurements

Bulk density is the division of the total mass by the volume of the dry core sample. Suitable density measurements were performed on the core samples in order to calculate the impedance of the rock which is the product of density and velocity.

Core mass was measured on an electronic scale to an accuracy of one hundredth of a gram. Volume measurements were derived from dimensions of length and diameter of the core. However, the non-uniform cross section of the core, related to a poor sample clamping procedure, produces substantial errors in the diameter and the subsequent volumetric calculations. In order to minimize the error in volume associated with the diameter of the core several measurements were made at points along the core length with

vernier calipers accurate to 10^{-5} m. The maximum and minimum diameters were noted and averaged to form the representative diameter measurement [Table 2] with the diameter error being half the difference between maximum and minimum values. The volume of the cores and associated errors was calculated under the assumption that they were right circular cylinders. Using this volume measurement in conjunction with the mass measurements, the density values and errors of the cores were assessed [Table 2]. The errors were normally less than 4%. However, a few measurements had errors of up to 20% which is clearly too large for a representative measurement. Fortunately, due to the fact that two or three cores were taken from each rock sample there is a certain redundancy of data with which one can find a less erroneous rock density measurement in a particular sample.

Almost all the sample rocks have mineral grain sizes were much smaller than the core dimensions and therefore it was assumed that the measured core densities were representative of the sample host rock. Under such assumptions, if one of a set of three cores had a large density uncertainty, the average density of the other two similar cores for the same rock provided the density for use in the impedance calculation. This new uncertainty was taken to be the sum of the errors from the two cores. However, in some cases the error from the two combined cores is greater than that of the individual core, and therefore the more accurate density of the single core is used. Density revaluation was required for samples 6, 12, 13, and 33. However, in the case of sample 16 only two cores were available and the error allocated to the erroneous sample was arbitrarily defined as twice that of the 'accurate'. In such a manner the density errors used in the final analysis, Chapter 4, were generally kept less than 4%.

Coarse grained rocks and those with large quartz veins display the largest variations in bulk density from core to core as the mineralogic composition of the rock greatly varies on the core scale. To be statistically valid such rock samples need to be analyzed on a larger scale. An example of this is from core 8 (i) [Table 3] which has a bulk density

of 2838 ± 20 kg/m^3 contrasting with the other related cores 8(ii) and 8(iii) of respective densities 2785 ± 26 and 2738 ± 19 kg/m^3. Even considering maximum deviations, core 8(i) obviously has a distinctly different density than the other two. Inspection of the rock, 8(i) reveals a large hornblende crystal at one end of the core which was not visible in the other two cores and was not sampled in the thin section. Hornblende has a specific density of 3 g/cm^3, which is larger than the major rock component of plagioclase whose density is 2.6-2.8 g/cm^3 [Emiliani 1987]. Therefore the abnormally high amount of hornblende in sample 8(i) would account for it being distinctly more dense than the other two cores from the host rock.

The Archemedian principal was tried as an alternative volumetric calculation in an attempt to reduce the density errors.

Archemedies law simply states the weight of the fluid displaced by a body is equal to the apparent weight loss of the body. Therefore by suspending the rock sample into a beaker filled with water on a mass scale, the apparent reduction in the core weight can be determined. This value together with the known density of the fluid is used to calculate the volume of water displaced. Further, to prevent the core from absorbing any water it was smeared with a thin coating of paraffin oil. The mass of the beaker and water was such that a simple balance scale had to be used to weigh the beaker. This scale proved to be unreliable to more than 0.5 of a gram, and cores of minimal density errors, calculated by the previous system were compared to the densities derived from the Archemedian principal resulting in discrepancies of over 8%. Discrepancies of over 7% occurred between two cores taken from the same sample, proving this specific Archemedian configuration to be inaccurate. With a more accurate and repeatable balance, this method may prove to be an accurate measure of density, and indeed is versatile enough to accommodate density measurements for irregularly shaped rock samples.

The rock samples in this region have minimal porosity of 0.2% at the surface [Stead et al. (1993)]. Therefore in their present condition the rock can only hold small amounts

of fluid, which is a common situation for most crystalline metamorphic and igneous rocks [Birch (1961)]. In order to minimize the effects of fluids within the samples the cores were stored in an air tight desiccator containing water absorbing calcium sulfate crystals in order to eliminate any moisture in the sample. In one case a core from sample 5 (parallel to foliation) was intruded with the pressure vessel hydrostatic confinement oil during an experiment due to failure of the protective seal around the sample. This sample was soaked for more than 24 hours in toluene in order to dissolve the oil, then dried for 24 hours in an oven at 50°C and then retested. The second velocity measurement on this sample was within 0.3% of the first and this difference is well within the 2% velocity error of this experiment suggesting that the fluid intrusion have little effect on the measured velocity in these low porosity rocks, and trapped fluid effects on the sample are of little concern. However, if the rocks were porous and fluid filled they would display a different velocity pressure relationships described in Rouleau (1994).

3.4 Micro cracks

Velocity measurements made at atmospheric pressures are not indicative of the intrinsic mineralogical rock velocity. Indeed, rocks found from surface outcrops are often fractured on a microscopic scale caused by such processes as weathering and stress relief. These "micro crack" features can drastically reduce the true intrinsic mineralogical rock velocities and thus provide a spurious indication of rock velocities at depth. Elevated pressures close the micro cracks and reveal the near intrinsic mineralogical rock properties. For reference, Simmons and Richter (1976) define a micro crack as:

> " an opening that occurs in rocks and has one or two dimensions smaller than the third. For flat microcracks, one dimension is much less than the other two and the width to length ratio, termed crack aspect ratio, must be

less than 10^{-2} and is typically 10^{-3} to 10^{-5}. The length.... typically is of the order of 100 micrometers or less."

Since these microcracks control to a large degree the physical properties of the rock, and especially the elastic wave velocity, it is important that their influence on the measurements be determined.

Some authors believe that micro cracking may be associated with the drop in confining stress on rocks formed at depth which were then exhumed and had a corresponding drop in their confining stress. This stress drop, at least over the scale of hours, results in the growth of microcracks in rock samples by a poorly understood process called "stress relief" in the literature [Teufel and Warpinski (1984)]. However, the primary supporting evidence for such "stress relief" is observed from cored samples removed from subsurface rock which subsequently dilate over several hours and produce sonic emissions related to the growth of crack porosity. How applicable this stress relief is to the case of metamorphic rocks which were uplifted to the surface over the course of hundreds of millions of years is yet unknown.

The suite of rocks collected from the Granite Lake region are associated with high-grade metamorphism and plutonic intrusions. Therefore the present surface samples were formed at depth. Through tectonic activity the samples now outcrop at the surface where the confining stress on the sample is relatively small and the rocks may have relaxed both elastically and thermally. Towards the end of the tectonic activity the rocks had cooled and brittle type fractures started to dominate tectonic deformation regimes. At this later time, the stress fields could cause rock failure at these lower temperatures which is accompanied by micro crack formation. Micro cracks could have also been formed from a variety of other geological scenarios. For example, during the Quaternary ($\approx$ 0.01 Ma) the study region was covered with over 2 km of ice [Press and Siever (1986)]. The progression and regression of the ice-bedrock interface gouged the land surface and most likely stressed the surface rock possibly resulting in micro cracking. More recently,

weathering effects on the surface samples due to temperature variations and the freezing and thawing of water may initiate or increase the micro cracks found within the rock.

With micro cracking, the effective bulk modulus of the dry sample and the subsequent acoustic velocity is lowered from the nonporous intrinsic state. Not until all the micro cracks have been closed by high confining pressures of 1000 to 2000 bar [Krantz (1983)] are the true intrinsic mineral velocity-pressure characteristics of the rock apparent. Figure 3.4 shows how the elastic wave velocity measured in a micro cracked rock sample compares to a hypothetical porosity-free rock. The velocity-pressure graph of a real measurement from this experiment is displayed in figure 3.5, this displays similar behavior to the theoretical velocity properties of a micro cracked rock in figure 3.4 . Not until the linear portion of the pressure-velocity curve is reached are the micro cracks substantially closed and at this point near intrinsic rock velocities are obtained as discussed by Christensen (1965). This constant slope section can be linearly extrapolated to get the approximate micro crack free velocity characteristics of the sample rocks with pressure.

There is some discussion as to the pressure required to obtain closure of the micro cracks in order that intrinsic properties be measured; to a degree these arguments appear to correlate with the peak pressure obtainable in the pressure system available. In searching the literature, works such as Krantz (1983), Christensen (1965), Christensen and Szymannski (1988), Christensen (personal communication (1992)), and others display data that suggests 2000 bar is sufficient pressure for metamorphic and igneous rocks to display intrinsic characteristics. However, Burke and Fountain (1989) argue that their metamorphic metagraywackes display substantial crack porosity up to 3000 bar and Fountain (1993) indicates that 3000 bar was required for micro crack closure in a granitoid rock. It is clear that every case is different and depends on the rock's history of deformation and weathering. Indeed, such micro crack porosity is noted to be a problem even to 10 Kbar when researchers have attempted to determine the intrinsic properties of

single mineral polycrystalline ceramics. In the present situation the linear relationship between velocity and pressure is extrapolated over a limited range of pressures to obtain approximate, but lower bounding, mineral velocities of our rock samples at various depth equivalents.

In the cores tested it was noted that at high pressures the velocity-pressure graphs became linear generally above 1500 bar [see Appendix]. Furthermore, upon decreasing pressure, higher velocities were measured at the same pressure than during the initial pressurization. Burke and Fountain (1989) observe the same phenomena in a sheared metamorphic rock study which exhibited velocity hysteresis between their pressure up and pressure down runs. They attribute this to micro crack closure during pressurization and micro crack opening during depressurization. In the case of an ultramafic rock they found the typical non-linear velocity-pressure relationship at low pressures but observed no measurable hysteresis on depressurization. This was postulated to be an effect of complete opening of the micro cracks in this rock as a consequence of the pre-existing alteration along the grain boundaries which provided a "cushion" preventing crushing of the asperities (rough surfaces) on the micro crack's surface. Since there was no irreversible damage to the rocks in this process the micro cracks could easily reopen. As all our samples show some hysteresis, we might postulate that our samples have a negligible amount of the above alteration.

To further reduce the potential effects of the fractured rock associated with the surface samples only fresh outcrop was sampled and the outer most weathered layers removed.

3.5 Laboratory configuration and ultrasonic velocity measurements

Birch (1960) was one of the pioneers of laboratory ultrasonic measurements on rock samples at elevated pressures. He made velocity measurements at pressures of up to 10 Kbar using a "delayed mercury timing" approach. This method involved sending an ultrasonic pulse through a copper jacketed test sample, and sending an identically timed ultrasonic signal through a mercury column. Both the received signal from the second transducer on the test core and the signal from a receiving transducer mounted in the mercury column were sent to an oscilloscope. The length of the mercury column between the transducers was then adjusted until the travel times through the core and the mercury matched on the oscilloscope. The mercury column length was measured by a vernier scale to an accuracy of 0.0025 cm (one thousandths of an inch) which corresponds to a time error of 0.05 μs. The actual time delay reading through the sample was found by converting the mercury vernier scale reading into time according to a calibration performed on a test piece of steel with known length and acoustic velocity.

The method of mounting the piezoelectric ceramics onto the core samples in the present study is different from the method of Birch (1960). The Birch (1960) method first solders a copper foil sheet around the core, upon which the transducers are directly mounted. The copper foil jacket acts as an electrical contact for the transducers and this foil covers the sample and is soldered to form a seal against the confining fluid. The ultrasonic ceramics are then placed at either end of the sample and rubber tubing is stretched around it to ensure no fluid leakage between it and the foil. However the brittle ceramics are relatively exposed and easily damaged. In comparison the transducers in our experimental configuration are mounted inside durable aluminum end caps. Further, these end caps are arranged such that they provide an electrical contact for the transducers, and can be rapidly attached to the core. However, a disadvantage of the present configuration is that the end caps substantially separate the core samples from the piezoelectric

ceramics, and the intervening aluminum material has to be accounted for in calculating the travel times as shown later

A diagram of the end cap is shown in figure 3.6 . It holds a 1 MHz lead zirconate titanate piezoelectric compressional wave ceramic of 25.4 mm diameter and 2 mm thickness. The face upon which the ceramic is housed is precision machined flat and attached to the end cap with an electrically conductive silver epoxy glue. This ensures there is a good electrical contact of one crystal face to the aluminum. Care must be taken with the epoxy to ensure that no electrical contact are inadvertently made between the two surfaces of the cell which would short out any input or received pulses and render the cell useless. This entailed chamfering the corners of both crystal faces and using a minimum amount of glue to prevent it squeezing out to the top surface and forming a conductive link. The configuration is then allowed to set while being clamped in a vice to remove any air bubbles or glue pockets leaving the ceramic flat and parallel to the aluminum surface. Further, a wire approximately 4 cm long is soldered to the exposed face of the transducers in the end cap set up and another wire is screwed into the end cap body to form live and ground connections, respectively, terminating in insulated female connectors.

The end cap material was chosen for durability and more importantly for its ultrasonic impedance. Aluminum has an compressional velocity of approximately 6.8 km/s and density of 2.7 g/cm^3 as determined with the present experimental setup, which results in an impedance of 1.8×10^7 $kgm^{-2}s^{-1}$. The mean impedance of the rock samples, shown in chapter 4, are also 1.8×10^7 $kgm^{-2}s^{-1}$ with a standard deviation of approximately 0.1 $kgm^{-2}s^{-1}$. Consequently, looking at equation (1) section 2.7, the average reflection coefficient from the aluminum-rock interface is small and this is advantageous since nearly full transmission of the input signal occurs.

As seen in figure 3.6, a thin piece of Teflon paper (2.54 cm diameter and 0.008 cm thick) is inserted between the sample and the end cap. This Teflon serves two roles. First

a good contact between the core and the end cap is produced as the Teflon molds into any gaps in the interface. Second, in performing the end cap to end cap run the two transducers are electrically isolated.

Also apparent in figure 3.6 is the clear Tygon tubing surrounding the core and part of the end caps as opposed to a copper jacket seal in the Birch technique. The tubing forms a good fit, having the same internal diameter as the external diameter of the core and part of the end cap. However this 3 mm thick tubing alone is not sufficient to prevent fluid intrusion to the core sample when confined at elevated hydrostatic pressure. A good fluid seal is formed by wrapping wire around the tubing over the end cap section and twisting the ends secure. Alternative methods of clamping the tubing to the end caps were tried: hose clamps were effective but bulky and heat shrink tubing did not provide enough tangential force to seal effectively.

A problem was that in constricting the Tygon with wire was a bulge was produced in the tubing that displaced the end caps from the core samples. As the Tygon tubing has a finite rigidity, the hydrostatic confining pressure must first overcome the flexure forces of the Tygon tubing. Such flexure can be closed by minimal hand pressure, of say a 10 kg force. Comparing this to the axial forces applied to an the effective core cross section of the 2.5 cm circular diameter of the core we can find the hydrostatic pressure required to over come the Tygon flex using the simple ratio between the force and the area it acts over. This yields a relatively small closure pressure of 0.2 MPa (20 bar) which substantially lowers the effective pressure acting on the core at values of low confining pressure. At the maximum pressures of 2000 bar the Tygon tubing introduced a negligible 0.1% pressure error which combined with the 0.1-0.2 km/s/1000 bar velocity-pressure relationship of most candidate cores (see core samples in the Appendix) causing negligible velocity errors. In the end cap calibration run (explained later in section 3.8) there is no sample and the end caps are placed face to face with the customary Teflon paper sandwiched between. In this case the bulge in the Tygon, and the associated force

caused by the binding wires is now transmitted over the smaller length of the end caps only. This results in a large gap between the end caps which translates to a reduction of the normal stress applied to the ends of the samples. If a force of magnitude ten times that used for the previous sample configuration is assumed, this results in an error in the pressure reading of nearly 1% at 2000 bar. This problem was solved by tying the binding wire while the end cap system was clamped shut in a vice. As the wire was tightened and with the two end caps clamped together the bulge of the Tygon slid along the end caps instead of forcing them apart.

3.6 Pressure vessel

At room pressure the core samples display micro cracking which effect the intrinsic mineral rock properties of the core samples. At elevated confining pressures micro cracking is drastically reduced and a more representative velocity measurement can be performed on the core samples. Therefore, the sample and end cap arrangement are pressurized up to 2000 bar in either one of two steel pressure vessels with their dimensional characteristics as follows:

Pressure vessel	I	II
Internal diameter	3.9 cm	10.2 cm
Internal bore length	19.0 cm	50.8 cm

Effective diameter of end caps and Tygon seal	3.1 cm
Total length of both end caps	5.7 cm

In the large pressure vessel (II) core lengths of up to 45.1 cm may be tested whereas pressure vessel (I) can accommodate cores up to 13.3 cm in length. Both pressure vessels are capable of containing the effective diameter of the end cap-core arrangement including the limiting 3.1 cm diameter of the Tygon tubing. Pressure vessel (I) was used in all of the final data in this study, but in setting up the system the larger vessel (II) was more convenient since it had less dimensional constraints.

The pressure vessels need to accommodate wire feed throughs for the transmitting and receiving transducers. However, at 2000 bar maximum pressure conventional electronic feed throughs tend to rupture. As seen in figure 3.7, the feed throughs are designed with a high pressure adaptation of a notch. Up to four ceramic coated, and therefore electrically insulated, copper wires are used in each feed through. These are bent around a notch and glued with epoxy to secure them and to ensure an impermeable seal. The notch acts as a solid obstruction against the fluid pressure in the vessel. The feed through is then housed in a hollow screw which fits into the vessel forcing the feed through against a counter bored hole drilled in either the side of the pressure vessel or the center of one of the sealing caps [figure 3.7]. One set of feed through wires pass out of the top sealing cap and one set comes through the side of the vessel [figure 3.7]. Care is required in making the feed through assembly to ensure that the latter set of wires are long enough to reach the outside of the pressure vessel chamber in order that the connections can be made outside the limited confines of the vessel cylinder. Finally, the sample is placed in the pressure vessel and the sealing cap is bolted down. Pressure readings are taken from a 1 bar finest scale Heise dial gauge meter, which was proven to be consistent with our laboratory standard gauge to maximum deviation of 5 bar, with the finest division of the standard also being 5 bar.

3.7 Ultrasonic travel time measurements

In the experiments, a calibration run of the end cap to end cap transit time as a function of pressure is first carried out in order that this time may be removed from the core test to obtain the true core transit time of the ultrasonic transducer pulse. The transmitting transducer input was provided by a FET (field-effect transistor) driven square wave generator, constructed in our laboratory. It has a 22 volts peak to peak output with a variable repeat frequency from 100 Hz to 20 KHz and pulse length of up to 45 microseconds. The input square wave is sampled by a digital oscilloscope which is triggered by a pulse provided from the same square wave generator. As observed on the oscilloscope, the input square wave rise time is initially 56 volts/μs. This voltage pulse across the piezoelectric ceramic causes it to expand longitudinally and thus produces the source of the sound wave which propagates into the sample. The transmitted acoustic pulse in turn applies a stress to the receiving transducer which changes volume and as a result produces a voltage difference across its ends which is displayed on a digital oscilloscope.

The digital oscilloscope is used to display the resulting input (sending) and output (receiving) traces simultaneously on the screen. These traces are acquired at a rate of 0.1 sample/ns although in the case of very short travel times, such as end cap to end cap runs, the system can be used at the higher sampling rate of 0.4 sample/ns. The wave form of the received output is approximately sinusoidal with a predominant frequency of 1 MHz which is the resonant frequency of the piezoelectric ceramics. Unfortunately, the first break of this wave is often obscured by electronic noise and is therefore not accurately discernible to more than 50 ns. However, the first peak is more clearly defined and the first maxima has a reading error of ± 4 ns in the end cap to end cap set up. Therefore to make a travel time measurement the first time cursor is placed on the first upward break of the input wave form ± 4 ns to provide a time reference position, and the second cursor

is placed on the first peak of the received transducer output with the time of flight being the difference between the time readings of the two cursors. With a typical 7.1 μs end cap pulse transit times the associated error is 0.1%. The oscilloscope time base and vertical voltage per division were always kept identical for this reading in order to eliminate errors associated with the scales. Since the input square wave does not rise instantaneously when viewed at the highest time scale resolution it is difficult to localize the first break. However, on the basis of experience gained from repeated measurements optimum settings for this channel were determined.

During a test the sample is pressurized in discrete steps to a maximum of 2000 bar. Travel times were recorded at a series of pressures and a greater concentration of readings were taken at higher pressures in the most useful linear, near micro crack free portion of the velocity-pressure curve. Travel times at zero pressure were not recorded as the end caps are generally not in contact with the core sample and the received response was either non-existent or at best very noisy.

After each pressure step an equilibration time of three to four minutes was required for the received signal to equilibrate to its previous DC. position on the oscilloscope. It is seen that the transducers have a fine porous structure. As such, flow of confining fluid into the ceramic will induce poroelastic stresses which could also produce a change in volume and hence a differential voltage across the ceramic. Although this suggestion has not been rigorously tested it is in qualitative agreement with the observation that an increasing pressure produces a positive DC. shift, whereas a depressurization results in a voltage drop.

At 2000 bar peak pressure the sample was left to stand for one hour in order to monitor the travel time under nearly constant pressure. The rational for this was that if the Tygon Tubing had leaked and allowed fluid to enter the pore space of the rocks then this fluid infiltration would have the effect of lowering the effective confining pressure on the

sample and hence alter its velocity. The rock sample was then depressurized in the same discrete pressure steps as in the pressurization run and ultrasonic travel times were noted.

3.8 Travel time correction of the end caps

A problem with subtracting the end caps transit times from those through the core run is that the pressure at which either were measured do not exactly correspond. The end cap data is discrete and the travel time values are not always taken at exact pressure multiples of 100 bar pressure. Therefore, a continuous correction function was required of travel time vs. pressure formulated by using a least squared fit curve. A number of fitting parameters were tried but the optimal curve was found to be a second order polynomial described in figure 3.8 . Correlation coefficients which provide a measure of how well a chosen function models the data for all the end cap correction runs were above 0.995 . Indeed, the maximum deviation of the real data to the best fit curve was always within 20 nanoseconds and this relatively large discrepancy value occurred in the low pressure readings under the influence of the Tygon tubing and deformation of the Teflon paper. In any event, these low pressure transit times were the least important pressure regime in this experiment, which is trying to focus on the higher pressured micro crack free region of the core velocity-pressure relationship. It is also noted that the end cap calibration transit times have very little hysteresis. Only at the low pressures was there any time difference between pressurization and depressurization as indicated by separation of time readings at a given pressure in figure 3.8 . This variation was mainly attributed to the deformation of the Teflon paper, but additional effects such as a potential porosity of the aluminum end caps at high fluid pressures cannot be ruled out. As there is minimal hysteresis in end cap transit time measurements, especially at higher pressures regimes, a best curve model was calculated using both the pressurization and depressurization data.

With the equation of this curve, the correction factor for the core measurements was simply removed.

Initially, it was assumed that one end cap correction would be sufficient to apply to all subsequent core measurements. Unfortunately additional corrections were required that result from a drifting in the end cap transit times. It was observed that the original set of end cap travel times had a time shift of 40 ns from a second calibration after over 30 tests had been performed. An associated velocity error of approximately 0.6% resulted from this, assuming an average 7.1 μs end cap pair transit travel time. In the latter part of the study, which employed the smaller pressure vessel (II), a new set of end caps was used. With these, calibration runs were frequently performed in the retesting of previous samples and subsequent testing of new samples. Maximum travel time deviations of less than 30 ns and an associated velocity error of less than 0.4% were then apparent. This latter set was used for all transit time evaluations in this thesis.

Whether this apparent end cap degradation is a function of time or the number of experiments or some other factor is difficult to determine. Table 4 contains relevant data on the number of days between end cap calibrations, the number of samples tested in each intervening period between calibrations, and the associated difference in travel times between subsequent calibrations. The delay time in the table is calculated using values at 2000 bar and this is taken to be indicative of the trends in the delay for the end caps at all pressures [figure 3.9].

The predominant feature of table 4 and the corresponding figure 3.9 is that the travel times of the end caps increase with time and use. By looking at table 4 it can be seen that between the 8/1/94 - 27/11/93 and 4/11/93 - 9/8/93 runs there were no intervening pressurizations of the end caps and insignificant time changes in the transit times observed, despite the fact that the end caps had aged 42 and 97 days respectively. Furthermore, all calibration runs that had more than 5 intervening pressurizations had significant time drifts of 24 nanoseconds and greater. This strongly suggests that the end

caps degrade with use more so than with time. As such, the end cap travel times cannot be used at face value as there is significant discrepancy between subsequent calibrations. To overcome this problem, a linear trend in the delays was assumed between calibrations with a time correction linearly dependent on the number of intervening pressurization runs. However, the quantitative relationship between the drift and the end cap pressurization history is unclear. For example, as the samples were often left overnight at 2000 bar, time spent at pressure may be the most important influence on the delays. Additionally, the transducers were left for days in unpressurized fluid or dry air. Regardless, all these effects are not quantifiable in this report and would require further study to investigate. However it was borne out by experience that the results were sufficiently repeatable if the end caps were calibrated every 17 runs.

Interestingly, it was found for the first few runs after preparation the end caps would yield inconsistent transit times. This was remedied by leaving the end caps in the pressure vessel at 2000 bar for 12 hours or more; the reason why this "seasoning" period was required is unknown. But using the seasoned end caps, and with frequent calibration measurements, the end cap transit travel times can be accurately monitored and used to confidently correct the core sample transit times. Finally, it was noted that in performing the core transit time measurements a 0.1 sample/ns digitizing time base had to be used with an error of 20 ns in the core tranist time which resulted in a 0.3% velocity error, assuming an average 8 μs core transit time.

3.9 Resulting velocity-pressure curves

In the present study it is shown that the velocity-pressure curves of the core samples become nearly linear at pressures of around 1500 bar as shown by the examples in figure 3.10 and the Appendix. Therefore, the maximum confining pressure available of 2000 bar is sufficient to almost eliminate the effect of microcracks, and the true intrinsic mineralogical velocities of the sample cores are displayed and analyzed in chapter 4.

3.10 Temperature effects

Changing temperatures within the pressure vessel could be detrimental to the travel time measurements because the intrinsic velocity of most materials are temperature dependent. In the present experiment it was known that the pressure vessel confining fluid warms on pressurization and cools during depressurization. In order to determine the severity of these phenomena we monitored the temperature variations during a typical pressure run using a thermocouple arrangement as shown in figure 3.11 . The 'live' end of the copper-constantan thermocouple was calibrated before being used in the pressure vessel with the reference copper-constantan junction being maintained at 0°C by ice water. Simply, the thermoelectric potential (in mV) was recorded when the thermocouple was placed first in boiling water and then ice was periodically added to the container until the temperature eventually reached near freezing. The resulting temperature as determined by a mercury thermometer vs. the thermoelectric potential graph was a linear relationship with a correlation coefficient of 0.9998 indicating that an accurate measure of temperature could be obtained from the thermocouple potential. The digital voltmeter accurate to 100 nV which corresponds to a hypothetical temperature accuracy of better than 0.1°C and the probe reaction time was a few seconds. Since only an approximate

measure of temperature variation was required, both these parameters were deemed accurate enough for the experiment.

The results of the temperature monitoring are shown in figure 3.12 .The temperature variation over the whole run was 10.9°C . The graph is a series of jagged lines caused by the initial pressurization temperature reading and the three or four minute cooling time until the next pressurization. Upon reaching 2000 bar the system was left to cool within 0.5°C of the initial room temperature and this took nearly one hour. The depressurization cycle was performed in a similar manner with the corresponding expected adiabatic cooling of the expanding fluid. Note that upon reaching room pressure, depressurizing from 2000 bar, the vessel fluid was cooler than the room temperature and was consequently equilibriated back up to room temperature in the final leg of the plot, figure 3.12 . Additionally, in a specific test of an end cap calibration test, the core was pressurized to 1990 bar in the normal manner. The confining pressure during the following cooling period was maintained constant by small inputs of pressurization and the observed travel times before and after the cooling period were identical within the sampling rate of the oscilloscope indicating that temperature effects were negligible in the present experiment. Further in the case of velocity changes of velocity at 2000 bar [Christensen (1979)] most igneous and metamorphic rocks have temperature gradients of between -0.5×10^{-3} km/s/°C and -0.6×10^{-3} km/s/°C. With a maximum temperature variation from room temperature of 5.6 °C the effect on the velocity is less than 0.003 km/s which is not detectable in the present experiments.

3.11 Mineral point count

Mineral modal analysis were undertaken to assess the effects of mineral composition on the observed ultrasonic velocities. Changes in mineralogy and mineral abundances are broadly related to changes in a rock's velocity response. Therefore, if the mineralogical variation is mapped, then this may have some relation to the velocity distribution of the rock samples and in turn may assist in the seismic interpretation.

Thin sections were taken from all the rock samples tested, and these were cut perpendicular to the observed foliation, as thin sections oriented *parallel* to the foliation are only indicative of a specific plane and not the whole rock. The crystal and grain sizes seen in all the rocks were of a millimeter and sub-millimeter scale suggesting that the 25 mm diameter sections provided statistically acceptable modal counts. If crystals are of the order of 25 mm or larger in dimension, then the thin section will not be large enough to sufficiently sample the mineralogy distribution, to any statistical significance.

An optical microscope with a set of cross hairs and cross polar capability was used in the study. The thin sections were mounted on a movable grid on the microscope stage. The optics were then moved in discrete steps along the grid and the minerals which lined up beneath the cross hairs were identified and recorded. These discrete steps occurred over the 2.54 diameter section such that there were over 1000 "point counts" made. The modal point counts are given in Table 5, and a graphical display of the major modal composition is shown in figure 3.13.

For ease of identification the slides were stained with sodium cobaltinitritite, which etches the plagioclases to become visually cloudy and stains the K-feldspars yellow in order that the two minerals may be more easily distinguished under normal unpolarized light which speeds up the mineral identification process. Standard microscope mineral identification techniques were used, as described in many texts such as Kerr (1977).

3.12 Experimental repeatability

Despite all the problems and uncertainties associated with calibrations, drift errors, and core length measurements the velocity measurements have proven to accurate to better than 2%. This value of 2% is formulated from repeatability tests that were normally within 0.5% (however, the shortest core 9 perpendicular to lineation and foliation had a 1.9% error), the end cap calibration had a time determination error of 0.1%, the core travel times had a 0.3% error, the core lengths had an error normally within 0.2%. Hereafter a 2% error is considered to be a conservative estimate of the uncertainty in the measurements.

A selection of the samples from the earliest experimental configuration used in pressure vessel (I) were retested with the smaller configuration and in general these comparisons differed by less than 2%. However, two tests displayed discrepancies of 2.5% and 2.6% which was considered unacceptable. For this reason, it was deemed necessary to remeasure all of those thirty samples initially tested in the large pressure vessel.

Density errors were dealt with on a core by core basis but generally the error was within 4%. However, other density determination techniques will have to be found in future to reduce this large error.

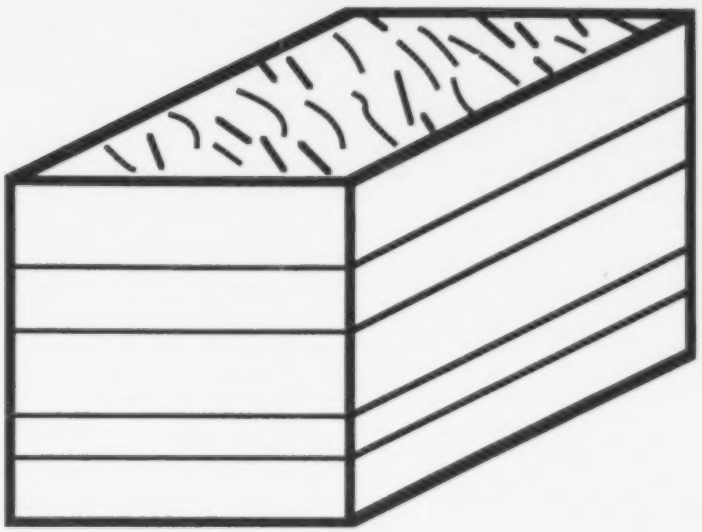

Figure 3.1. A layered rock sample cut with one set of faces parallel to the foliation plane. Straight solid lines represent foliation planes, or layering of the constituant materials. Lineation is shown from the orientation of long and thin crystals, such as hornblendes, denoted in the diagram by the wavy lines. The lower diagram is cut with no faces parallel to foliation, so no lineation direction can be seen.

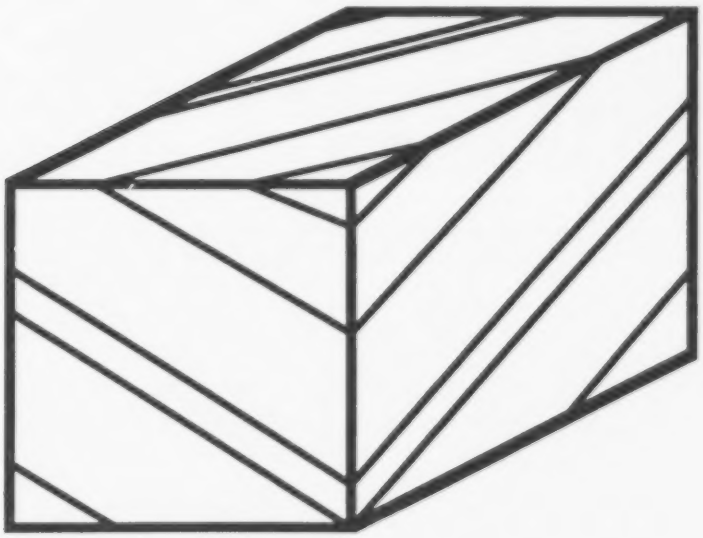

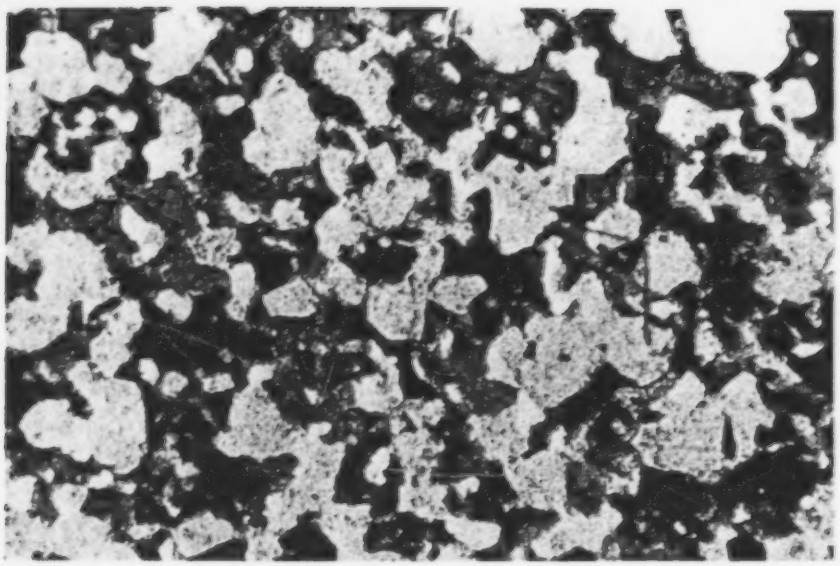

Figure 3.2 . Thin section of sample 2. Dark patches indicate hornblende crystals which is the major mineral component. Horizontal width of figure is 2.0 mm .

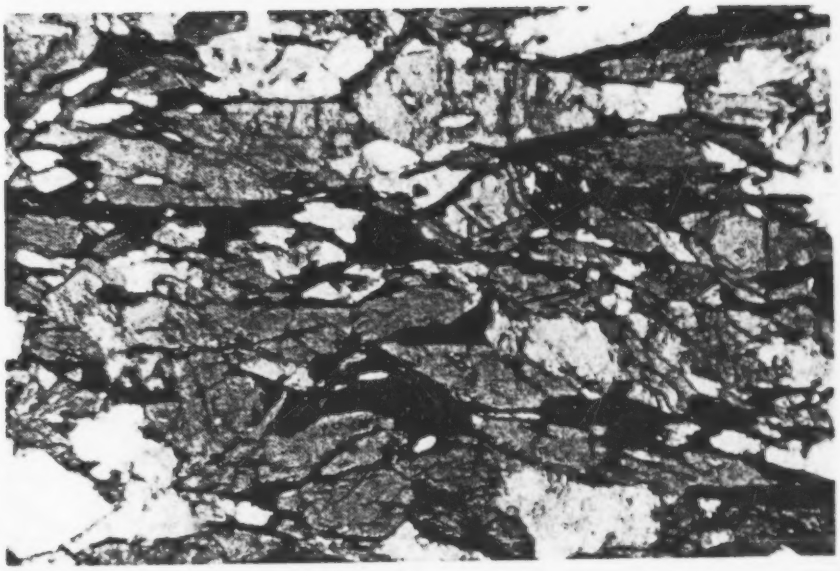

Figure 3.3 . Thin section of sample 12. Dark grey patches and lighter grey patches indicate hornblende and plagioclase crystals respectively, which are the major mineral components. Horizontal width of figure is 2.0 mm.

Table 2. Core dimensions

Sample	Diameter (mm)	Error in Diameter (mm)	Length (mm)	Parallelism (mm)	Mass (g)	Density (kg/m^3)	Error of Density (%)
1a (i)	24.53	0.03	45.88	0.0254	58.30	2690	0.81
1a (ii)*	24.55	0.01	75.18	0.0254	97.76	2747	0.36
2 (ii)	24.43	0.09	63.39	0.0508	86.98	2927	2.57
2 (iii)	24.53	0.03	43.20	0.0508	59.63	2920	1.14
2(i)	24.52	0.04	49.27	0.0508	68.14	2928	1.35
3 (i)	24.52	0.01	23.30	0.0508	30.19	2744	0.94
3 (ii)	24.58	0.04	56.09	0.0254	73.36	2756	1.17
3 (iii)	24.56	0.04	55.20	0.0254	72.17	2759	1.17
4 (i)	24.55	0.05	75.02	0.0508	98.35	2769	1.49
4 (ii)*	24.58	0.02	63.67	0.0254	82.98	2746	0.64
5 (ii)	24.50	0.03	47.76	0.0254	61.43	2728	0.94
5 (i)	24.50	0.02	42.30	0.0508	54.53	2735	0.76
6 (i)	24.50	0.01	26.04	0.0508	34.25	2790	0.87
6(iii)	24.41	0.21	18.18	0.1779	22.56	2651	8.48
6 (ii)	24.62	0.02	40.92	0.0254	54.29	2787	0.71
7 (i)	24.47	0.07	66.13	0.0254	87.40	2810	1.92
7 (iii)	24.58	0.04	52.08	0.0508	69.70	2820	1.33
7 (ii)	24.62	0.02	49.46	0.0508	66.86	2839	0.83
8 (i)	24.60	0.02	40.04	0.0254	54.01	2838	0.71
8 (iii)	24.56	0.03	44.44	0.0254	58.64	2785	0.95
8 (ii)	24.60	0.02	44.90	0.0254	58.44	2738	0.69
9 (i)	24.54	0.04	39.91	0.0254	52.71	2792	1.22
9 (ii)	24.55	0.03	19.29	0.1779	25.35	2776	3.67
9 (iii)	24.48	0.06	31.41	0.0508	40.96	2770	2.05
10 (i)	24.50	0.02	37.98	0.0254	50.49	2821	0.60
10 (ii)*	24.47	0.04	57.78	0.0254	76.93	2832	1.04
11b (i)	24.47	0.04	27.00	0.0508	34.15	2689	1.62
11b (ii)	24.62	0.04	31.58	0.0127	40.31	2681	1.15
12 (i)	24.44	0.14	30.88	0.0508	42.25	2917	3.99
12 (ii)	24.33	0.23	63.74	0.0508	87.03	2936	6.19
12 (iii)	24.50	0.08	65.34	0.0508	89.61	2909	2.30
13 (i)	24.46	0.01	50.81	0.0254	63.04	2640	0.41
13 (iii)	24.50	0.20	35.00	0.0508	43.66	2646	5.59
13 (ii)	24.54	0.04	58.48	0.0254	73.30	2650	1.16
15a (i)	24.45	0.02	79.98	0.0254	100.54	2677	0.49
15a (iii)	24.62	0.02	45.68	0.0381	57.35	2637	0.77
15a (ii)	24.32	0.22	41.02	0.0508	51.27	2690	6.07
16 (i)	23.74	0.74	40.98	0.0254	50.2	2767	19.78
16 (ii)*	24.48	0.02	34.49	0.0254	43.61	2686	0.75
32 (i)	24.51	0.01	58.44	0.0254	74.75	2711	0.39
32 (ii)*	24.47	0.03	56.39	0.0254	77.50	2922	0.91
33 (i)	24.53	0.03	48.70	0.1525	65.26	2835	1.75
33 (ii)	25.11	0.67	50.58	0.0254	65.62	2619	16.93
33 (iii)	24.49	0.11	43.12	0.0254	59.68	2938	3.01
34 (i)	24.51	<0.01	31.23	0.1016	39.32	2669	1.15
34 (ii)*	24.50	<0.01	51.06	0.0254	64.98	2699	0.28

Core orientations are denoted by: (i) perpendicular to foliation, (ii) parallel to foliation and perpendicular to lineation and (iii) parallel to lineation and foliation. if only two core directions are shown then perpendicular to foliation is still denoted by (i), and parallel to foliation as (ii)*.

Table 3. Velocity and impedance results

Sample	Perpendicular to Foliation				Parallel to Foliation Perpendicular to Lineation				Parallel to Foliation Parallel to Lineation				Distance along profile A-A' (km)	Sample
	Ultrasonic Velocity (km/s)	Bulk Density (kg/m^3)	Impedance (10^7) ($kg/m^2/s$)	Impedance error (%)	Ultrasonic Velocity (km/s)	Bulk Density (kg/m^3)	Impedance (10^7) ($kg/m^2/s$)	Impedance error (%)	Ultrasonic Velocity (km/s)	Bulk Density (kg/m^3)	Impedance (10^7) ($kg/m^2/s$)	Impedance error (%)		
34	5.97	2669	1.593	3.15	6.53	2699	1.762	2.28					0.3	34
33	6.39	2835	1.812	3.75	6.59	2887	1.903	6.76	6.88	2938	2.021	5.01	1.35	33
32	6.27	2711	1.700	2.39	6.77	2922	1.978	2.91					1.25	32
16	6.58	2686	1.767	3.48	6.47	2686	1.738	2.74					8.15	16
15a	5.79	2677	1.550	2.49	6.11	2690	1.644	8.07	6.18	2637	1.630	2.77	6.1	15a
13	6.47	2640	1.708	2.41	6.24	2650	1.654	3.16	6.31	2646	1.670	7.59	4.8	13
12	6.16	2917	1.797	5.99	6.85	2936	2.011	8.19	6.88	2909	2.001	4.3	4.1	12
11b	5.71	2689	1.535	3.62	6.18	2681	1.657	3.15					4	11b
10	5.93	2821	1.673	2.6	6.09	2832	1.725	3.04					3.75	10
9	6.21	2792	1.734	3.22	6.28	2776	1.743	5.67	6.33	2770	1.753	4.05	3.65	9
8	6.38	2838	1.811	2.71	6.98	2738	1.911	2.69	6.63	2785	1.846	2.95	3.7	8
7	6.27	2810	1.762	4	6.36	2839	1.806	2.83	6.35	2820	1.791	3.33	3.4	7
6	5.84	2790	1.629	2.87	6.48	2787	1.806	2.71	6.65	2789	1.855	3.58	3.5	6
5	5.79	2735	1.584	2.76	6.46	2728	1.762	2.94					3.1	5
4	5.82	2769	1.612	3.49	6.77	2746	1.859	2.64					2.75	4
3	6.33	2744	1.737	2.94	6.31	2756	1.739	3.16	6.34	2759	1.749	3.17	2.85	3
2	5.68	2928	1.663	3.35	6.5	2920	1.898	3.14	6.9	2927	2.020	4.57	3	2
1	5.79	2690	1.558	2.81	6.29	2747	1.728	2.36					2.5	1a

Velocities and impedance values are given at 2000 bar hydrostatic confining pressure. In the cases of only two cores from a given sample the first column still denotes cores aligned perpendicular to foliation, and the second suite of columns denote cores arbitrarily aligned parallel to foliation. The relative distance along A-A' refers to distance along highway 106 from the easterly contact of the eastern granodiorite metasediment boundary [figure 1.3].

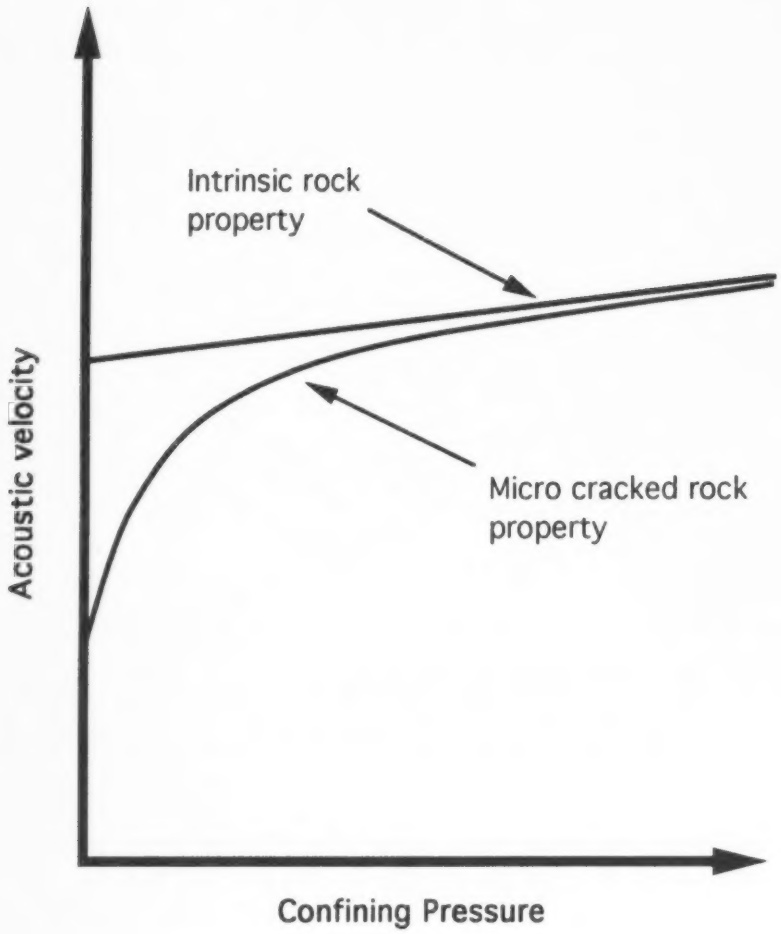

Figure 3.4 . Graph to illustrate the effects of micro cracks on physical rock properties such as acoustic velocity. The micro cracked rock is asymptotic to the intrinsic mineral properties at high pressures, at which point the microcracks have substantially closed.

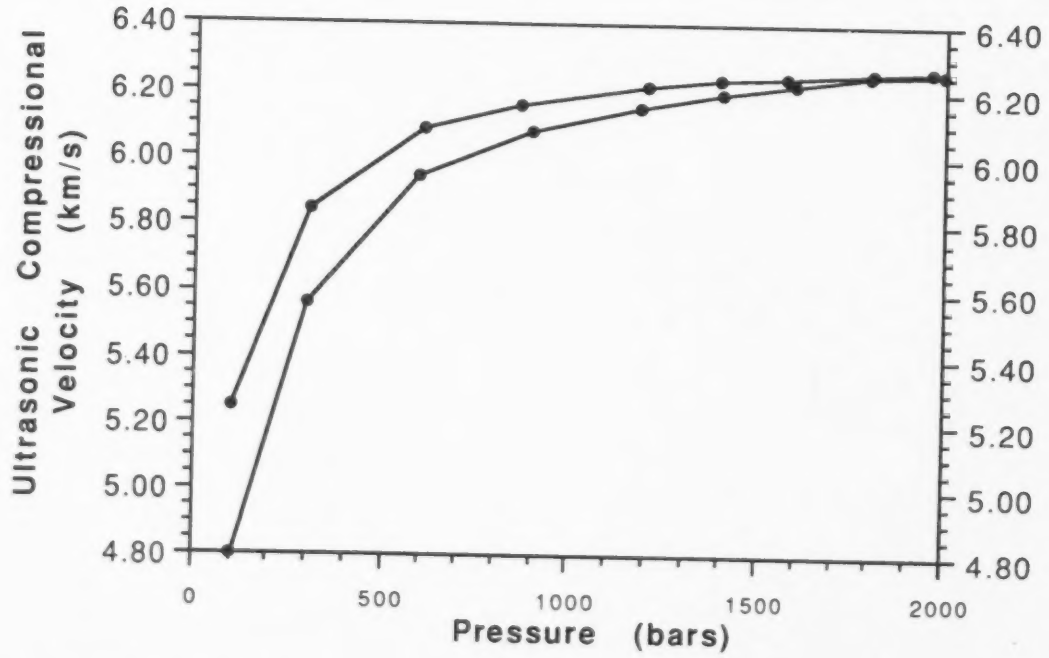

Figure 3.5. Velocity pressure run of a typical sample. The lower curve is observed during pressurization and the upper curve is observed during depressurization.

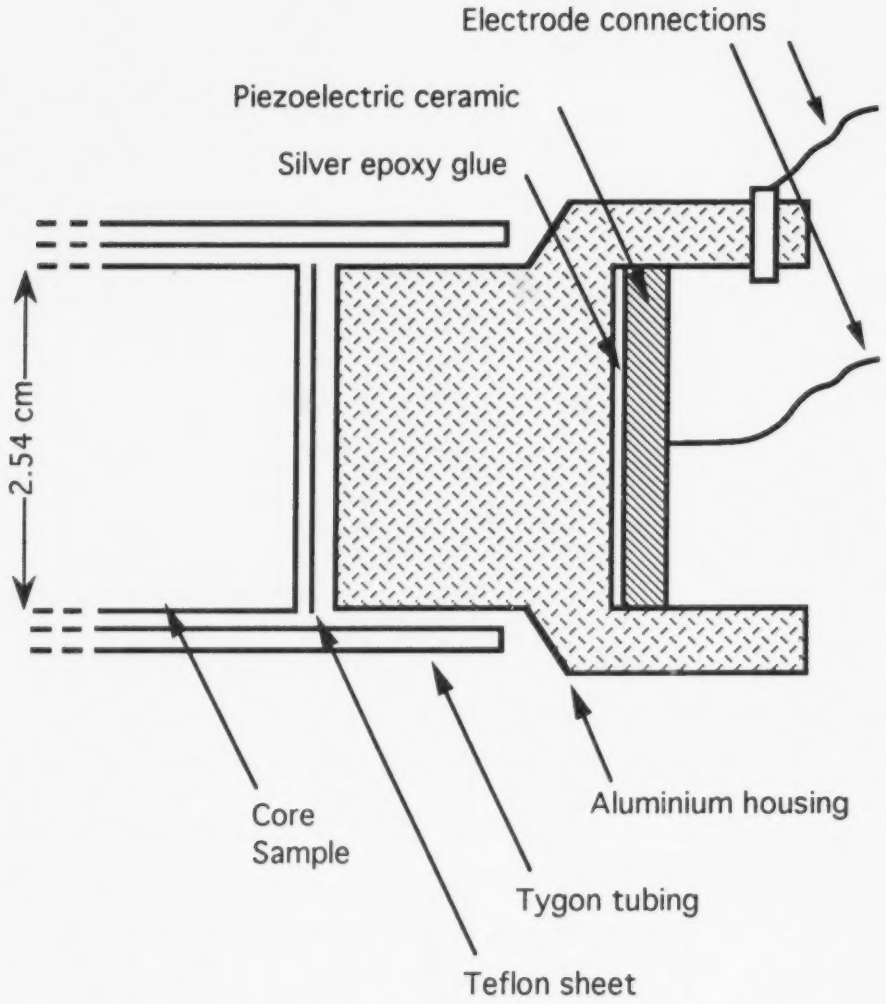

Figure 3.6 . Endcap housing of the piezoelectric ceramics. The aluminium mount helps protect the cell from physical damage. With this arrangement the tygon tubing forms a seal around the endcap and the core sample ensuring no hydrostatic confining fluid leaks into the sample.

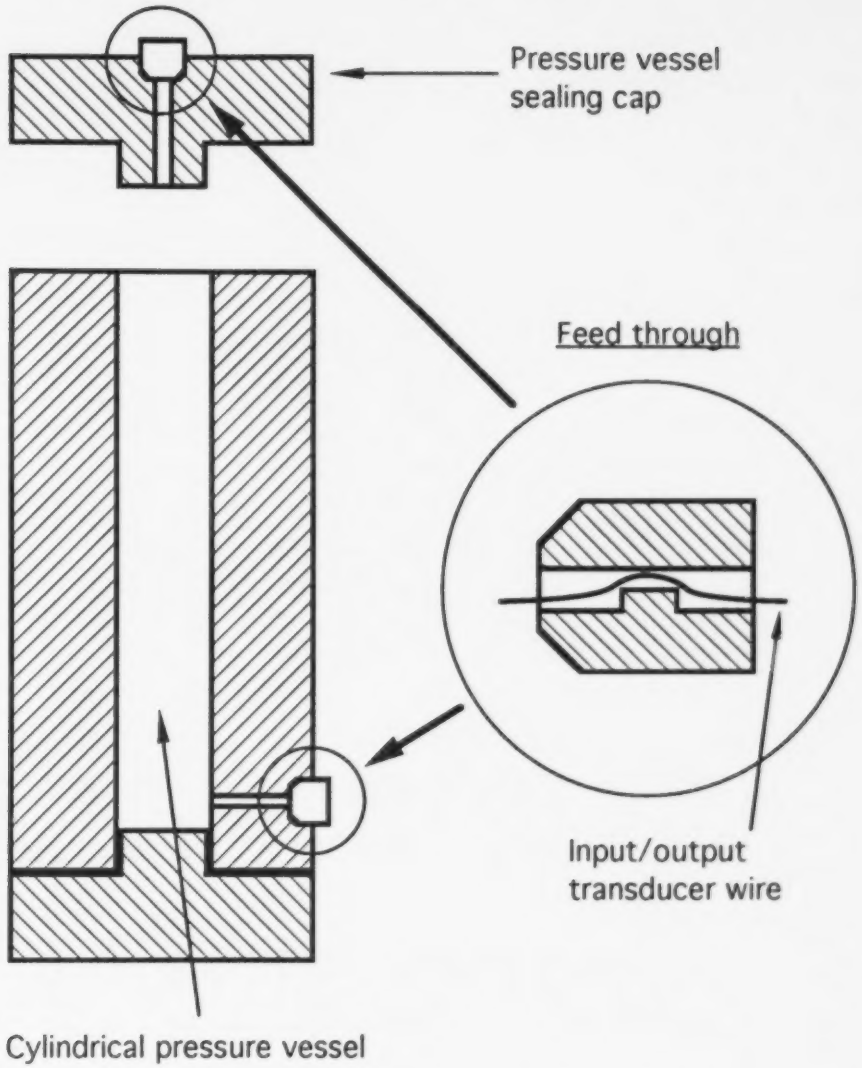

Figure 3.7 . Schematic cross section of the pressure vessel. Two sealing caps are arranged at either end of the pressure vessel and bolted in place. The transducer feed through wires are displayed in the enlarged circle, with a small notch preventing the wire from blowing out under pressure. The wire is also set in epoxy glue and the feed through is threaded into the main body of the pressure vessel.

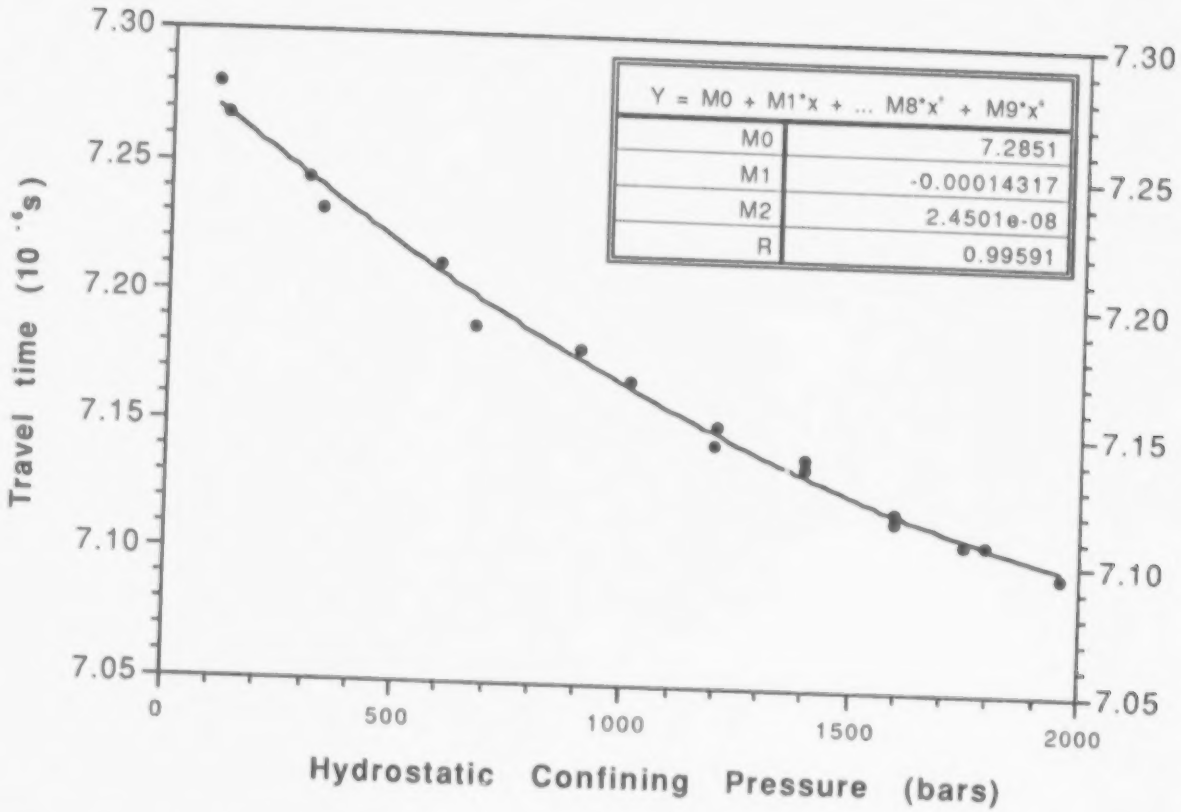

Figure 3.8 . End cap calibration. The graph displays travel time data for both pressurization and depressurization. Longer travel times at a given pressure were observed during pressurization. These data are modeled with a second order polynomial of co-efficients shown in the legend and with a correlation co-efficient of 0.99591.

Table 4. End cap calibration history

Date d/m/y	Number of days	Number of core measurements	Time drift (ns) (@ 2000 bars)
11/1/94			
	3	6	30
8/1/94			
	42	0	0
27/11/93			
	3	5	?
24/11/93			
	8	5	-4
16/11/24			
	12	17	28
4/11/93			
	97	0	8
9/8/93			
	9	11	24
18/6/93			
	32	14	4
17/5/93			

Note, a negative sign in the Time Drift *column denotes an increase in the travel time rather than the normal decrease with increasing date.*

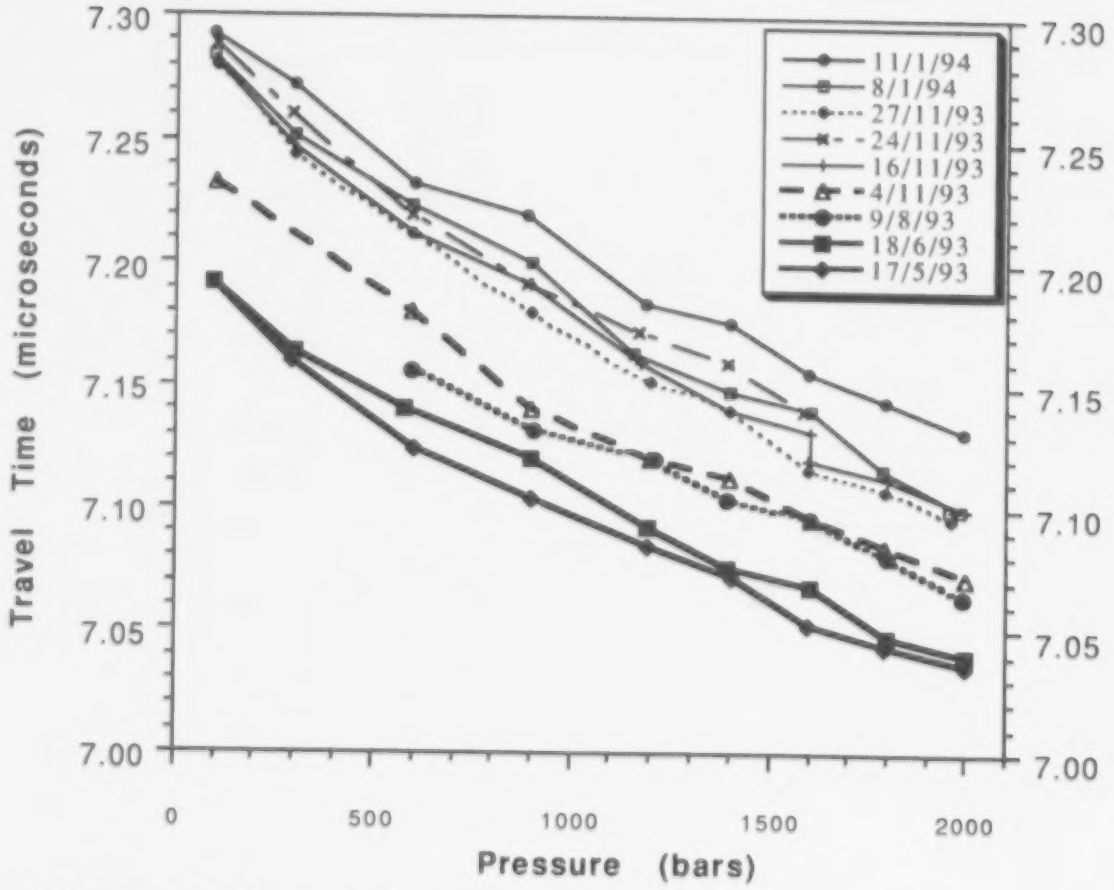

Figure 3.9 . End cap calibrations. The legend displays the dates of the calibration runs.

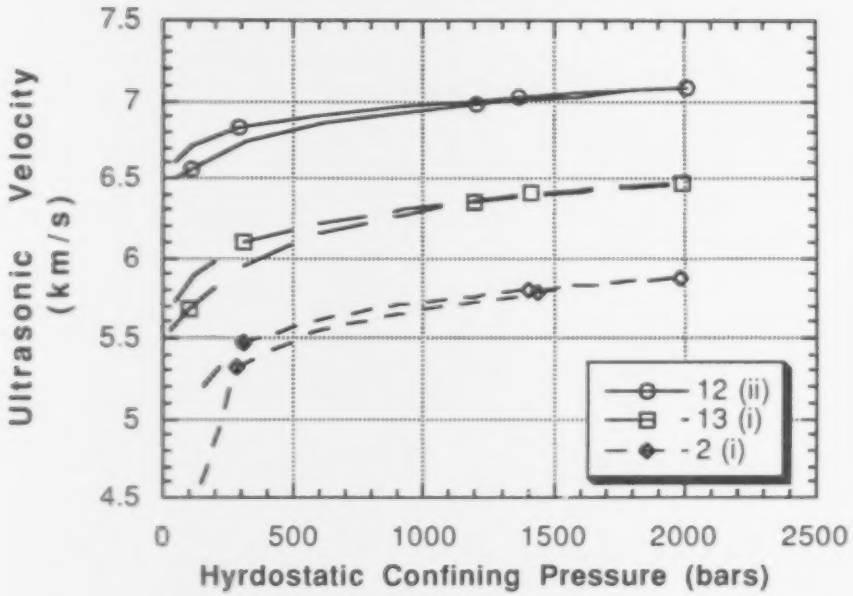

Figure 3.10 . Velocity vs. pressure for three cores. In each case, the lower curve represents pressurization and the upper depressurization.

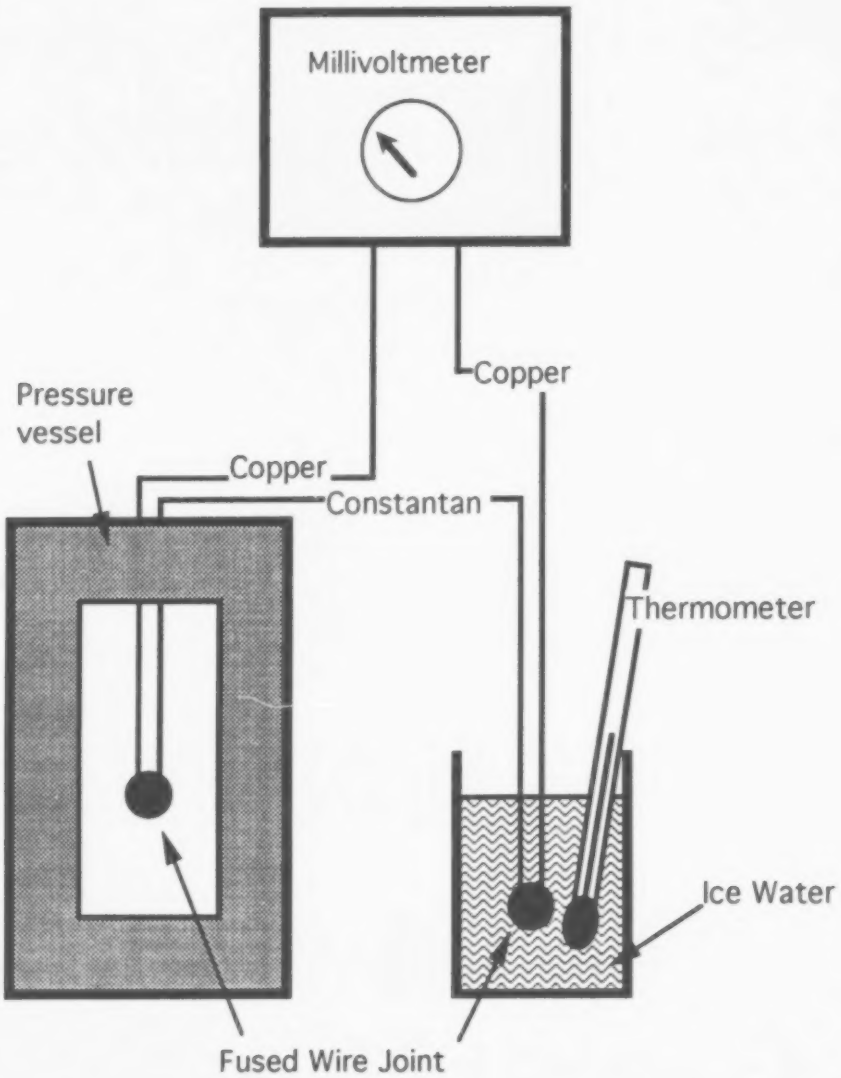

Figure 3.11 . Temperature measurement. Thermocouple arrangement is set up with copper and constantan wires. The fused wire joint in the pressure vessel moniters temperature by a calibrated relationship with the millivolt reading. A second fused joint is the reference junction maintained at 0 °C by ice water and monitored by a thermometer.

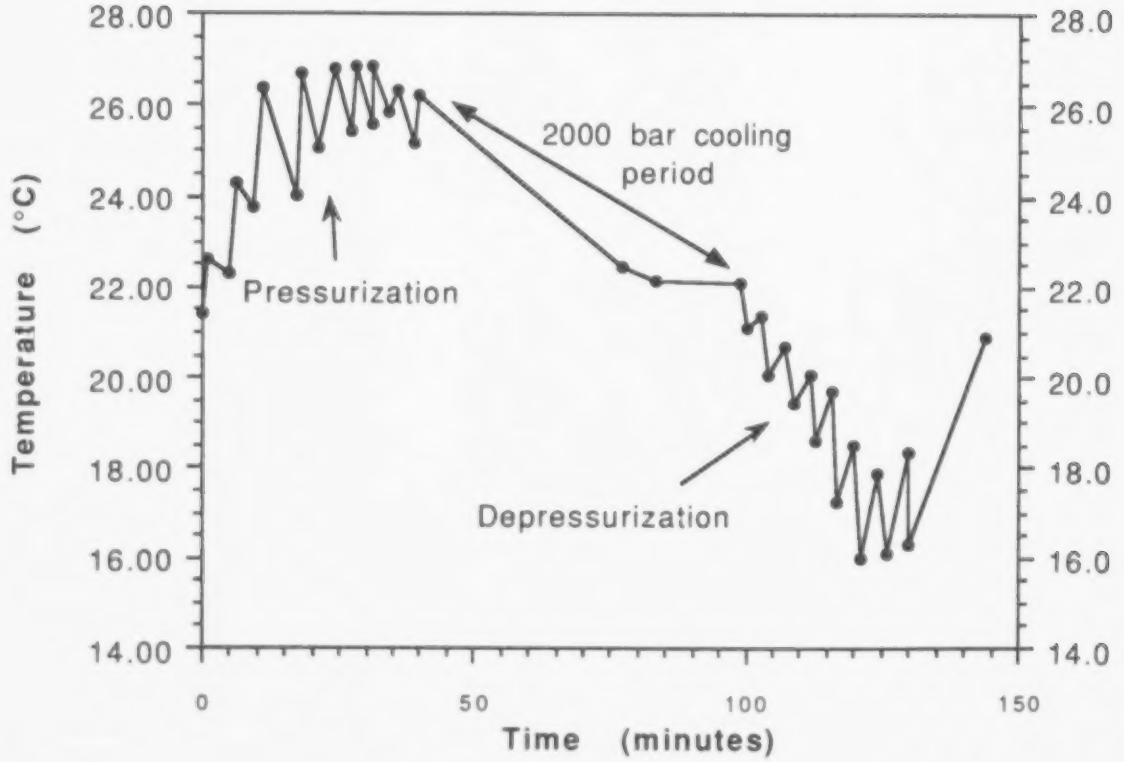

Figure 3.12 . Observed temperatures during pressurization and depressurization. Thermocouple response is shown with readings taken both directly after a pressurization and again three to four minutes later. At 2000 bar pressure the system was left to thermally equilibriate for one hour at constant pressure before depressurization.

Table 5. Mineral point count

	Percentages of mineral components										
Sample	Qrtz	Plag	Btite	H-bl	Garn	K-sp	CPX	Silm	Acsr	Opq	Altn
34	34.9	52.0	8.2	2.3	----	1.4	0.2	----	0.2	0.1	0.6
33	----	47.0	----	35.5	----	0.6	15.5	----	1.5	----	----
32	2.5	61.8	1.0	27.3	----	5.2	----	----	2.0	0.1	----
16	17.6	69.0	0.1	8.0	----	1.1	----	----	2.3	1.8	----
15a	6.6	60.1	10.1	10.0	----	10.9	----	----	1.5	0.8	----
13	23.6	61.3	4.2	1.8	----	8.9	----	----	0.3	----	----
12	2.7	43.2	4.7	46.9	----	2.2	----	----	----	0.3	----
11b	24.4	52.5	23.0	----	----	----	----	----	----	----	----
10	19.7	22.8	31.9	----	5.3	----	----	----	----	0.6	----
9	14.0	59.5	17.1	4.8	----	0.6	----	----	3.3	0.3	0.4
8	4.1	66.6	9.5	18.2	----	----	----	----	----	1.6	----
7	24.8	51.7	18.3	----	2.5	----	----	----	----	2.8	----
6	7.6	56.5	9.7	20.9	----	1.5	----	----	3.9	----	----
5	40.2	40.3	19.1	----	----	----	----	----	----	0.4	----
4	41.9	32.8	16.5	----	2.7	----	----	4.2	----	1.5	0.5
3	33.3	47.3	13.6	----	3.8	----	----	----	----	1.6	0.4
2	----	25.5	25.2	49.3	----	----	----	----	----	----	----
1a	41.8	35.4	19.9	----	1.8	----	----	----	0.5	0.6	----

Symbol Explanation: Qrtz=Quartz, Plag=Plagioclase, Btite=biotite, H-bl= Hornblende, K-sp= potassium feldspar, CPX=Clinopyroxene, Silm= Sillimanite, Acsr= Accessory (such as zircon and apetite), Opq= Opaques (such as magnetite and zircon), Altn=Alteration. The dashed lines show there is no amount of the respective mineral present.

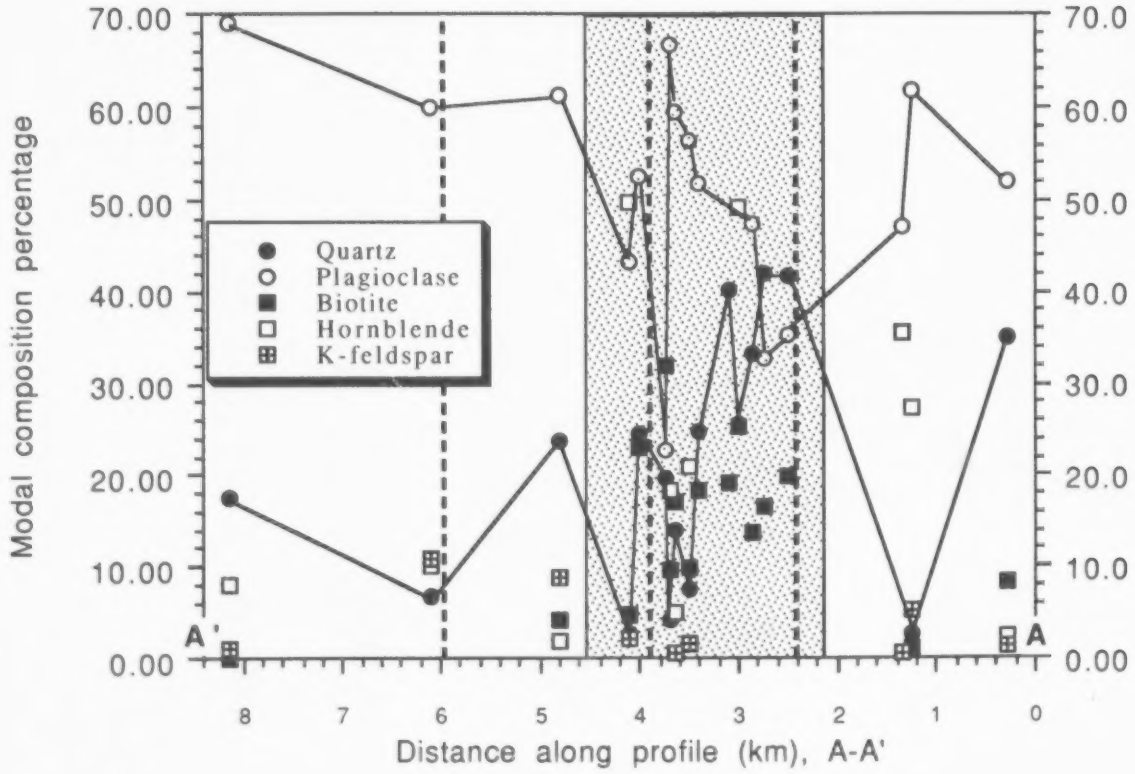

Figure 3.13 . Mineralogy of the rock samples, shown in a spatial distribution. Only the major mineral modal percentages are shown, described in the legend and the trends of plagioclase and quartz are clearly marked. Distances are measured along highway 106 relative to the metasediment contact of the east side on the easterly granodiorite. The shaded area represents the metasedimentary band and the dashed lines the shear zones.

CHAPTER 4

Results

4.1 Introduction

In this chapter the seismic data is interpreted in light of the laboratory velocity, impedance and mineralogy measurements from the surface sample rock cores. Additionally, with relevant mapped geologic data the seismic reflections [figure 1.2] can be constrained as to their positioning and to some extent their geologic origin. As will be shown, the candidate geologic structures which are the source of the seismic reflections include contrasts in properties due to: 1) differences between the granodiorites and metasediments, 2) influences of various modes of deformation on the rock, and 3) frequent changes in the properties within the metasediments.

In order to analyze how the seismic data will be affected by the variations in physical properties of the sample rocks, some parameters must be derived. With reference to section 2.10 the characteristic wavelengths of the seismic signals traveling through the earth must be known in order to understand to what spatial resolution the geologic structure may be imaged. In the present study the upper frequency of the seismic vibrator source is 56 Hz and this corresponds to a Rayleigh resolution limit of 0.0128 seconds of TWTT [section 2.10]. This combined with the average velocity of 6.08 km/s of the core samples aligned in the direction of the seismic ray propagation indicates that structures which are 39 meters thick normal to the reflecting structure should be able to be individually resolved.

The predominant wavelength of the seismic signal is 150 meters [section 2.10]. Structures much smaller than this characteristic wavelength are collectively homogeneous to the propagating elastic wavelet, and through a series of such closely spaced structures

the seismic ray will travel at some averaged velocity. This wavelength phenomena also needs to be considered in ultrasonic velocity measurements. For example, if the metasedimentary units have mineralogical variations substantially larger than the size of the core, such as large quartz veins, the structure may be inadequately sampled by a test piece of core dimension. In comparison, the seismic source has a dominant wavelength much larger than the dimensions of the cores and will pass through such structures with some averaged velocity function.

When interpreting the ultrasonic data, up to three sets of orthogonally oriented core are measured from candidate samples. However, the first arrival seismic ray paths essentially travel at normal incidence to the expected geologic structures (and hence foliations) as previously discussed in chapter 3. This suggests that core oriented perpendicular to foliation should provide the most appropriate velocity data to use in relating the ultrasonic to seismic measurements. Consequently, most of the following discussions will focus on measurements of these core aligned perpendicular to the plane of foliation.

4.2 Spatial impedance distribution

The spacing and contrast of differing rock types, and hence elastic impedances, are important in determining the character of an observed reflected seismic trace. In order to better display these, spatial impedance distribution plots of figures 4.1 and 4.2 were derived from velocity data measured at pressures of 2000 bar where the rocks display a near linear velocity-pressure relationship and thus minimal micro crack porosity effects [section 3.4]. Several interesting trends are seen in these figures which help describe the features of the seismic profile. Figure 4.1 shows the full data set from all of the core samples and figure 4.2 shows data only from core aligned perpendicular to foliation.

These graphs show the spatial distribution of the impedances of the metasediments and granodiorites along the seismic profile. Their relative lateral positions in the graph are determined from their projected distances west along highway 106 from the most easterly contact of the east pluton marked as "A" at CDP 1645 [figure 1.3], which is the origin in these figures. Most of the samples were collected immediately adjacent to the highway in road side exposure, but a few of the samples (1a, 2, 3, 4 and 5) sampled along a small side road to Granite Lake were up to one kilometer removed. Under the assumption that the geologic contacts are also perpendicular to the highway, figures 4.1 and 4.2 demarcate the spatial position of the samples perpendicular to the road measured relative to position "A".

The impedance measurements in figures 4.1 and 4.2 are taken directly from Table 3. The uncertainties shown result from the propagation of the sample dependent density uncertainty and the estimated 2% velocity repeatability uncertainty. These values represent extreme limits, as both the density and the velocity uncertainties assume worst possible cases. However, the data are sufficiently accurate to illustrate the major impedance differences, where the trend in the impedance is large relative to each sample's individual uncertainty.

A preliminary examination of figures 4.2 suggests that there are two possible causes of the central reflector "a" seen in figure 1.1 . Firstly, a large impedance contrast is seen at the granodiorite-metasediment contacts and these differences are of a sufficient size to produce a seismic reflector. Secondly, suitably large impedance contrasts exist within the metasedimentary layers and these may cause interference or tuning effects. However, a full analysis of these graphs are detailed later in the chapter.

4.3 Velocity, density and mineralogical variations

Figures 4.3 and 4.4 are plots showing the spread of velocity and density measurements for all the core samples regardless of the core orientation, and for those core samples oriented perpendicular to foliation, respectively. These figures are cross plots of the velocity and density of the samples with lines of constant impedance superimposed. Ellipses surrounding the individual datum display the error associated with the bulk density and compressional wave velocity. In theory, when evaluating a seismic reflector between two types of rocks forming a sharp contact, the strength of the reflector will be dependent upon the number of constant impedance lines which separate the two samples in the plot. As the lines of isoimpedance trend from the top left to the bottom right of figure 4.3 the largest reflections are produced at rock interfaces separated on the graph in a bottom left to top right direction.

On first examination of figure 4.3, a difference in clustering positions between the granodiorites and the metasediments is observed. Generally, the granodiorites are of moderate velocity and relatively low densities compared to the surrounding metasediments of slightly higher densities. In figure 4.4, the perpendicular aligned cores show granodiorite velocities of between 5.8 to 6.6 km/s and densities between 2630 and 2830 kg/m^3, with the metasediments having slightly lower velocities of 5.6 to 6.4 km/s and higher densities of 2690 to 2930 kg/m^3. As a reference it is noted that the average velocity of the whole suite of rocks in the direction perpendicular to foliation is 6.08 km/s.

The mineralogical differences in the metasediments are displayed in Table 5. Below, the mean percentage modal composition of the 12 metasediments are as follows, with the errors of one statistical standard deviation from the 12 sample data set:

Plagioclase	58.5 ± 7.8%
Hornblende	14.5 ± 14.0%
Quartz	14.2 ± 13.6%
K-feldspar	4.7 ± 4.4%
Biotite	3.9 ± 4.4%

Clearly, plagioclase is the major mineral component in the metasediments. All the other minerals occur in widely varying amounts relating to the percentage deviations of the mineral compositions being as large as the denoted average value themselves. This is not surprising as the metasediments of the Amisk and Missi groups have different sedimentary origins and depositional regimes. The Amisk was formed from volcanic ash and clasts which settled out in the marine type environment of the Hudson basin, whereas the Missi rocks were formed from erosional deposits of fast flowing rivers into the edge of the Hudson basin overlaying the Amisk rocks.

The modal mineralogy of the granodiorite plutons is shown below:

Plagioclase	44.5 ± 13.7%
Quartz	21.2 ± 15.6%
Biotite	17.4 ± 7.5%
Hornblende	11.7 ± 18.6%

These granodiorites show less statistical modal variations than the metasediments, as might be expected from the plutonic origins of these rocks. That is, each pluton crystalized at the same geologic time from the same basic reservoir of magma and as a result should be relatively homogeneous.

4.4 Formation of reflection coefficient profile

Reflections seen in seismic profiles are produced primarily at interfaces between rocks of different impedances. Using surface sample impedance and spatial positioning data, one can formulate a reflection coefficient profile in depth based on the positioning of these reflections between adjacent surface core samples. The spatial positioning of the reflection coefficients in Table 6 somewhat arbitrarily places the reflections at the mid-points between two 'adjacent' rock samples. As the seismic reflections are assumed to be nearly perpendicular to the foliation, the perpendicularly aligned cores of the rock samples are used in the calculations. The relative distances of the samples along the seismic profile was measured from position A at CDP 1645 [figure 1.3] in the horizontal direction. From this, the vertical distances to the dipping reflectors were calculated using an approximate 22° dip of the major structural layers. At the mid-points between surface samples the reflection coefficient of adjacent surface samples are calculated from equation (1) [section 2.7] on the assumption that these two candidate samples form homogeneous blocks and join at a sharp contact positioning the reflector.

Some caution is required when relating the actual direction that the seismic wave travels in our test area, to that displayed in the seismic section which has been migrated. The migration process accounts for rays reflected from dipping, nonhorizontal, interfaces. As previously indicated the first reflection arrival follows a path aligned perpendicular to the inclined plane of foliation. However, seismic profiles display traces vertically at the position that the seismic energy is observed and this has the consequence that a reflection seen in the seismic section does not come from a point directly below the plotted position. Migration adjusts the inclined ray path to a fictitious vertical alignment to make it representative of a *point* reflection positioned on the inclined plane vertically below the shot point/receiver position described in figure 4.5 . One can see that in comparison of the

migrated seismic data to the laboratory derived impedances, the vertical distance to the reflector and not the normal distance from the reflector is required.

Before the observed seismic data may be modeled, one must calculate the arrival times of different reflections, and to do this a velocity vs. depth function must be found using the core sample velocities. The simplest model consists of discrete velocity layers as shown in figure 4.6 . The core velocity is assumed to be representative of constant velocity layers, and the reflecting interfaces map to depths at the midpoints between adjacent samples. Therefore, by dividing twice the vertical width of a block projected to the vertical (assuming the calculated dip of 22°) by the velocity of the sample, the interval two way travel time (TWTT) over that segment may be calculated. The sum of adjacent travel times to other inferred geologic interfaces produce a series of potential TWTT reflected arrivals and this can then be compared to the TWTT positions of the reflectors on the actual seismic section [figure 1.2]. These travel times and the expected reflection coefficients are provided in Table 6. For example in Table 6 the interface between samples 33 and 1a provide a normal incidence reflection coefficient of -0.075 at a vertical interval depth of 0.78 km. A resulting interval travel time of 0.079 seconds was calculated for a wave to traverse from the overlaying sample 32-33 interface to the 33-1a interface. This time was then added to the two other more shallow interval transit travel times of 0.068 and 0.105 seconds to arrive at a total TWTT to the 33-1a reflector of 0.252 seconds. This calculation proceeds downward in a layer by layer approach until all the reflection coefficients are located in time.

4.5 Description of seismic data

The present research seeks to aid in the determination of the source of the seismic reflections. Consequently, it is important to first look for any correlations between the surface geology and the observed seismic sections.

Figures 1.2 and 4.7 show the seismic profile at different scales with the former being large scale and the latter displaying a more detailed view. The principal eastwards dipping reflector "a" is clearly shown on both. The series of parallel reflectors lie with a vertical extent of approximately 0.22 seconds TWTT and hereafter such coherent sets of reflectors are referred to as a seismic *packet or package*. Other reflection packets seen in the near surface seismic data have been denoted as "b" and "c" [figure 1.2] and these extrapolate at the surface to the mapped contacts of the metasedimentary layers to the west and east of the two large granodioritic plutons seen in figure 1.3 .

The extrapolations of the eastward dipping reflection packets to the surface (TWTT of 0.0 seconds) described above can be seen in figures 1.2 and 4.7 . The seismic data processing involved in producing these plots involved a constant 6 km/s migration velocity which can be converted from the two way time axis to depth in kilometers by a multiplication factor of 3 km/s. The horizontal axis seen in the seismic sections is easily converted to meters as each common depth point (or trace) is spaced 25 meters apart such that the true dip can be calculated by simple trigonometry for reflection packet "a" being approximately 22° from the horizontal. Coincidentally, the 6 km/s migration velocity used to process the seismic sections closely matches the average 6.08 km/s velocity of our sample cores.

The western reflector "b" [figure 1.2] extrapolates at the surface to the westerly contact of the westernmost granodiorite body at CDP 2000 as illustrated in figure 1.3 . The eastern reflection packet "c" surfaces at the eastern edge of the eastern granodiorite between CDP 1645 and CDP 1590 as seen in the detailed seismic profile [figure 4.7].

The seismic package we will be looking at in detail in this chapter is denoted "a" in figures 1.2 and 4.7 . At depths of 0.5 seconds and greater the deep part of reflector "a" is a large coherent packet of strong parallel reflectors denoted a(ii) [figure 4.7] and is of 0.22 seconds vertical extent. The near surface reflectors defined as a(i) [figure 4.7] extrapolates to the east and west contacts of the central metasediment bands with the surrounding granodiorites (± 200 m) at CDP positions 1813 and 1748, respectively [figure 1.3]. The top of this reflective package contains the strongest reflectors and these extrapolates to the approximate vicinity of the Ma-Mp contact and the central shear zone near CDP 1755 in figure 1.3 . The exact surface locations of the extrapolations are difficult to pinpoint as the reflectors are not all completely straight with many small angular deviations. Generally, however, the regional dip of 22° appears to be relatively uniform for the near surface reflection structures.

A second but less well defined structure "s" [figure 4.7] merges with the larger packet "a" at depths of 0.5 seconds TWTT and reaches the surface at CDP 1850 within 400 meters of the Granite Lake shear zone [figure 1.3]. This reflection is at a slightly different angle to the other near surface reflection, a(i), and is only two cycles wide. The geologic map of figure 1.3 shows the Granite Lake shear zone to be north-south trending and subparallel to the northwest-southeast striking metasedimentary bands and shear zones. This difference in strike suggests that there may have been a difference in the stress orientations between the time of the shear regime in which the Granite Lake shear zone was formed and that of the structural deformation of the metasediments. Indeed, the Granite Lake shear zone is inferred to have been was formed by the NW-SE crustal shortening D7 regime which followed the deformation phases forming the present metasedimentary structures. The D7 event took place at relatively cool temperatures of 250°C, resulting in the brittle shear faulting in contrast to the ductile shear regimes of the earlier D3 to D6 events. Therefore at depth it is entirely possible that this brittle shear zone may dip at a different angle to the metasedimentary band structures.

The correspondence between the seismic reflections and the surface outcrop may define the primary cause of the central near surface reflection "a", figure 1.2 and 4.7. Also, the secondary near surface reflection packet "s" appears in the locality of the westerly Granite Lake shear zone and joins the main "a" reflection package at 0.5 seconds of two-way travel time. Furthermore the edges of the reflection package "a" extrapolate to the approximate contacts between the metasediments and the two bounding granodioritic plutons.

4.6 Constraining the metasedimentary reflection package

Table 7 shows the reflection coefficients produced by imaginary contacts between surface rock samples and these reflections are arranged according to their relative distances along the profile A-A'. The positioning of large reflection coefficients between surface samples should relate to large reflective events seen in the seismic profile. In particular, this section attempts to constrain the edges of the metasedimentary reflection package a(i) [figure 4.7] to the sampled surface geology. Further, this section explains how large a reflection coefficient must be in order that an observable seismic reflection is seen, and also discusses effects of inadequately sampled surface geologic structure.

A significant problem with our procedure is associated with the spatial separation of representative samples along the seismic profile which for the most part is controlled by the existence of outcrop. If two adjacent samples are widely separated on the surface then the area between may have buried contrasts in the rock properties. Therefore, as many different geologic units as possible were sampled to ensure a representative collection of impedances along the profile.

The easterly granodiorite pluton contains two samples, 32 and 33, which represent a small Gdb granodiorite band [figure 1.3] within a much larger Gdh granodiorite unit. It is

important to ascertain how deep this Gdb granodiorite body extends in order to see if it is a cause of any of the deep reflections seen in the seismic sections.

In the case of the sample 33 - 1a interface there is both a large separation between samples (1.15 km) and a presumed mineralogical change of the interlayered Ai Amisk unit and the Gdh granodioritic rock [figure 1.3]. Granodiorite sample 33 was found in a Gdb body [figure 1.3], but is surrounded by the Gdh granodiorite. Therefore, the large negative reflection coefficient, -0.075 [Table 6], associated with the 33 - 1a interface may be misrepresentative of the impedance contact between a Gdb body (sample 33) and a metasedimentary body (sample 1a). What is mapped between samples 33 and 1a [figure 1.3], are contacts between the Gdb and the main Gdh bodies, with a further Gdh granodiorite-metasediment contact. If one assumes that the easterly (Gdh) granodiorite pluton is totally represented by sample 34, then one gets reflection coefficients of -0.01 and -0.64 associated with the granodiorite-metasedimentary boundary and that of the Gdh-Gdb granodiorite boundaries, respectively, in the region between samples 1a and 33. In comparison, Rey et al. (1993) suggests from previous studies [Velzeboer (1981)] that reflection coefficients visible at the surface are commonly 0.036 in *shallow borehole depths*. This value was obtained from comparing a logged borehole data set passing through sedimentary structures to a reflection seismic profile shot in the same area. The Granite Lake test site comprises of metamorphic and igneous rocks, therefore, the reflection coefficient of 0.036 is only used as a representative bench mark value for the size of reflection coefficients which are visible at the surface. Using this criterion the representative samples from granodiorite metasediment boundary produces a relatively insignificant reflection coefficient of -0.01. The first significant impedance contrast occurs at the sample 3-4 interface with a reflection coefficient of 0.04. This interface is therefore postulated to constrain the easterly edge of the seismic reflection package "a" [figure 4.7] which is reemphasized by the fact that this interface is positioned within a

100 m of the surface seismic extrapolation of the reflective package "a" at CDP 1748 [figure 1.3]

The larger scale seismic section of figure 1.2 shows no distinct reflectors within the near surface region between reflectors "a" and "b". This "transparent" region corresponds with the eastern granodioritic pluton, indicating that there is insufficient contrast in impedances within this body to produce reflections. Therefore, the large reflection coefficient of -0.064 at the Gdb-Gdh interface (between samples 33 and the representative sample 34, respectively [figure 1.3]) either does not propagate to the depths observed in the seismic section or is a result of a higher than typical velocity in sample 34 due to its anomalous hornblende content [Table 5].

The western edge of the reflection package "a" extrapolates to CDP 1813 in the locality of the western side of the metasediments at the granodioritic pluton contact [figure 1.3]. The obvious correlation of the seismic reflector to a surface sample interface would be between samples 13 and 12 [figure 1.3], but the associated reflection coefficient of -0.025 does not satisfy the 0.036 resolution criterion. Therefore, we assume the seismic extrapolation to surface was not entirely accurate in this case. The likely alternative occurs at the interface between samples 12 and 11b with a reflection coefficient of 0.078, 350 m east of CDP 1813.

With the edges of the metasedimentary reflector constrained one can assess the synthetic vertical depth of the seismic reflector a(i) [figure 4.5] using the data from Table 6. The result yields a reflection package with its top at the sample 3-4 and its bottom at the 12-11b interface of 0.23 seconds in vertical extent . This is in excellent agreement to the 0.22 seconds observed from the seismic section [figure 4.7].

4.7 Introduction to shear zones

Shear zones are the result of two blocks of material moving past one other along a line of discontinuity. The type of deformation can either be ductile, whereby the rock is sufficiently hot that it behaves as a plastic solid, or brittle if the rock is cool enough that it breaks instead.

Ductile shear zones are formed in rock at high temperatures in excess of 350 °C for granitoid rock. At these temperatures quartz plastically deforms and flows under shear stress. Other minerals such as feldspars remain brittle and often fracture at these temperatures [Rey et al. (1993)]. These ductile zones are recognized by the gradual reduction in mineral grain size as the region of the most severe deformation is approached. At high temperatures above 550 °C both quartz and feldspar are ductile, however, the quartz has a lower viscosity and this contrast in viscosity results in a foliated structure which is apparent after cooling. Brittle shear zones form at cooler rock temperatures, much below 300 °C [Rey et al. (1993)], whereby all the constituent minerals are brittle and fracturing pervades the rock structure. However, the fracturing happens in a far more localized area than the further ranging ductile shear zones [Scholz (1992)].

Rey et al. (1993) observed that shear zones have associated velocity gradients with a lower material velocity observed as one approaches the locus of the shear zone. Indeed, Rey et al. [1993] proposed that changes of velocity between sheared and unsheared granitoid rock may be as large as 11%.

Both types of shearing regimes are present in the Granite Lake test area. Within the metasediments there are two ductile shear zones referred to henceforth as the "eastern" shear zone 200 m west of CDP 1748 [figure 1.3] and the "central" shear zone approximately 700 km east of CDP 1813. Also, a third *brittle* shear zone, the Granite Lake shear zone, is represented by sample 15a within the western granodiorite pluton.

Both the central and eastern shear zones were formed during metamorphic deformation at temperatures near 550 °C [Gordon et al. (1993)] and both exhibit the features of a ductile shear zone described above. The western "Granite Lake" shear zone occurred during the later D7 phase of tectonic activity when temperatures in this locality where around 250 °C [personal communication Ashton (1994)] and thus brittle deformation was dominant.

4.8 Eastern metasedimentary shear zone

The eastern shear zone is contained within a single "Missi" unit of rocks within the banded metasediments. Samples 1 through 5a were all were taken from a 350 m interval, measured along the highway in a "Ma" Missi group [figure 1.3]. As a result, the impedance response of this shear zone is unrelated to the mineralogical changes of other geologic units. This grouping of impedances displays a trend with decreasing values as one approaches the easternmost shear zone. But, the trend appears to be truncated at sample 3 as seen in Table 7 or more graphically in figure 4.2 .

The impedance distribution is almost symmetric about sample 3 which exhibits a high impedance with the other samples displaying gradually lowering values to the east and west. With the exception of sample 2 the other four rocks have noticeably similar mineralogy [Table 7]. However, a decrease of relative levels of quartz and biotite with an increase in plagioclase all appear to correspond with the impedance increase towards the position of sample 3. Sample 2 was anomalous in its composition with respect to the other samples having no quartz with additional high biotite and hornblende modal mineralogy percentages.

The velocities in this Mp area [figure 1.3] are essentially constant at approximately 5.8 km/s, with sample 3 displaying a high value of 6.3 km/s. Samples 1a, 3, 4 and 5 have similar mineralogy and therefore this high velocity of sample 3 must be attributed to an

additional factor. Other differences are also apparent whereby samples 1a, 2, 4 and 5 have velocity anisotropies of over 8%, as opposed to the sample 3 with a velocity anisotropy of less than 0.1% [Table 7]. The uniform high velocity response of sample 3 indicates that it has no preferred crystal orientation or banded structure that is commonly associated with anisotropy [Birch 1961]. In contrast, the higher anisotropies of the other four samples are probably associated with shear related phenomena indicating pronounced foliation, described in the previous section 4.7, which are known to produce low velocity orientations [Birch (1961)]. This would account for the high anisotropy in samples within the sheared zones compared to the relatively unsheared surrounding rock. Additionally, one could postulate that the extent of the shear zone west of it's mapped location is less than 350 m, indeed, up to the position of sample 3 where no velocity anisotropic effects are seen. Carrying this argument further, samples 2 and 5 display substantial velocity anisotropy and relatively low velocities perpendicular to foliation which suggest that they are possibly associated with an unmapped region of anomalously highly sheared rock immediately to the west of sample 3, which may warrant further geologic mapping.

Reflection coefficients associated with the shear zones occur between sample interfaces 4-3 and 3-2 with respective reflection coefficients of 0.037 and 0.022 . Therefore, the former interface would display a reflection coefficient strong enough to be seen at the surface according to the minimum reflection coefficient criterion of 0.036 [section 4.7].

In conclusion the general trend of decreasing velocity towards the shear zone and the velocity contrast between sheared and unsheared samples are in general agreement with work performed by Rey et al. (1993) [section 4.7].

4.9 Central shear zone

Figure 4.2, displays the impedance trends in the vicinity of the central shear zone where there is both a progressive reduction in impedance and velocity values [figure 4.8] towards the shear zone again in accordance with the work of Rey et al. (1993) [section 4.7]. Sample 11b is the nearest sample to the shear zone and it displays the lowest impedance and velocity values. Reflection coefficients of 0.078, -0.043, 0.040 occur between sample pairs of 12-11b, 11b-10 and 10-8, respectively, all within 300 m of this zone. Indeed, these interfaces are spaced more than 60 m apart normal to the dipping layers and as a result satisfy the spatial resolution limit of 39 m [section 4.1]; reflections from such interfaces should be able to be recorded as events on the seismic section. This suggestion is based on the simplifying assumption of a block velocity distribution [figure 4.6] applied to this relatively sparse data set. However, as in the case of the eastern shear zone there is good evidence for a decreasing trend in the impedances which towards the shear zone, even with experimental uncertainties taken into account.

A complication with this central shear zone, however, is that the samples near this shear zone (12, 11b, 10 and 8) have varying mineralogies [Table 5] due to their differing geologic origins. Consequently, the impedance and velocity trends seen near this shear zone may have mineralogical variations superimposed upon the more structural shear deformation effects [section 4.7].

4.10 Granite Lake shear zone, and the western pluton

The western Gdh granodioritic pluton, figure 1.3, is traversed by 5 kilometers of highway 106 approximately perpendicular to its regional band like structure which is roughly parallel as mapped to the "L" shaped metasedimentary layers. Samples 13, 15a and 16 were ultrasonically tested to evaluate the seismic response of this pluton. However, sample 15a was obtained from outcrop near to the north-south trending Granite Lake brittle shear zone depicted in figure 1.3, and 400 m west of the extrapolation of the seismic reflector "s" [figure 4.7] at the surface at CDP 1850 [figure 1.3]. Therefore, samples 13 and 16 were assumed to best represent the bulk characteristics of the pluton and sample 15a was a measure of the sheared rock velocity response. Mineralogicaly, both samples 13 and 16 were similar [Table 8] except that sample 13 is more siliceous with lesser amounts of hornblende. Despite these relatively minor differences, their calculated impedances and velocities fall well within error of each other [figure 4.2 and 4.8]. Further, the relatively low velocity anisotropy of 3.6% and 1.7% of samples 13 and 16, respectively, compared to the higher velocity anisotropies seen in samples 1a-5 [Table 7] reemphasizes the homogeneous nature of these relatively unsheared sections of the plutonic bodies.

Sample 15a is located at the southern termination of the mapped Granite Lake shear zone as denoted in figure 1.3, and has a greatly lower impedance than the surrounding granodiorites [Table 8]. At face value the contrasts in impedance would produce substantial reflection coefficients of -0.049 and 0.066 between rock interfaces of 13-15a and 15a-16, respectively. However, for these two reflections to be individually spatially resolved they would have to be separated by at least 39 m [section 4.1]. As figure 4.7 shows two reflection amplitudes correlating to this surface position one must assume that the interfaces between the velocity block centered on 15a and the bounding plutons (samples 13 and 16) are spaced more than the required 39 m. Visually this rock sample

15a is similar to the neighboring samples of 13 and 16, but has a slightly more pronounced banded crystalline structure, and is also mineralogicaly similar except for its relatively low quartz levels. Also the velocity anisotropy of this sample is 5.3% which is higher than that of the unsheared samples 13 and 16, but not as high as the samples found in the eastern ductile shear zone [Table 7]. Geologically the western shear zone is determined to be a brittle feature as defined by various indicators exposed primarily on the shores of Granite Lake [personal communications, Ashton (1994)]. The brittle nature is emphasized by the lack of major foliation in the rock associated with its low value of velocity anisotropy. Therefore, the low velocity and impedance of the reflector may be associated with a mineralogic difference of the rock, combined with some small amount of shear induced foliation structure. The resulting impedance contrast produces the reflection "s" seen in the seismic profile [figure 4.7].

4.11 Multiple reflectors

Geologically the metasediments consist of several layers of differing mineralogy resulting from the variety of source rocks and styles of deposition. These are layered 100 to 725 m wide measured horizontally along the seismic section, and correspondingly 40 to 295 m in vertical extent assuming that these structures dip at 22° into the earth. This pattern of contrasting properties within the metasediments together with a predominant seismic wavelength of about 150 m [section 4.1] may result in interference, or tuning effects in the resultant reflecting trace.

Generally, the metasediments display a coherent banded structure of nearly equal width extending in a near perpendicular manner to the seismic profile for over 2 kilometers in northwest and southeast directions [figure 1.3]. In the following analysis, the surface geology will be taken as an indicative cross section of the geologic structure

at depth. Under this assumption, there are many small metasedimentary bands with contacts of unknown impedance contrasts of vertical width perpendicular to the dipping structure of: 55, 95, 45, 45, 105, 260, and 35 m which are mostly as big or larger than the 39 m spatial resolution limit [section 2.10] indicating each interface may be individually resolved. Also, maximum constructive or destructive interference effects are produced when layered structures of contrasting impedances being spaced by integer values of a quarter the predominant wavelength of the seismic signal.

4.12 Theoretical interference effects

Consider the case of three horizontal layers of impedance denoted by I_1, I_2 and I_3 lying successively beneath one another. Furthermore, assume the impedances are such that $I_1 < I_2 < I_3$ and the layers are each half a wavelength in thickness. A vertical wave traveling first through I_1 is incident upon the I_1-I_2 interface whereupon portions of the energy are reflected and transmitted according to equation (1) [section 2.10]. The transmitted wave travels through the second medium to the second interface where both reflection and transmission phenomena occur. This second reflected wave travels upwards through medium 2 along the same ray path as the initially reflected wave of the I_1-I_2 reflector. The time difference between the travel paths of the two reflected waves is one wavelength and as a result constructive interference occurs with the two waveforms resulting in a combined amplitude greater than that produced from a single reflection interface. These interference effects are further complicated by multiple reflections within the layers, which for the given example, all constructively interfere due to the integer wavelength path differences.

In the above scenario, if I_2 were changed to have a lower impedance than I_1, then the reflected wavelet from the I_1-I_2 contact would now be negative due to the negative

value of I_2 - I_1 from the reflection coefficient equation (1) [section 2.10]. Now, the resultant reflected waves off the I_1-I_2 and I_2-I_3 interfaces still have a path difference of one wavelength but the wavelets are now out of phase and cause destructive interference. Of course, if the path differences between layers are not integer values of half the predominant wavelength, partial interference takes place.

4.13 Interference effects in the metasedimentary units

Variations in the thicknesses of the metasedimentary layers with depth will produce tuning effects of the seismic signal if the layers are sufficiently thin. With non-uniform layer thicknesses, corresponding variations of path differences between reflections from the top and bottom of the layer will occur. The resultant wavelet observed at the surface is then the resultant of the subsequent levels of constructive or destructive interference. The first system of layers used in the previous discussion [section 4.12] will be used to illustrate this.

When the second layer was half a wavelength thick the superposition of the reflected waves from boundaries I_1-I_2 and I_2-I_3 resulted in constructive interference. Now, consider a case where the layers dip and their respective thicknesses vary along their length. Suppose that at a certain position along the layer, I_2 has a thickness of one quarter of a wavelength. The path difference between the top and bottom reflections in this layer is now one half a wavelength and destructive interference will occur which reduces the amplitude of the final reflected wave. The shallower reflectors higher up in a thinning, dipping structure would display tuning effects intermediate between the constructive and destructive reflection positions. Such effects are noticeable in the seismic profile [figure 4.7] where the reflection character does indeed increase and decrease in amplitude throughout its extent. For example, the reflection signal of

reflection package a(i) [figure 4.7] noticeably weakens between common depth points (CDP) 1664 to 1687. If this were associated with tuning effects then the seismic profile indicates that layered (banded) structure seen in the surface geology [figure 1.3] continues down dip and that the thicknesses of these layers vary with depth. This in itself is not entirely surprising as the present structures are a product of many deformation regimes that have folded and deformed the original sedimentary layered structure which was not necessarily a stack of uniform planar layers after its initial deposition. However, the character of the seismic reflectors a(i) and a(ii) is more uniform below 0.25 seconds (east of CDP 1750) with the sets of parallel reflectors inside the packet being vertically displaced between 0.025 and 0.04 seconds apart, corresponding to approximate vertical distances of 150 to 240 m (on the assumption of a 6 km/s average core velocity). This value is similar to the predominant seismic wavelength of 150 m supporting the suggestion that the metasedimentary layers produce substantial interference effects.

4.14 Corrections to measured velocities and impedances

All of the interpretations above were made using core velocity data measured at pressures of 2000 bar (200 MPa). This pressure is used solely on the basis that it is the highest pressure attainable with the present system and this causes the maximum reduction of the micro crack porosity resulting in near intrinsic mineralogical rock velocities. As a result the purpose of using pressure in these experiments is not to simulate the in situ conditions but to provide as defect free a sample as possible. However, in the real earth both pressure (or stress) and temperature increases with depth and it is important to determine whether neglecting these factors biases the velocity results.

The effect of pressure or confining stress on the velocities is first examined. The vertical, or lithostatic stress S_l with vertical depth z into the earth may be calculated according to:

$$S_l = g\rho_{av}z \tag{8}$$

where g is the acceleration due to gravity and ρ_{av} is the average rock density. Further, the velocity of compressional wave propagation, V_p, is described by,

$$V_p = \sqrt{\frac{K + 4/3\mu}{\rho_{av}}} \tag{9}$$

with K denoting the bulk modulus and μ the shear modulus. Using the empirically derived finite strain equations [Stacey (1992)] the shear and bulk modulus are linear functions of pressure according to:

$$\mu = \mu_0 + \mu' P \tag{10}$$

$$K = K_0 + K' P \tag{11}$$

where P denotes hydrostatic pressure, K_0 and μ_0 are the zero pressure values of bulk modulus and shear modulus respectively and K' and μ' are constants. Therefore, as seen in section 3.4, increasing pressure causes an approximately linear velocity response over the relatively small pressure ranges that occur in these laboratory experiments.

The vertical depth measured from the top of our sequence, starting at "A" [figure 1.3], to a position below sample 16 located at the far west of the westerly granodiorite is 2.8 km (assuming a dip of 22° as described earlier). Combined with the average rock density of our cores of 2.77 g/cm^3, the pressure difference between the rock at the top of the modeled sequence to the bottom is 760 bar (76 MPa). This is of relatively little

consequence as all the velocity-pressure curves of the samples as shown in the Appendix and have velocity gradients in the order of 0.1 km/s per 1000 bar at high pressure. Therefore, the percentage change of impedance associated with pressure contrast across the whole profile of 2.8 km vertical extent is less than 2%. The pressure effect on the impedance of individual samples used to calculate reflection coefficients is even smaller, as the relative depths between the representative samples is small (typically less than 300 m) and results in a velocity bias of less than 0.2% and in most cases is completely negligible.

Similar arguments can be used to neglect the effects of temperature on the velocity response of the rock. Using the approximate geothermal temperature gradient calculated for crustal rock of 6.7°C/km [Stacey. (1992)] the vertical section of 2.8 km depth would have a net temperature difference of approximately 19°C. Individual rocks adjacent to each other in sampling will have maximum temperature variations less than 2°C, with typical depths between samples of less than 300 m. Christensen (1979) measured the temperature coefficients $(\partial V/\partial T)_P$ of several igneous and metamorphic rocks which were found to vary between -0.5×10^{-3} and -0.6×10^{-3} km $s^{-1}°C^{-1}$ at 2000 bar. Therefore over the typical 2°C increase of temperature between adjacent samples, there is a corresponding velocity reduction of 0.001 km/s ($\approx$ 0.02% velocity error), further suggesting that temperature corrections are unnecessary at these relatively small depths involved in our preliminary investigation.

It must be kept in mind that what is important to the present study is the reflection response of the rock at depth and this is related to the difference in impedances between rocks at the geologic contacts. This experiment is not trying to reproduce the exact in situ conditions of the rock at depth it merely intends to constrain the position of the major reflections. Consequently, if it is assumed that most in situ factors on the rock such as lateral stress, overburden pressure and the temperature affect the rocks in a linear manner with depth then the resulting variations in these properties will have little effect on the

derived reflection coefficient values especially over the relatively modest depths from which these reflections are returned. For instance, the overburden pressure approximation may not be a sufficient approximation to the true insitu stress conditions and transverse stress may have an effect. However, the unsampled lateral stresses are assumed to vary in a somewhat constant manner over vertical profile and therefore the relative impedance contrasts and subsequent reflection coefficients will be unaffected.

4.15 Synthetic seismic

The reflection data we have acquired in this thesis is a first step to aiding the geologic interpretation of the observed reflections by both noting their strength (associated with the magnitude of the reflection coefficient) and approximate location. The edge of the reflection packets have been constrained, as well as isolated reflectors in the locality of shear zones. Ideally, to produce a representative synthetic seismogram a continuous profile with depth of both velocity and density is required. However our data set has only a few representative samples from which to produce such a profile.

For completeness, figures 4.9 and 4.10 show two possible synthetic seismograms derived from the laboratory data set. Both are formed from a simple convolution of the vibrator wavelet [equation (5)] with the reflection profiles and no attenuation or multiple reflections taken into account. The first synthetic, figure 4.9, is formed from the reflection data as displayed in Table 6. The second synthetic seismic was formed by a simple reflection model which assumed a first order approximation of averaged velocity and impedance response in the main geologic units delineated by the metasedimentary bands and the granodiorite plutons. Both originate at time 0.0 s at CDP 1645, position A [figure 1.3]. This latter profile assigned constant impedances and velocities to each granodiorite body and the banded metasediments with added features of low impedance/velocity in the

central and western Granite Lake shear zones [Table 9]. It is noticed that the TWTT of this calculated metasedimentary package is 0.21 seconds in good agreement with the 0.22 seconds seen in the seismic profiles and 0.23 seconds derived from the reflection data of Table 6. However, the metasedimentary reflection package "a" [figure 4.7] displays five or six strong reflection events (from times 0.35 to 0.57 at CDP 1645) compared to the two seen at comparable times in figures 4.9 and 4.10 . Clearly far more data would be needed to model the layered structure, such as from a borehole log, to use such synthetic seismograms in a comparative study with the real seismic data.

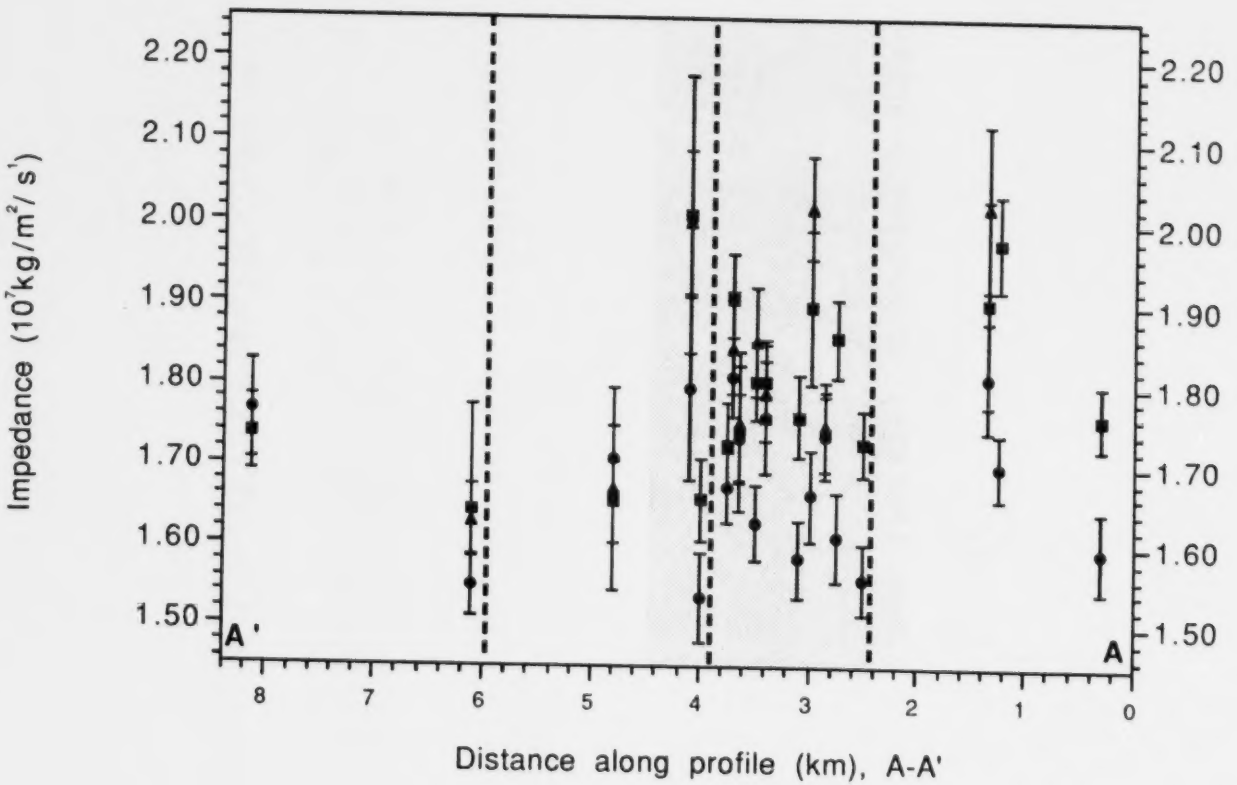

Figure 4.1 . Impedance vs. position along the seismic profile. Distances are measured along highway 106 relative to the metasediment contact on the east side of the eastern granodioritic pluton. Solid circles denote cores aligned parallel to foliation, or parallel to foliation and lineation, as in section 3.1.1 . Squares denote cores perpendicular to foliation, and triangles represent cores aligned parallel to foliation yet perpendicular to lineation. The shaded area represents the metasedimentary band and the dashed lines represent the shear zones. Impedance error bars are also shown.

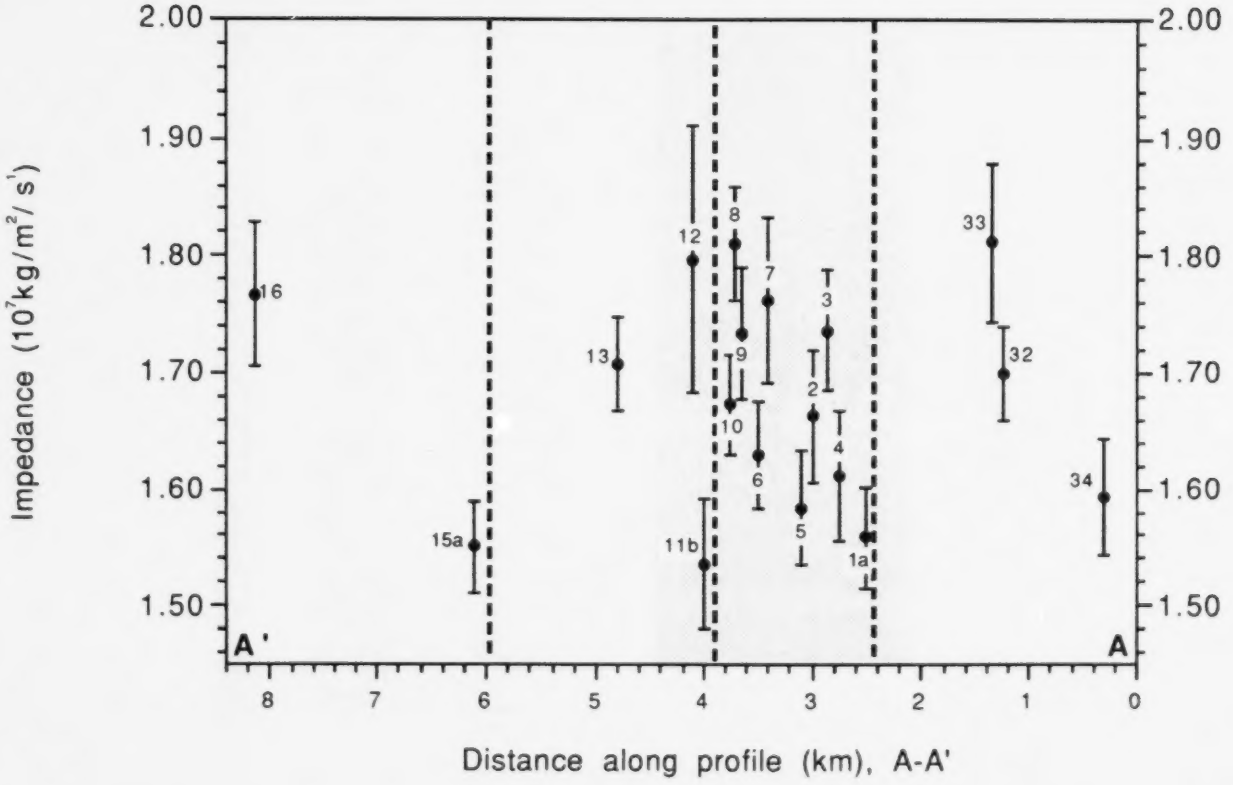

Figure 4.2 . Impedance for core aligned perpendicular to foliation vs. position along seismic profile. Distances are measured along highway 106 relative to the metasediment contact on the east side of the easterly granodioritic pluton. The shaded area represents the metasedimentary band and the dashed lines represent the shear zones. Vertical impedance errors are shown on the labeled cores.

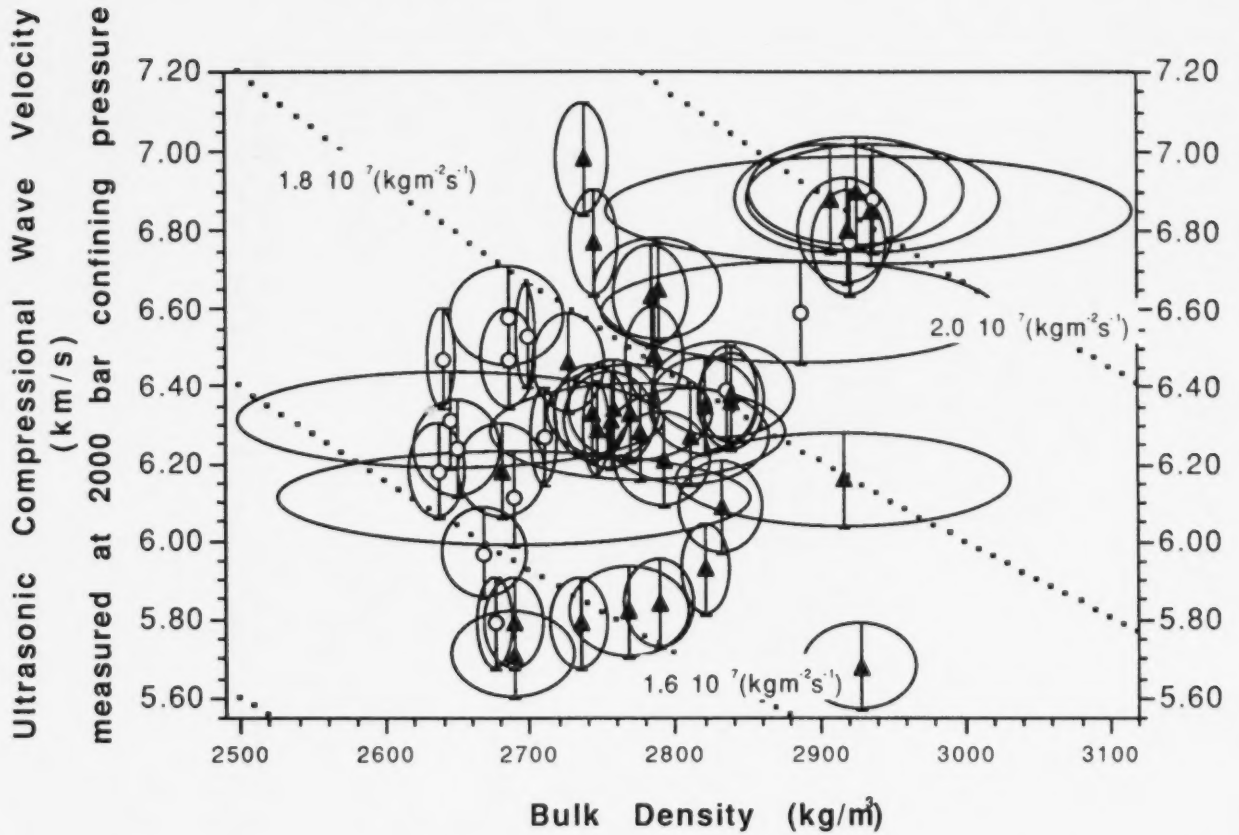

Figure 4.3 . Ultrasonic velocity at 2000 bar vs. bulk density for all the core data. Granodiorites are shown as hollow circles, and metasediments are denoted by solid triangles. Lines of constant impedance are shown as dotted lines. The axes of the ellipses indicate the uncertainties in density and velocity.

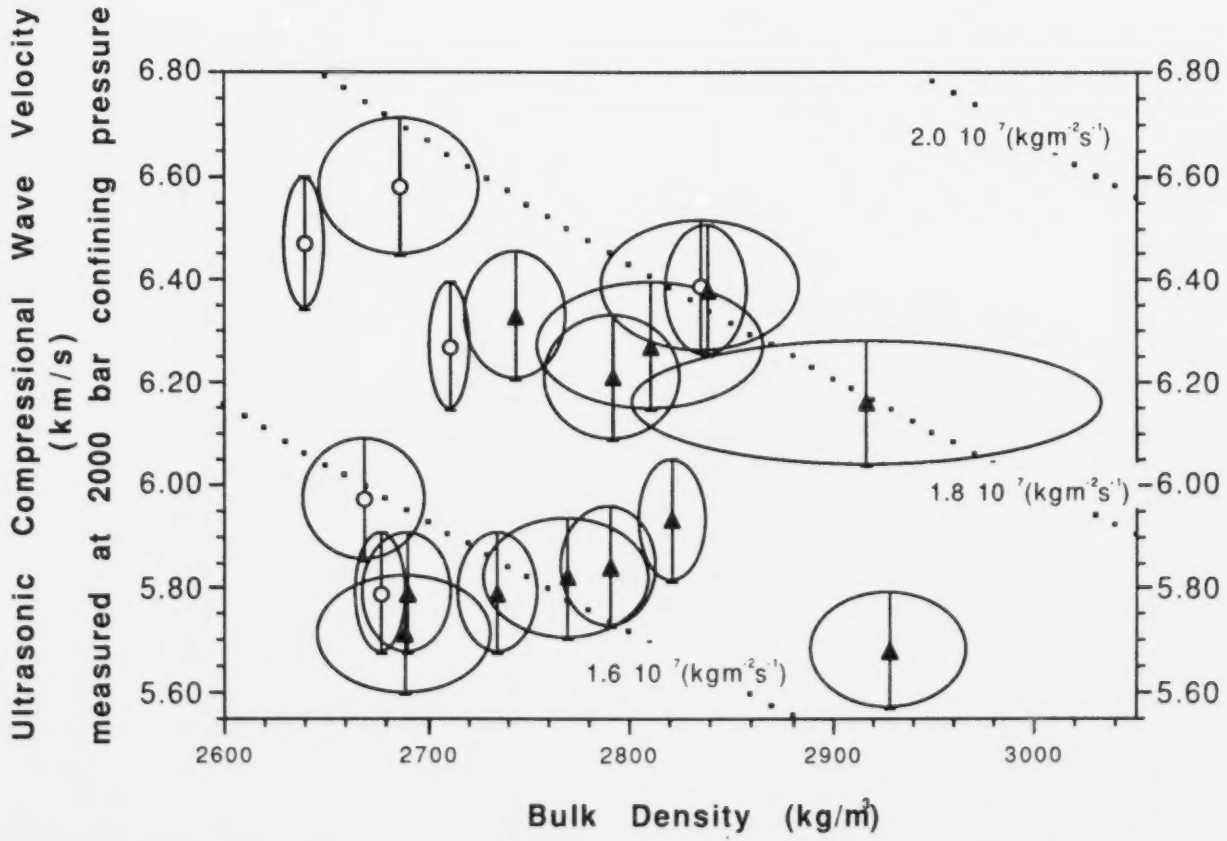

Figure 4.4 . Ultrasonic velocity at 2000 bar vs. bulk density for core alligned perpendicular to foliation only. Granodiorites are shown as hollow circles, metasediments are denoted by solid triangles and lines of constant impedance are shown as dotted lines. The axes of the ellipses indicate the uncertainty in density and velocity.

Table 6. Reflection coefficients at estimated two-way travel times.

Sample	Ultrasonic Velocity (km/s) measured at 200 MPa	Impedance (10^7) ($kg/m^2/s$) measured at 200 MPa	Impedance error (%)	Distance of Sample Impedance Along Profile A-A' (km)	Position of Reflection Coefficient Along Profile A-A' (km)	Reflection Coefficient	Depth of Reflection Coefficient Vertically from Reflector (km)	Interval Two Way Travel Time (TWTT) Vertically Between Reflectors (s)	Total TWTT to Reflector (s)
34	5.97	1.593	3.15	0.3					
					0.775	0.032	0.313	0.105	0.105
32	6.27	1.700	2.39	1.25					
					1.300	0.032	0.525	0.068	0.173
33	6.39	1.812	3.75	1.35					
					1.925	-0.075	0.778	0.079	0.252
1a	5.79	1.558	2.81	2.5					
					2.625	0.017	1.061	0.098	0.349
4	5.82	1.612	3.49	2.75					
					2.800	0.037	1.131	0.024	0.374
3	6.33	1.737	2.94	2.85					
					2.925	-0.003	1.182	0.016	0.390
2	5.9	1.728	3.35	3					
					3.050	0.013	1.232	0.017	0.407
5	6.48	1.772	2.76	3.1					
					3.250	-0.003	1.313	0.025	0.432
7	6.27	1.762	4	3.4					
					3.450	-0.039	1.394	0.026	0.457
6	5.84	1.629	2.87	3.5					
					3.575	0.031	1.444	0.017	0.475
9	6.21	1.734	3.22	3.65					
					3.675	0.022	1.485	0.013	0.488
8	6.38	1.811	2.71	3.7					
					3.725	-0.040	1.505	0.006	0.494
10	5.93	1.673	2.6	3.75					
					3.875	-0.043	1.566	0.020	0.514
11b	5.71	1.535	3.62	4					
					4.050	0.107	1.636	0.025	0.539
12	6.16	1.797	5.99	4.1					
					4.450	0.079	1.798	0.053	0.592
13	6.47	1.708	2.41	4.8					
					5.450	-0.049	2.202	0.125	0.717
15a	5.79	1.550	2.49	6.1					
					7.125	0.066	2.879	0.234	0.951
16	6.58	1.767	3.48	8.15					

The velocity and impedance measurements are taken from cores oriented perpendicular to foliation. Distances along A-A' refer to positions along highway 106, as shown in figure 1.3. Travel time calculations using a discrete velocity function , with the 0.0 second reflector corresponding to surface position A [figure 1.3].

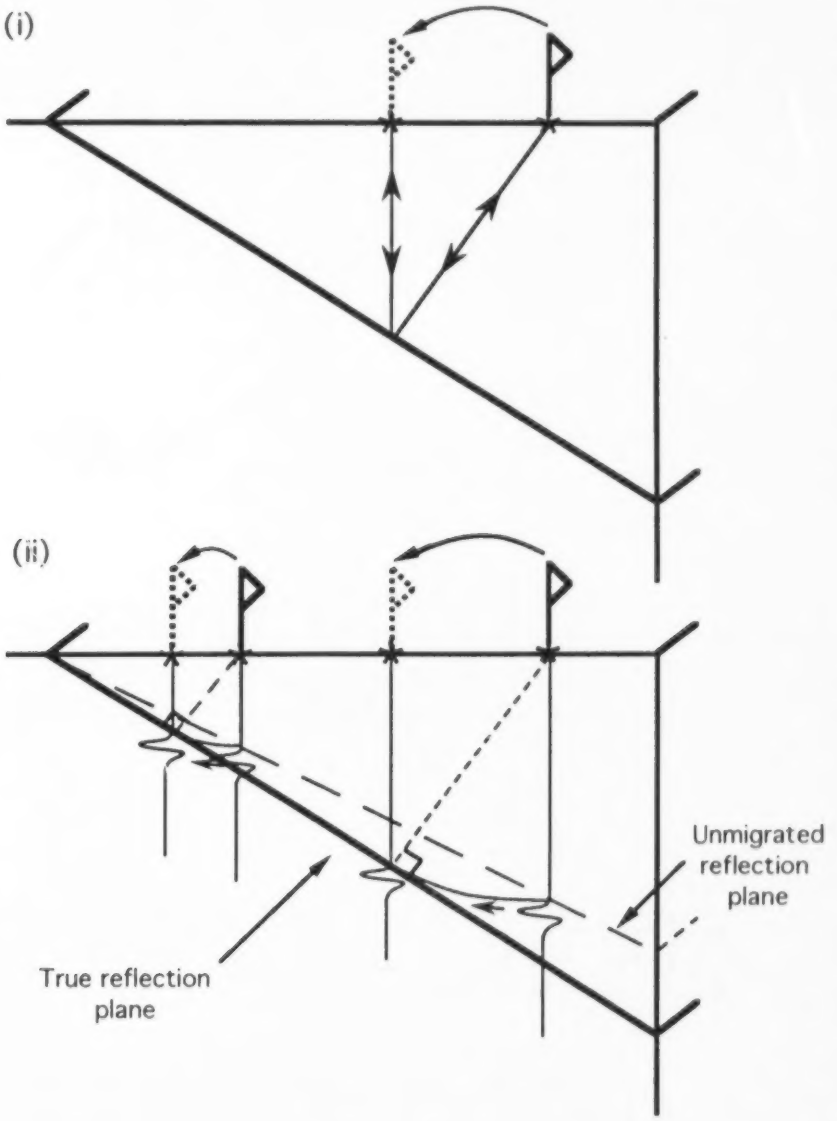

Figure 4.5. Seismic migration effects. In diagram (i) the solid flag represents the position of a true ray path from source to receiver which is normally incident to the dipping reflection interface. The dashed flag represents the artificial ray path of vertically oriented migrated ray. In diagram (ii), the solid flags have the unmigrated reflection response, corresponding to normally incident rays of (i), which are swept on a radius until they form tangents with the inclinded reflection plane. The dashed flags now display migrated seismic traces, corresponding to the artifical vertical ray paths in (i), at their new migrated lateral offsets.

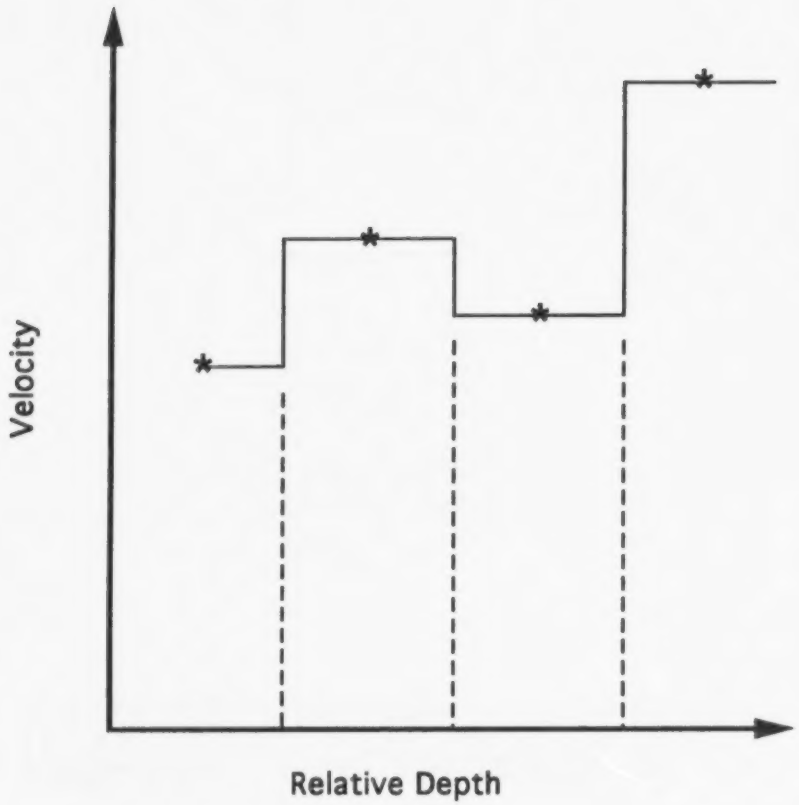

Figure 4.6 . Schematic of reflector positioning. A velocity profile is shown at increasing values of depth. The '*' denotes the velocity of a given core and the dashed lines show the placement of the reflector mid-way between core positions. The depth axis can be converted to a time scale with the discrete velocity function .

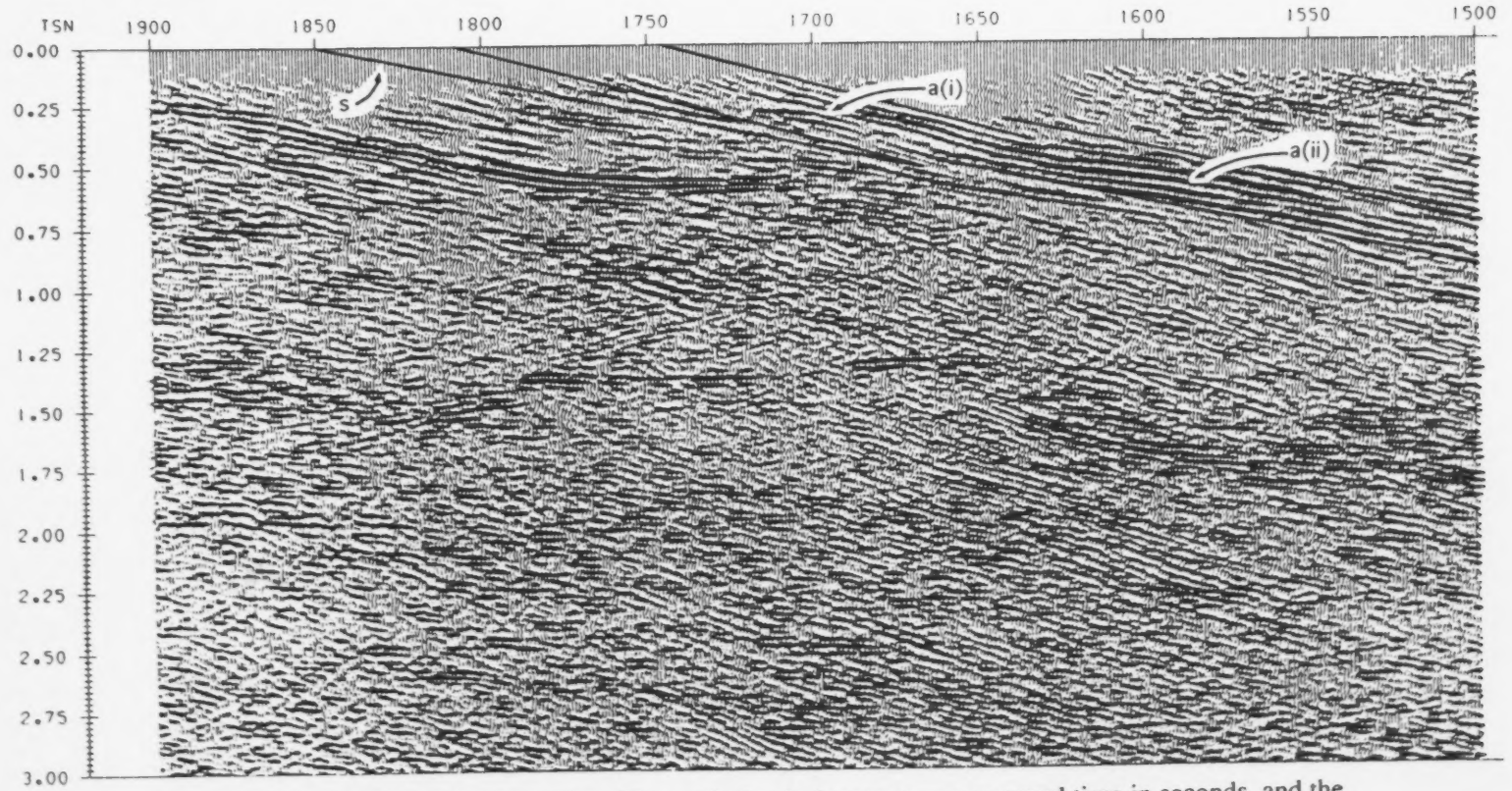

Figure 4.7 . Detailed seismic section. The vertical axis denotes two way travel time in seconds, and the horizontal axis is the common depth point position (CDP) spaced 25 metres apart along highway 106 . The major reflection packet studied in the thesis is denoted as a(i) and a(ii), the near surface and deeper parts of the reflection packet, respectively. The proposed seismic response of the Granite Lake brittle shear zone labeled is "s", and extrapolates to CDP 1850, whereas a(i) extrapolate to a surface position between CDP 1813 and CDP 1748.

Table 7 Shear related phenomena

Sample	Distance along profile A-A' (km)	Modal mineral composition (%) Qrtz	Plag	Btite	H-bl	Garn	Velocity (km/s)	Impedance ($kgm^{-2}s^{-1}$) (10^7)	% Velocity Anisotropy
5	3.1	40.2	40.3	19.1	---	---	5.79	1.58	11
2	3	---	25.5	25.2	49.3	---	5.68	1.66	20
3	2.85	33.3	47.3	13.6	---	3.8	6.33	1.74	<0.1
4	2.75	41.9	32.8	16.5	---	2.7	5.82	1.61	15
1a	2.5	41.8	35.4	19.9	---	1.8	5.79	1.56	8
Shear Zone	2.4	---	---	---	---	---	---	---	---

A-A' refers to positions from figure 1.3 . Qtrz = Quartz, Plag = Plagioclase, Btite = Biotite, Garn = Garnite. Velocity and impedance are evaluted at 2000 bar confining pressure.

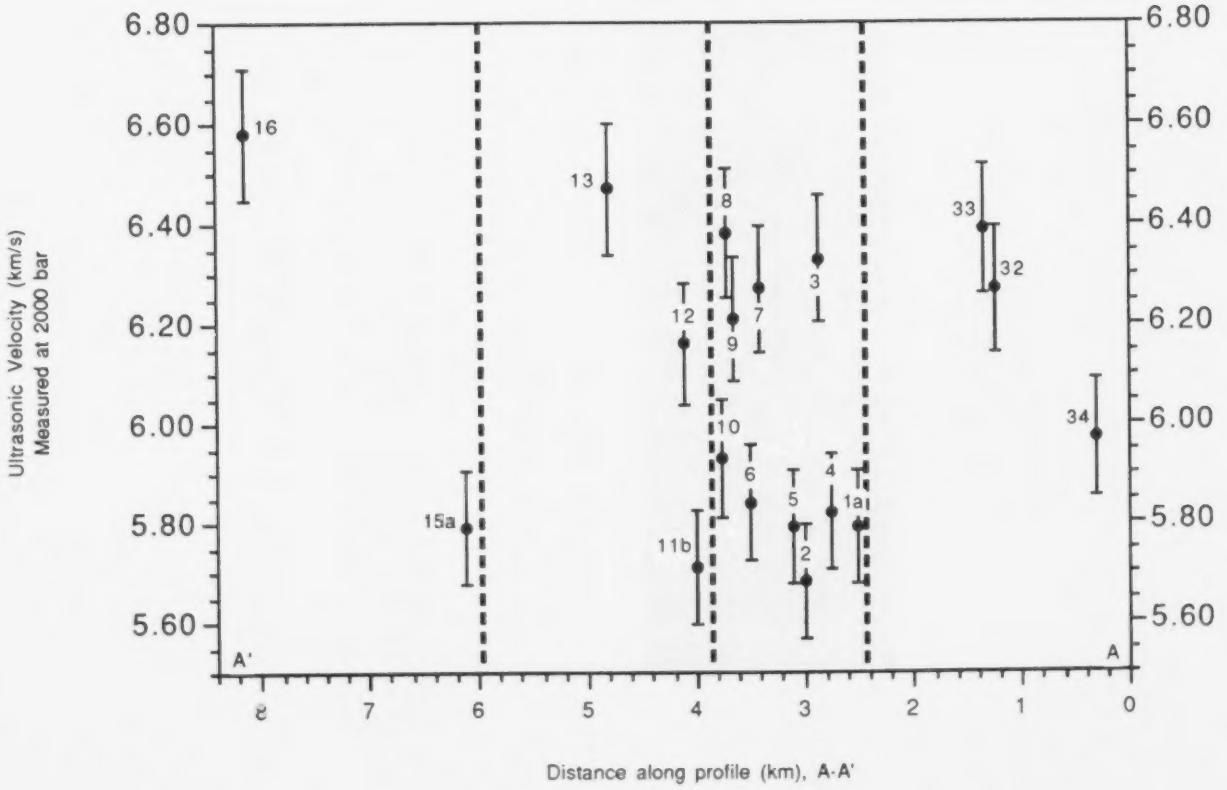

Figure 4.8 . Velocities for cores aligned perpendicular to foliation vs. position along seismic profile. Distances are measured along highway 106 relative to the metasediment contact on the east side of the easterly granodioritic pluton. The shaded area represents the metasedimentary band and the dashed lines represent the shear zones. Vertical velocity errors are shown on the labeled cores.

Table 8 Reflections associated with the Granodioritic sample 15a

Sample	Modal Composition (%)			Velocity (km/s)	Impedance ($kgm^{-2}s^{-1}$)
	Quartz	Biotite	Plagioclase	@ 2000 bars	@ 2000 bars
16	17.6	0.1	69.0	6.58	1.77×10^7
15a	6.6	10.1	60.1	5.79	1.55×10^7
13	23.6	4.2	61.3	6.47	1.71×10^7

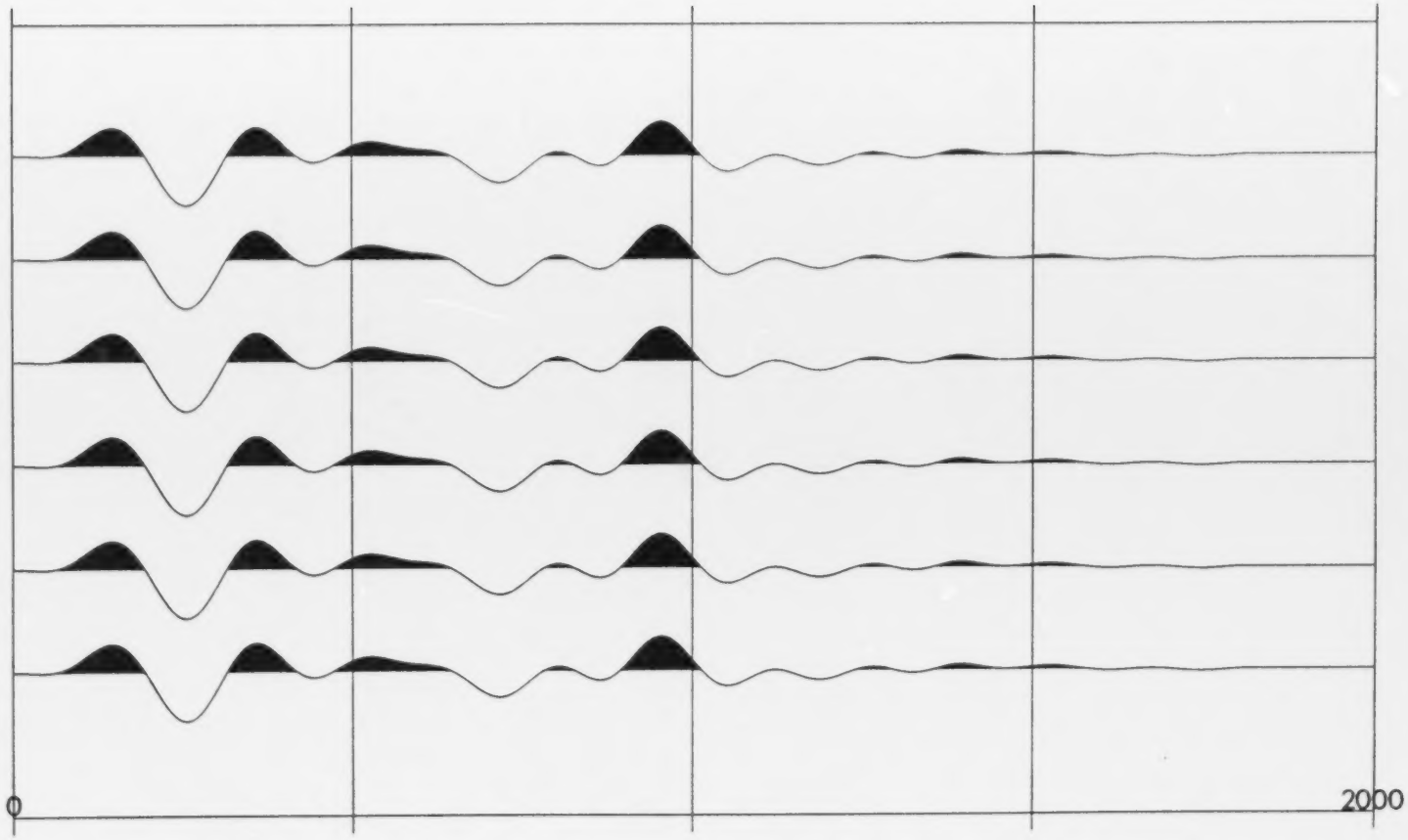

Figure 4.9 . Sythnthetic seismogram I. Klauder wavelet (12 to 56Hz range) convolved with the reflection profile of Table 6. Time graduations in 500 milliseconds intervals.

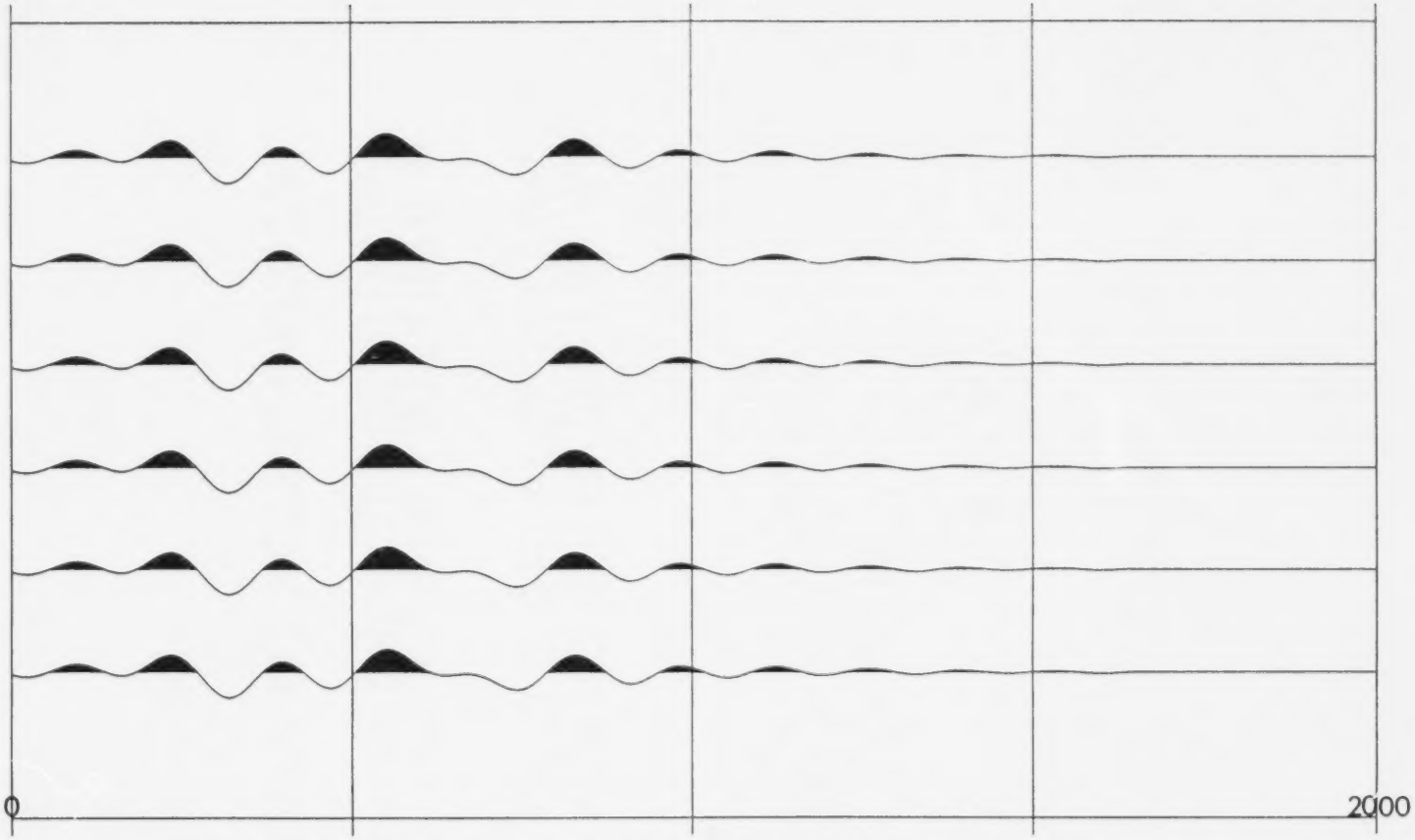

Figure 4.10 . Sythnthetic seismogram II. Klauder wavelet (12 to 56Hz range) convolved with the reflection profile of Table 9. Time graduations in 500 milliseconds intervals.

Table 9 Velocity and reflection model

Samples used to evaluate velocity and impedance average	Average velocity (km/s) of cores at confining pressures of 2000 bars	Vertical TWTT to reflectors (seconds)	Reflection coefficient
34, 1a	6.11		
		0.330	-0.048
3, 6, 7, 8, 9	6.21		
		0.484	-0.039
10, 11b	5.82		
		0.536	0.040
13, 16	6.53		
		0.762	-0.057
15a	5.79		
		0.790	0.057
13, 16	6.53		

CHAPTER 5

Conclusion

The results of the present study suggest that the strong reflected seismic wave packet "a" seen in figures 1.2 and 4.5 project to impedance contrasts in the locality of CDP 1748 and 1813 within the metasediment units and not at the metasediment granodiorite contacts. Additionally, the reflection package "a" [figure 1.2 and 4.5] contains several interference effects of suitably spaced interfaces between the banded metasedimentary layers, superimposed upon shear induced foliation fabric. Furthermore, three mapped shear zones in the Granite Lake area display a lowering of velocity and impedance towards the proximity of the shear zone in accordance to work done by Rey et al. (1993)

The main points of the seismic section and laboratory results are now discussed.

1) Rey et al. (1993) discuss the lateral extent of shear zones. The paper analyses the effect of ductile shearing on the velocity of the rock, which decreases as the shear strain exhibited in the rock structure increases, with velocity contrasts of up to 11% possible between sheared and unsheared rocks in granitic samples. This compares favorably with the 9% velocity contrasts seen over the metasediment ductile shear zones in the present study. He states that in granitic domains formed at high temperatures (>550°C) stress induced foliation is a consequence of viscosity contrasts between the flowing quartz and feldspar components. This flow regime develops a relatively homogenous strain in the rock and a pervasive foliation with high sample velocity anisotropies; such behavior is seen in the eastern metasedimentary shear zones. At low temperature (<300°C) the brittle nature of the minerals in the rock result in the formation of non-ductile shear zones and

this is the temperature regime at formation of the brittle Granite Lake shear zone located in the western granodiorite pluton.

2) The eastern ductile shear zone is located within the metasediments. The effects of this shear zone was apparent in the velocities of five samples over a 350 m distance within a single metasedimentary unit. The mineralogy was relatively constant for these 5 samples (1a, 2, 3, 4 and 5) yet the velocity and impedance response varied substantially. The three rocks nearest the shear zone (3 being the furthest with samples 4 and 1a being progressively nearer) had decreasing velocities and impedances at closer proximity to the shear zone. East of this shear zone, past sample 3, the velocities of the remaining samples 2 and 5 drop to values similar to those found close to the metasedimentary shear zone. These low velocities might indicate the existence of a previously unmapped shear in the locality of sample 5 [figure 1.3] at the contact between the different Mp and Ma metasedimentary units portrayed in figure 1.3 .

3) The central ductile shear zone is associated with rock samples of low velocity and impedance compared to the surrounding metasedimentary rock samples. This variation in acoustic response is difficult to conclusively relate to shear related phenomena as the rock compositions near this zone vary. However, a trend of lowering impedance and velocity occurs amongst samples 12, 11b, 10 and 8, with sample 11b having the lowest velocity and impedance values and is closest to the shear zone. The velocity change between those rocks nearest and those farthest from the shear zone (11b and 8) is 9%; this change compares favorably to the 11% maximum described by Rey et al. (1993) in a similarly sheared rock.

4) The granodioritic surface sample 15a occurs at a brittle shear zone [figure 1.3] which may also appear as a coherent reflector in the seismic record. Figure 4.5 displays a

reflector "s" which extrapolates at the surface to common depth point 1850 a distance of 400 m from the Granite Lake shear zone [figure 1.3]. This reflection also appears to merge with the metasedimentary reflector "a" at depths of 0.5 seconds two way travel time.

This brittle shear zone was formed during the D7 tectonic phase after the ductile D3-D6 events, with the latter deformations determining the present orientation of the metasedimentary structures. Therefore, since the ductile and brittle deformations occured at different times it is likely that the left lateral Granite Lake shear zone dips at an angle with respect to the metasedimentary layers.

Laboratory measurements of the impedance of the Granite Lake shear zone, represented by granodiorite sample 15a is compared to the surrounding granodiorite body represented by samples 13 and 16 which yields substantial reflection coefficients of -0.5 and 0.7 well above the theoretical criterion of 0.036 described by Rey et al. (1993), required to resolve a seismic reflection above the background noise.

5) The predominant seismic wavelength of the vibrator input source is 150 m [section 2.10]. This is comparable to normal widths of the different metasediment bands [figure 1.3] which vary from 45 to 260 m. These interfaces, due to their different compositions and origins, have varying impedances and display reflection contacts spaced by more than 39 m satisfying the Rayleigh resolution of the seismic wavelet [section 2.10]. Furthermore, if the individual reflection coefficients are smaller than the proposed limit of 0.036 [Rey et al. (1993)], reflections off these contacts may still be seen in the seismic section due to interference effects which occur in the parallel banded structure with suitably spaced reflection coefficients. These interference effects may strengthen or weaken the resultant seismic reflected wavelet, potentially displaying a reflector that would otherwise have been to weak to be noticed amongst the noise of the received seismic trace.

6) The seismic profile of figure 1.2 displays parallel oriented structures "a", "b" and "c" dipping gently eastwards to over four seconds two way travel time. The central reflector "a" is continuously 0.22 seconds wide and dips at an angle of 22° from common depth points 1813 to 1650. East of common depth point 1650, the seismic profile turns east-west from its original northeast-southwest orientation. At this point, the structural geological features no longer strike perpendicular to the seismic profile and the seismic reflectors are sampled from an obliquely oriented structural plane. This accounts for reflector "a" having a smaller dip angle from common depth points 1650 onwards [figure 4.7].

One can see that the sampling of the surface rock samples as shown in figure 1.3 is relatively sparse. However, as laboratory measurements are labor intensive only 46 rock cores were measured from 18 samples in this preliminary study. Therefore, only the main geologic areas of the plutons and metasediments were concentrated on, but these measurements appear to have highlighted the main trends in velocity and impedance structure along the profile.

Ideally, core obtained from a wellbore intersecting the dipping structure should be used for these investigations. This would eliminate problems associated with limited outcrop in choosing a representative outcrop for a given geological area. In the present study surface samples were collected from isolated outcrops and these may not always be indicative of the entire geology of the sampled region. As a result, ultrasonic measurements on surface core samples should be considered a first step in the quantitative analysis of a given reflection profile in the absence of a wellbore sonic logs or continuous core.

As this was the first such study in our laboratory, the experimental procedures followed a learning curve that resulted in a improvement in the accuracy of the ultrasonic

velocity to a final, conservatively estimated, value of 2%. Further improvements in velocity measurements are now possible as a high voltage transducer driver with up to 120 Volts output and faster rise time than the previous ultrasonic pulse source has been recently acquired. The signal to noise ratio in this system is visibly lower than our previous system and the input square wave has more definition, with a fast rise time of 5 ns. Furthermore, different travel time determination techniques may be evaluated in future studies to increase the accuracy of the velocity measurements, with many of the known techniques shown in ASTM standards (1993).

The density measurements in the present study were the largest source of uncertainty and were nominally of the order 4% or less. This problem arises from the non-uniform, non-circular cross section of many cores. In making the simple calculation of bulk density from mass and the volume, as determined from the core dimensions, these diameter variations were of major concern. The Archemedian principle of density measurement was applied to the samples but with little success.

In retrospect, we found that the three shear zones in our region of study had appeared to be related to variations in the seismic impedance structure and in particular to relative impedance lows. Although the present data sampling is admittedly sparse, these observations are in qualitative agreement with the recent work of Rey et al. (1993) who found velocity gradients associated with shear zones.

This thesis has provided a data base of velocity and density data, available for use by seismologists and people working on gravity data in the Trans-Hudson Lithoprobe region. Previous seismic and gravity profiles were based on educated guesses of the rock's physical properties. Now, more representative studies in this region can be performed using the laboratory derived rock property measurements. Further, shear zones which pervade through this region can be seismically constrained as regions of local low velocities. The study of the velocity response of these shear zones has implications for

studies in other sheared regions. Although much of this will apply to basic scientific crustal studies there has lately been much interest in the properties of these shear zones as they are often associated with mineral deposition.

Further work will consist of the following major components. First, a new technique for the velocities on prismatic samples will be undertaken. This will allow the determination of the velocity anisotropy from the same block as opposed to differing cores as in the present configuration. Principles of exploration seismics will also be applied to these samples in the hopes that we will simultaneously be able to extract shear wave properties. Secondly, this region of deformation to the west of Flin Flon is crossed twice by the seismic line. Near to Flin Flon the zone is again crossed nearly perpendicularly. This is of great interest as although these rock types are quite similar, the rocks did not experience as high a level of metamorphism, and consequently studying the structures nearer Flin Flon will essentially simulate measurements from shallower and cooler portions of the crust. Finally, these results will be contrasted with the raw seismic traces (not the final processed versions of figure 1.2) in order to assess quantitatively the relationship between the rock properties and the seismic reflections.

BIBLIOGRAPHY

Ashton K. E. et. al., 1988. Geology, Wildnest Lake area, Saskatchewan. Geological Survey of Canada: open file.

Ashton K. E., 1993. Structure of the southern flank of the Kissetnew gneiss belt in Saskatchewan. LITHOPROBE Trans-Hudson Orogen Transect, Report No. 34.

ASTM, 1993. Standard test method for laboratory determination of pulse velocities and ultrasonic elastic constants of rock[1]. Annual book of ASTM standards: vol 03.03 .

ASTM, 1993. Standard practice for measuring ultrasonic velocity in materials[1]. Annual book of ASTM standards: vol 04.08.

Birch, F., 1960. The velocity of compressional waves in rocks to 10 kilobars, 1. Journal of Geophysical Research, 65: 1083-1960.

Birch, F., 1961.The velocity of compressional waves in rocks to 10 kilobars, 2. Journal of Geophysical Research, 66: 2199-2224.

Burke, M. M. and Fountain, D. M., 1990. Seismic properties of rocks from an exposure of extended continental crust-new laboratory measurements from the Ivera Zone. Techtonophysics, 182: 119-146.

Christensen, N. I., 1965. Compressional wave velocities in metamorphic rocks at pressures to 10 kilobars[1]. Journal of Geophysical Research, 70: 6147-6164.

Christensen, N. I., 1979. Compressional wave velocities in rocks at high temperatures and pressures, critical thermal gradients, and crustal low-velocity zones. Journal of Geophysical Research, 84: 6849-6857.

Christensen, N. I. and Szymanski, D. L., 1988. Origin of Reflections from the Brevard Fault Zone. Journal of Geophysical Research, 93: 1087-1102.

Emiliani, C., 1987. Dictionary of the physical sciences. Oxford University Press.

Fountain, D. M., in press 1993. Eclogite-facies shear zones - deep crustal reflectors? Tectonophysics.

Gordon T. M., et al., 1993. Mineral assemblage and thermobarometric constraints on the temperature-depth history of the Kisseynew and Flin Flon belts, Minitoba. LITHOPROBE Trans-Hudson Orogen Transect Report No. 34.

Hajnal, Z. et. al., submitted 1994. Deep crustal structure of the western Trans-Hudson Orogen (Canada) from seismic reflection data.

Hoffman P. F., 1988. United plates of America. The birth of a craton: early Proterozoic assembly and growth of Laurentia. Ann. Rev. Earth Planet. Sci., 16: 543-603.

Hoffman, P. F., 1989. Precambrian geology and tectonic history of North America. In: (Editors) Bally, A. W. and Palmer, A. R., Geology of North America - An Overview. The Geological Society of America: 447-512.

Hurich, C. A., and Smithson S. B., 1987. Compositional variations and the origin of deep crustal reflections. Earth Planet. Sci. Lett., 85:416-426.

Jones, T. D. and Amos, N. 1982. Seismic velocity and anisotropy in mylonites and the reflectivity of deep crustal fault zones. Geology, 10: 260-263.

Jones, T. D. and Nur, A., 1884. The nature of seismic reflections from deep crustal fault zones. Journal of Geophysical Research, 89: 3153-3171.

Kelfweit, R. S. and Wood, L. C., 1982. The limits of zero-phase wavelets. Geophysics, 47: 1035-1046.

Kerr, P. F., 1977. Optical mineralogy. McGraw-Hill Book Company.

Kranz, R. L., 1983. Microcracks in rocks: a review. Tectonophysics, 100: 449-480.

Lewry J. F. et. al., final revision 1993. Structure of a Paleoproterozoic continent-continent collision zone: a Lithoprobe seismic reflection profile across the Trans-Hudson Orogen, Canada. Special issue Tectonophysics, from the 5th International Conference on Seismic Reflection Probing of the Continents and their Margins.

Lucas, S. B. et. al., 1993. Deep seismic profile across a Proterozoic collision zone: surprises at depth. Nature, 363: 339-342.

Mainprice, D. and Casey, M., 1990. The calculated seismic properties of quartz mylonites with typical fabrics: relationship to kinematics and temperature. Geophys. J. Int.: 103, 599-608.

Press, F. and Seiver, R., 1986. Earth. Fourth edition: pp 247.

Reilly, B. A. et al., 1993. Structural history of the Flin Flon domain in Saskatchewan. LITHOPROBE Trans-Hudson Orogen Transect, Report No. 34.

Rey, P. F., Fountain D. M. and Clement, W. P., in press 1993. P-wave velocity across a non-coaxial ductile shear zone and its associated strain gradient: consequences for upper crustal reflectivity. Journal of Geophysical Research.

Richter, D., and Simmons, G., 1977. Microcracks in crustal igneous rocks: microscopy. In: J. G. Heacock (Editor), The Earth's crust. Am Geophys. Union, Geophys. Monogr., 20 149-180.

Ricker, N., 1953. Wavelet contraction, wavelet expansion and the control of seismic resolution. Geophysics, 18: 769-792.

Rouleau, P. M., 1994. On seismic wave attenuation in an hydrated crust. Ph.D. thesis University of Alberta.

Stacey, F. D., 1992. Physics of the earth: third edition. Brookfield Press.

Stead, D. et al., (1993). Physical properties of rocks from the Trans-Hudson Orogen--An update. LITHOPROBE Trans-Hudson Orogen Transect, Report No. 34.

Teufel, W. aand Warpinski, N. R., 1984. Determination of in situ stress from anelastic strain recovery measurements of oriented core: a comparison to hydraulic fracture stress

measurements in the Rollins sandstone, Piceance basin, Colorado. Rock mechanics in Producing and Production Procedures. 25th U. S. Symposium on Rock Mechanics, Chapter 19.

Velzeboer, C. J., 1981. The theoretical seismic reflection response of sedimentary sequances. Geophysics, 46: 843-853.

Widess, M. B., 1973. How thin is a thin bed? Geophysics, 38: 1176-1180.

Yilmaz, O., 1993. Seismic data processing. Society of Exploration Geophysicists.

Zisman, W. A., 1933b. Compressibility and anisotropy of rocks at and near the earth's surface. Proc. Natl. Acad. Sci. U. S., 19: 666-679.

APPENDIX

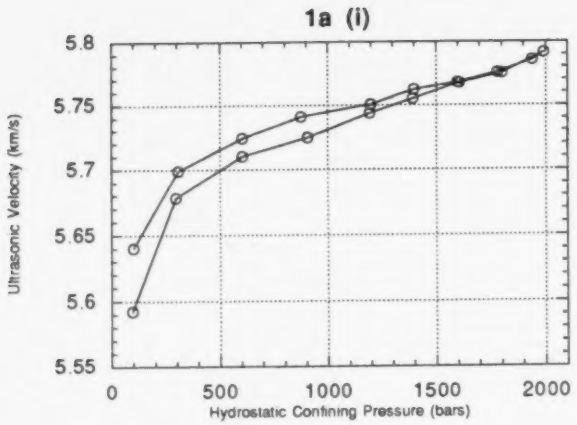
1a (i)
Ultrasonic Velocity (km/s)
5.8
5.75
5.7
5.65
5.6
5.55
0
500
1000
1500
2000
Hydrostatic Confining Pressure (bars)

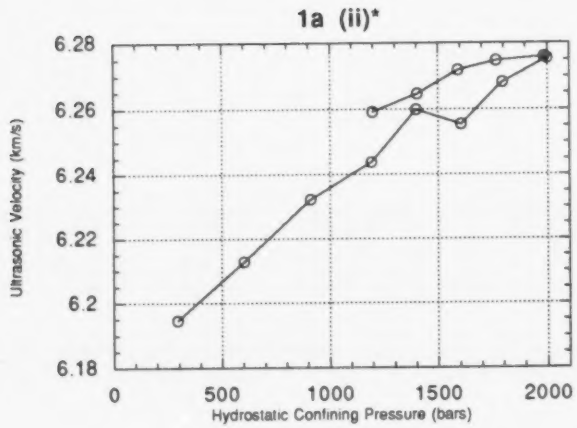
1a (ii)*
Ultrasonic Velocity (km/s)
6.28
6.26
6.24
6.22
6.2
6.18
0
500
1000
1500
2000
Hydrostatic Confining Pressure (bars)

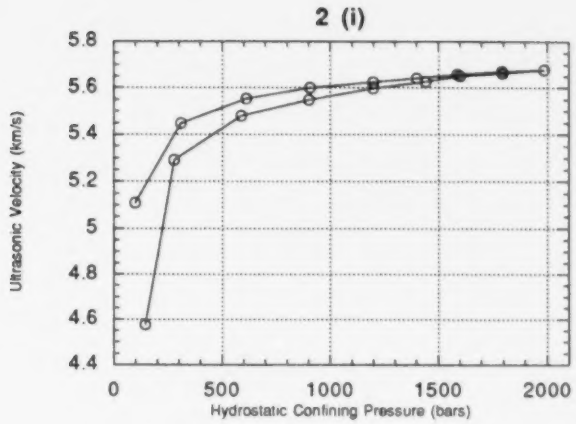
2 (i)
Ultrasonic Velocity (km/s)
5.8
5.6
5.4
5.2
5
4.8
4.6
4.4
0
500
1000
1500
2000
Hydrostatic Confining Pressure (bars)

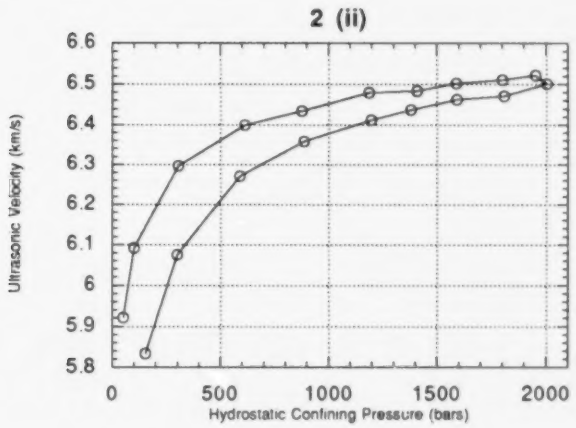
2 (ii)
Ultrasonic Velocity (km/s)
6.6
6.5
6.4
6.3
6.2
6.1
6
5.9
5.8
0
500
1000
1500
2000
Hydrostatic Confining Pressure (bars)

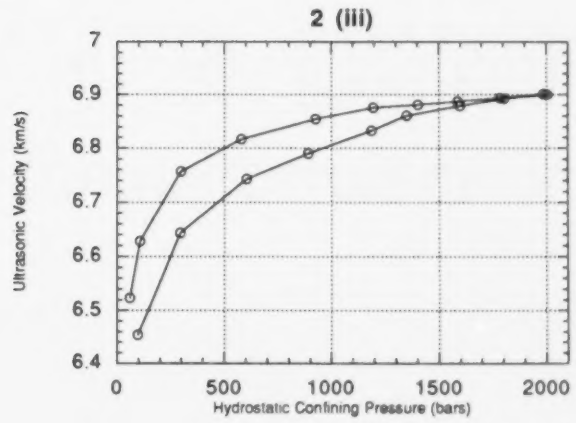
2 (iii)
Ultrasonic Velocity (km/s)
7
6.9
6.8
6.7
6.6
6.5
6.4
0
500
1000
1500
2000
Hydrostatic Confining Pressure (bars)

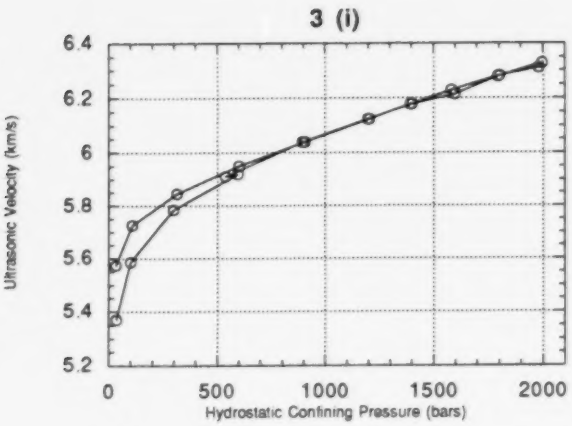
3 (i)
Ultrasonic Velocity (km/s)
6.4
6.2
6
5.8
5.6
5.4
5.2
0
500
1000
1500
2000
Hydrostatic Confining Pressure (bars)

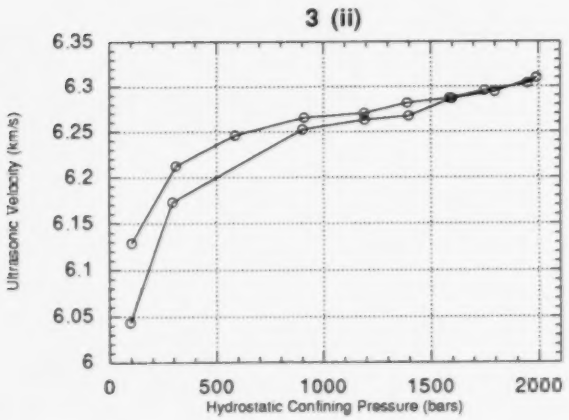
3 (ii)
Ultrasonic Velocity (km/s)
6.35
6.3
6.25
6.2
6.15
6.1
6.05
6
0
500
1000
1500
2000
Hydrostatic Confining Pressure (bars)

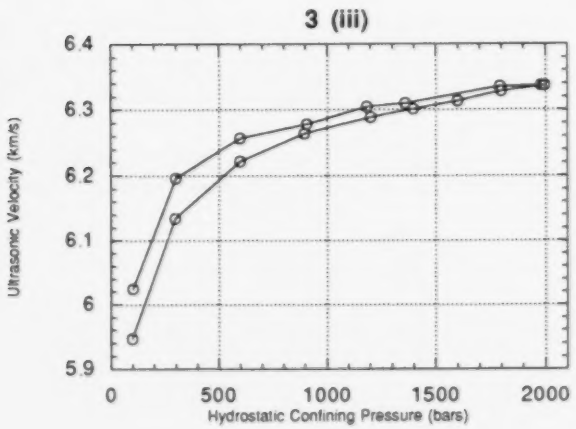
3 (iii)
Ultrasonic Velocity (km/s)
6.4
6.3
6.2
6.1
6
5.9
0
500
1000
1500
2000
Hydrostatic Confining Pressure (bars)

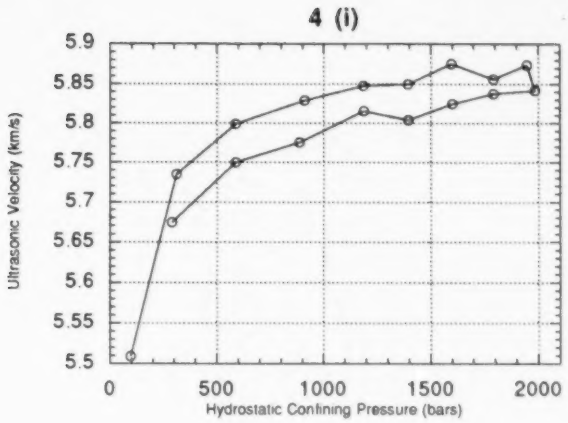
4 (i)
Ultrasonic Velocity (km/s)
5.9
5.85
5.8
5.75
5.7
5.65
5.6
5.55
5.5
0
500
1000
1500
2000
Hydrostatic Confining Pressure (bars)

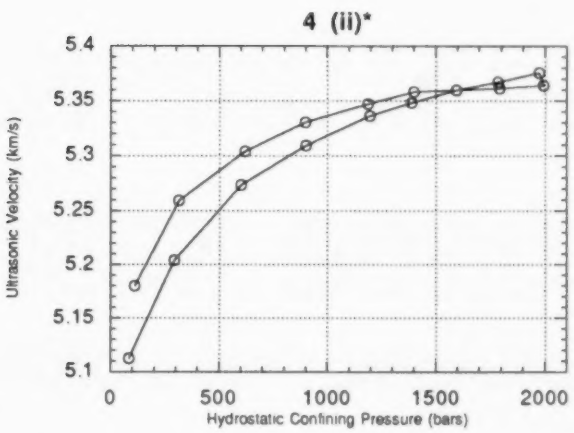
4 (ii)*
Ultrasonic Velocity (km/s)
5.4
5.35
5.3
5.25
5.2
5.15
5.1
0
500
1000
1500
2000
Hydrostatic Confining Pressure (bars)

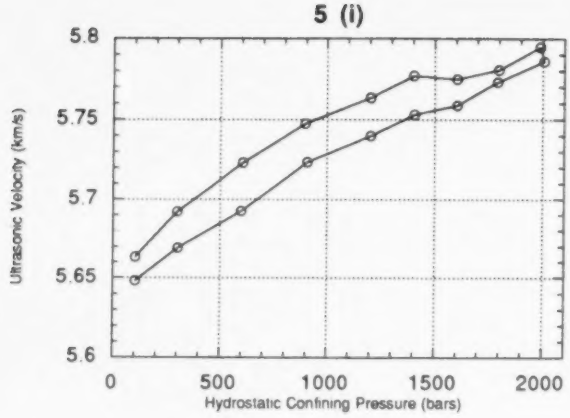
5 (i)
5.8
5.75
5.7
5.65
5.6
Ultrasonic Velocity (km/s)
0
500
1000
1500
2000
Hydrostatic Confining Pressure (bars)

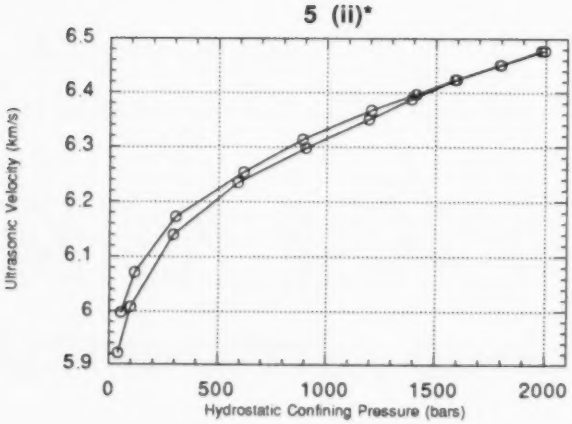
5 (ii)*
6.5
6.4
6.3
6.2
6.1
6
5.9
Ultrasonic Velocity (km/s)
0
500
1000
1500
2000
Hydrostatic Confining Pressure (bars)

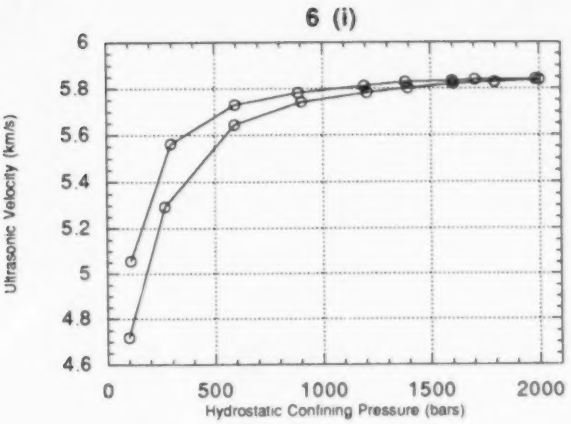
6 (i)
Ultrasonic Velocity (km/s)
6
5.8
5.6
5.4
5.2
5
4.8
4.6
0
500
1000
1500
2000
Hydrostatic Confining Pressure (bars)

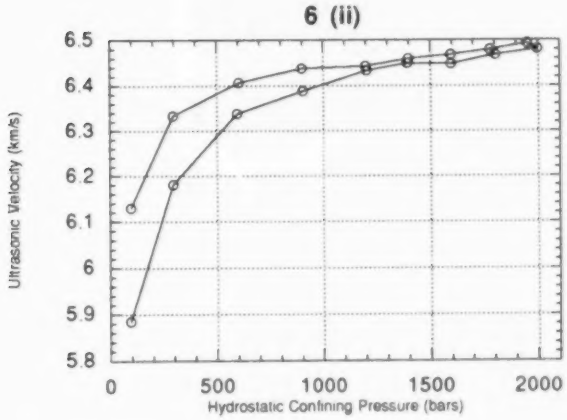
6 (ii)
Ultrasonic Velocity (km/s)
6.5
6.4
6.3
6.2
6.1
6
5.9
5.8
0
500
1000
1500
2000
Hydrostatic Confining Pressure (bars)

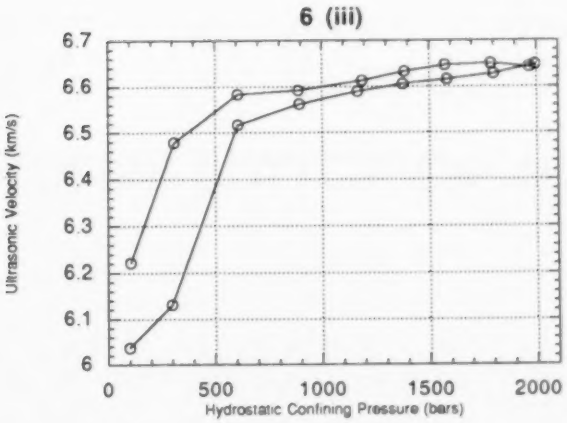
6 (iii)
Ultrasonic Velocity (km/s)
6.7
6.6
6.5
6.4
6.3
6.2
6.1
6
0
500
1000
1500
2000
Hydrostatic Confining Pressure (bars)

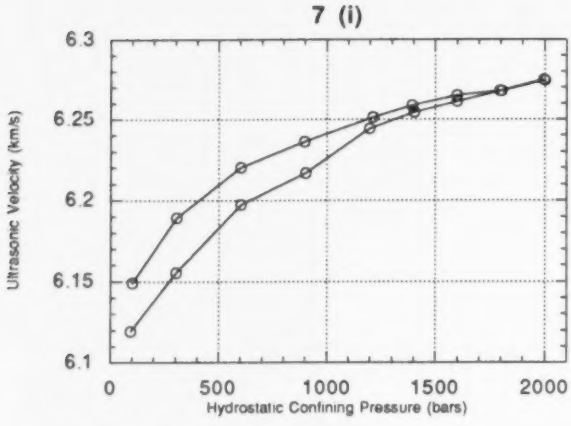
7 (i)
Ultrasonic Velocity (km/s)
6.3
6.25
6.2
6.15
6.1
0
500
1000
1500
2000
Hydrostatic Confining Pressure (bars)

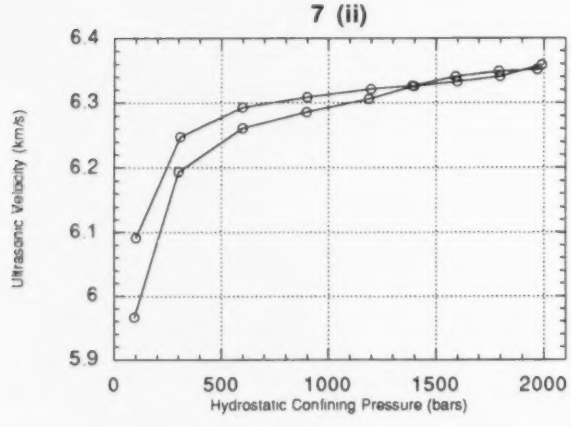
7 (ii)
Ultrasonic Velocity (km/s)
6.4
6.3
6.2
6.1
6
5.9
0
500
1000
1500
2000
Hydrostatic Confining Pressure (bars)

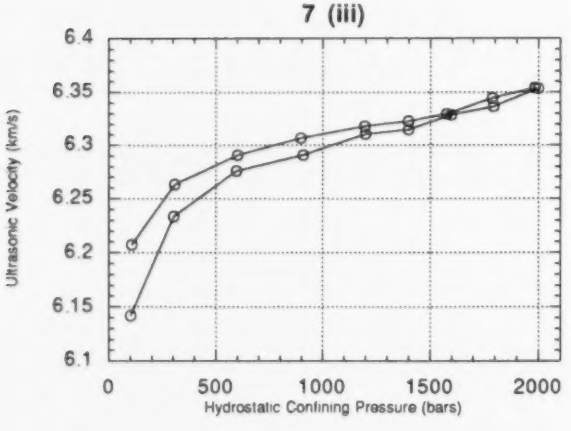
7 (iii)
Ultrasonic Velocity (km/s)
6.4
6.35
6.3
6.25
6.2
6.15
6.1
0
500
1000
1500
2000
Hydrostatic Confining Pressure (bars)

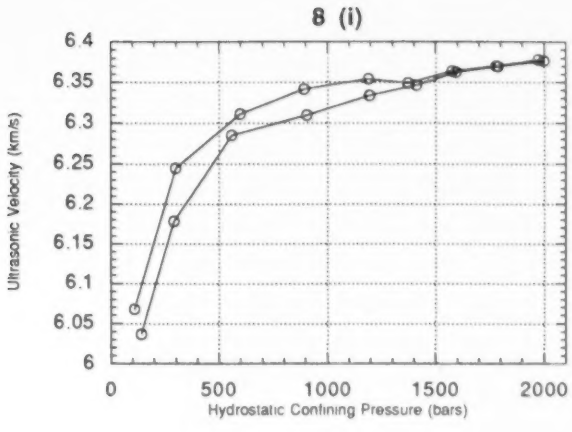
8 (i)
Ultrasonic Velocity (km/s)
6.4
6.35
6.3
6.25
6.2
6.15
6.1
6.05
6
0
500
1000
1500
2000
Hydrostatic Confining Pressure (bars)

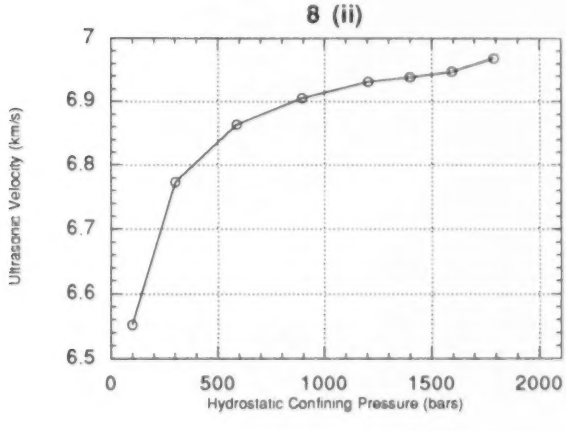
8 (ii)
Ultrasonic Velocity (km/s)
7
6.9
6.8
6.7
6.6
6.5
0
500
1000
1500
2000
Hydrostatic Confining Pressure (bars)

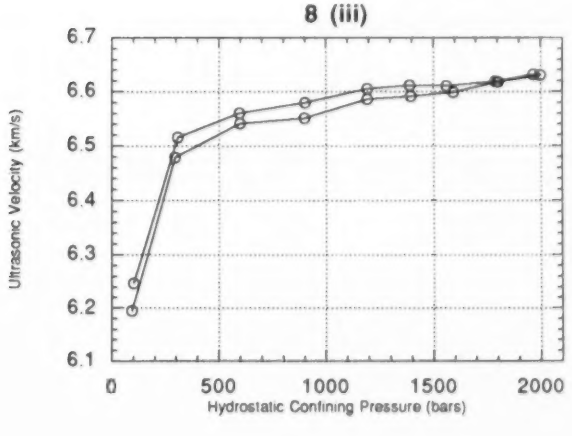
8 (iii)
Ultrasonic Velocity (km/s)
6.7
6.6
6.5
6.4
6.3
6.2
6.1
0
500
1000
1500
2000
Hydrostatic Confining Pressure (bars)

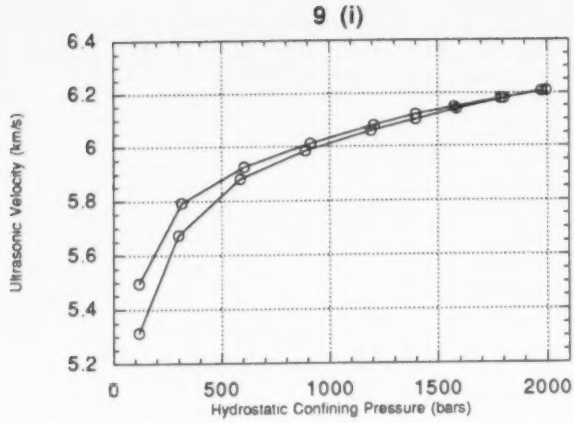
9 (i)
Ultrasonic Velocity (km/s)
6.4
6.2
6
5.8
5.6
5.4
5.2
0
500
1000
1500
2000
Hydrostatic Confining Pressure (bars)

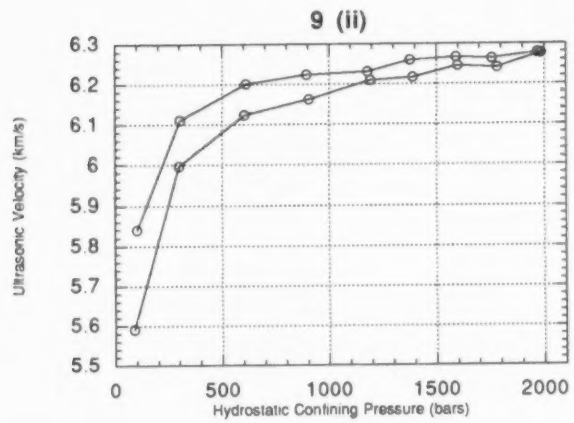
9 (ii)
Ultrasonic Velocity (km/s)
6.3
6.2
6.1
6
5.9
5.8
5.7
5.6
5.5
0
500
1000
1500
2000
Hydrostatic Confining Pressure (bars)

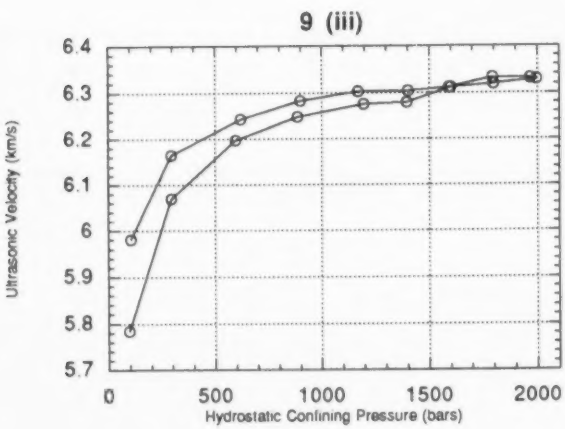
9 (iii)
Ultrasonic Velocity (km/s)
6.4
6.3
6.2
6.1
6
5.9
5.8
5.7
0
500
1000
1500
2000
Hydrostatic Confining Pressure (bars)

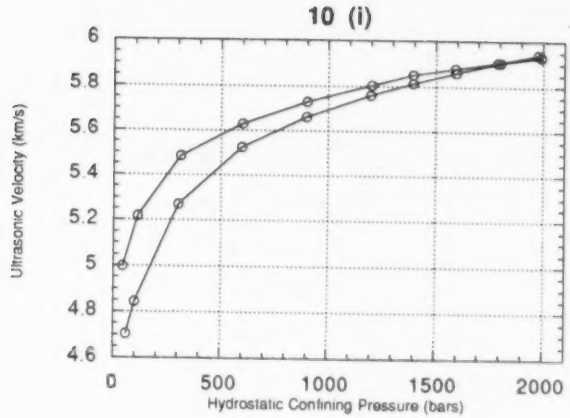
10 (i)
Ultrasonic Velocity (km/s)
6
5.8
5.6
5.4
5.2
5
4.8
4.6
0
500
1000
1500
2000
Hydrostatic Confining Pressure (bars)

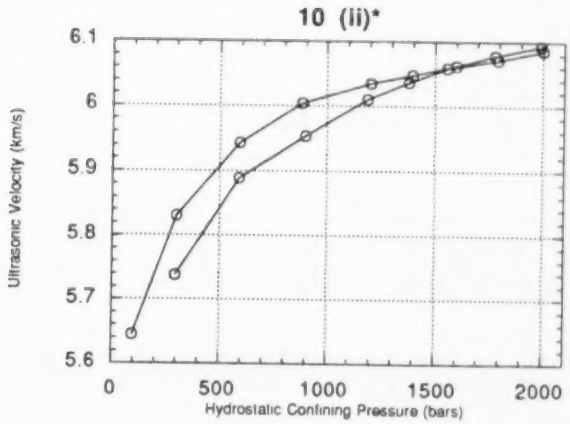
10 (ii)*
Ultrasonic Velocity (km/s)
6.1
6
5.9
5.8
5.7
5.6
0
500
1000
1500
2000
Hydrostatic Confining Pressure (bars)

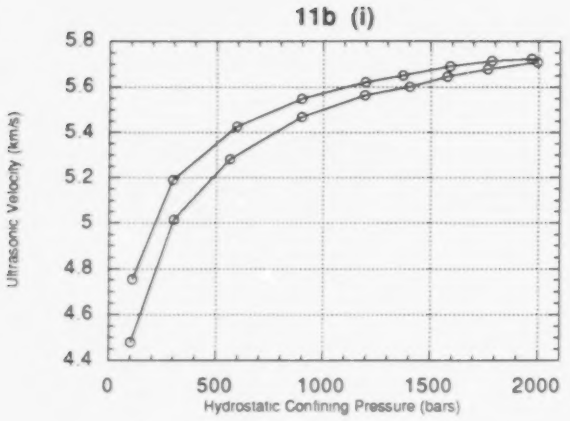
11b (i)
Ultrasonic Velocity (km/s)
5.8
5.6
5.4
5.2
5
4.8
4.6
4.4
0
500
1000
1500
2000
Hydrostatic Confining Pressure (bars)

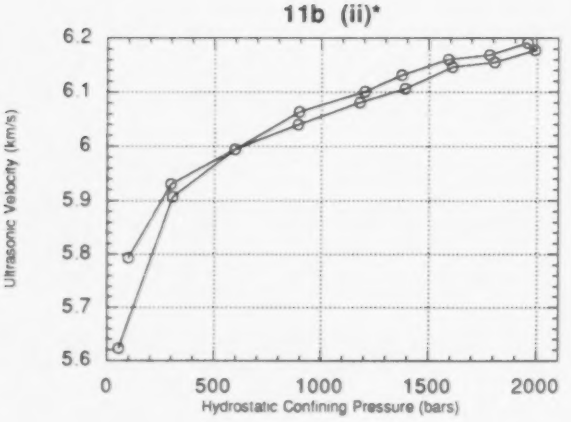
11b (ii)*
Ultrasonic Velocity (km/s)
6.2
6.1
6
5.9
5.8
5.7
5.6
0
500
1000
1500
2000
Hydrostatic Confining Pressure (bars)

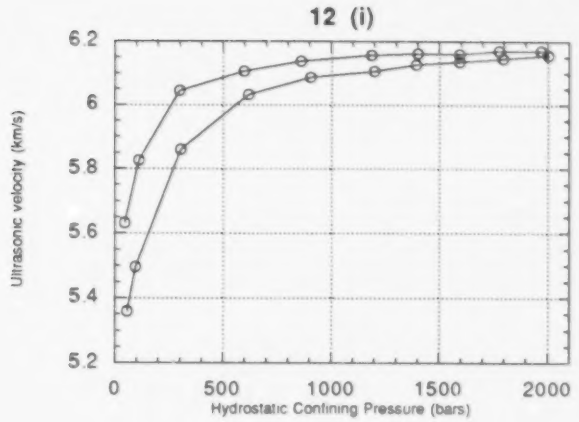
12 (i)
Ultrasonic velocity (km/s)
6.2
6
5.8
5.6
5.4
5.2
0
500
1000
1500
2000
Hydrostatic Confining Pressure (bars)

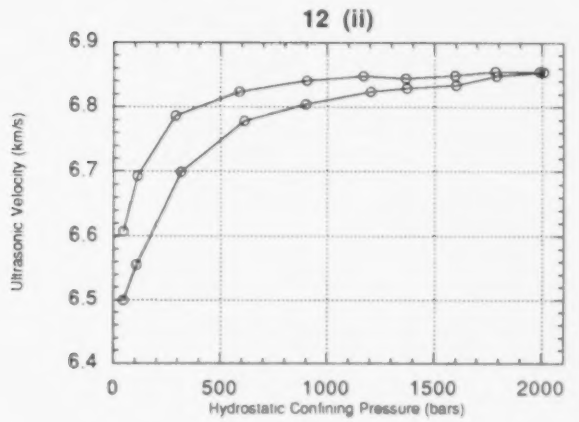
12 (ii)
Ultrasonic Velocity (km/s)
6.9
6.8
6.7
6.6
6.5
6.4
0
500
1000
1500
2000
Hydrostatic Confining Pressure (bars)

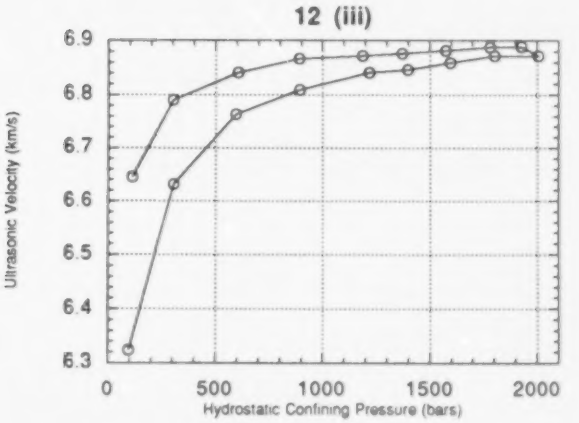
12 (iii)
Ultrasonic Velocity (km/s)
6.9
6.8
6.7
6.6
6.5
6.4
6.3
0
500
1000
1500
2000
Hydrostatic Confining Pressure (bars)

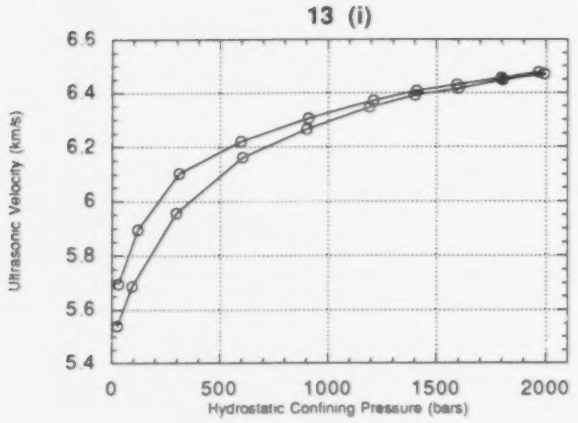
13 (i)
Ultrasonic Velocity (km/s)
6.6
6.4
6.2
6
5.8
5.6
5.4
0
500
1000
1500
2000
Hydrostatic Confining Pressure (bars)

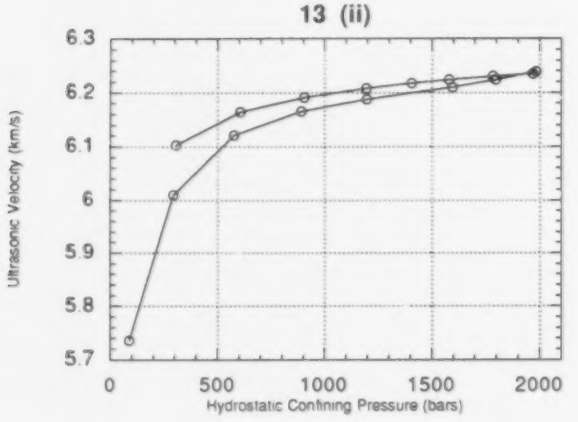
13 (ii)
Ultrasonic Velocity (km/s)
6.3
6.2
6.1
6
5.9
5.8
5.7
0
500
1000
1500
2000
Hydrostatic Confining Pressure (bars)

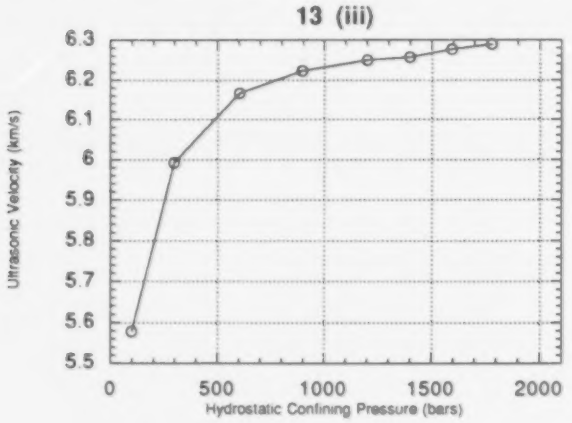
13 (iii)
Ultrasonic Velocity (km/s)
6.3
6.2
6.1
6
5.9
5.8
5.7
5.6
5.5
0
500
1000
1500
2000
Hydrostatic Confining Pressure (bars)

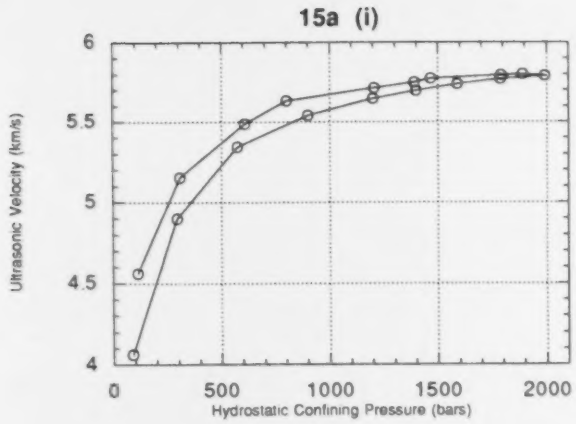
15a (i)
Ultrasonic Velocity (km/s)
6
5.5
5
4.5
4
0
500
1000
1500
2000
Hydrostatic Confining Pressure (bars)

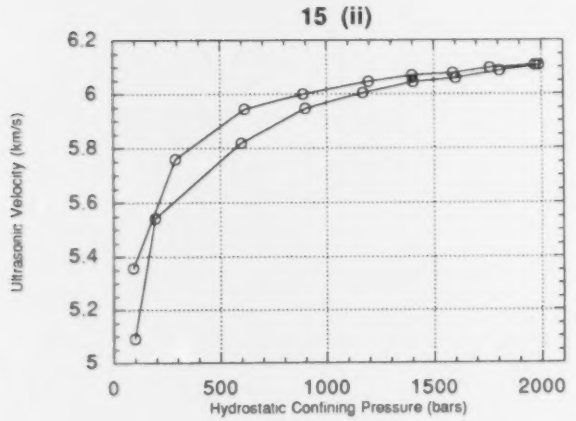
15 (ii)
Ultrasonic Velocity (km/s)
6.2
6
5.8
5.6
5.4
5.2
5
0
500
1000
1500
2000
Hydrostatic Confining Pressure (bars)

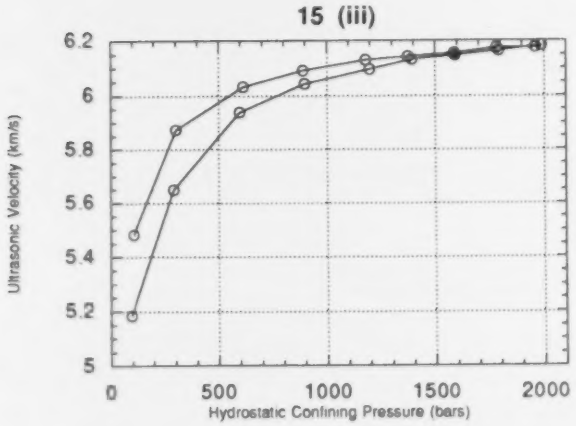
15 (iii)
Ultrasonic Velocity (km/s)
6.2
6
5.8
5.6
5.4
5.2
5
0
500
1000
1500
2000
Hydrostatic Confining Pressure (bars)

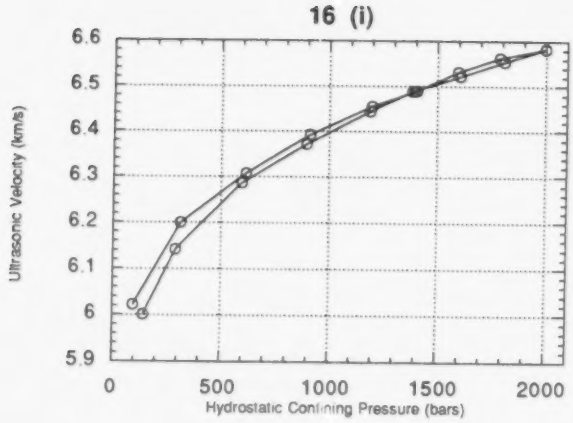
16 (i)
Ultrasonic Velocity (km/s)
6.6
6.5
6.4
6.3
6.2
6.1
6
5.9
0
500
1000
1500
2000
Hydrostatic Confining Pressure (bars)

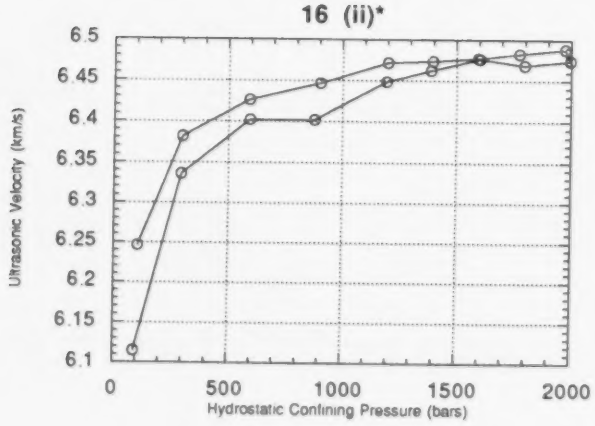
16 (ii)*
Ultrasonic Velocity (km/s)
6.5
6.45
6.4
6.35
6.3
6.25
6.2
6.15
6.1
0
500
1000
1500
2000
Hydrostatic Confining Pressure (bars)

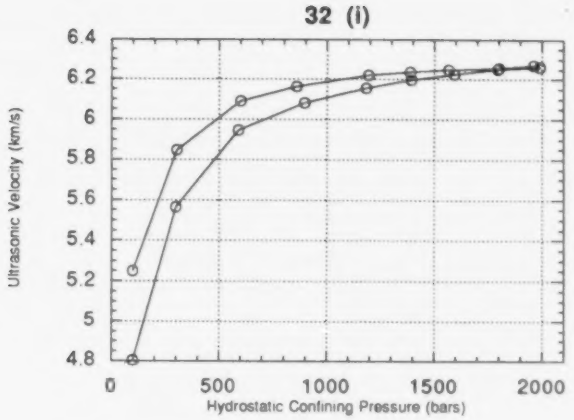
32 (i)
Ultrasonic Velocity (km/s)
6.4
6.2
6
5.8
5.6
5.4
5.2
5
4.8
0
500
1000
1500
2000
Hydrostatic Confining Pressure (bars)

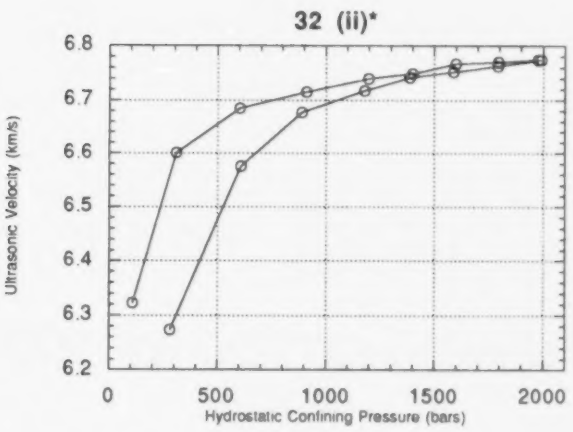
32 (ii)*
Ultrasonic Velocity (km/s)
6.8
6.7
6.6
6.5
6.4
6.3
6.2
0
500
1000
1500
2000
Hydrostatic Confining Pressure (bars)

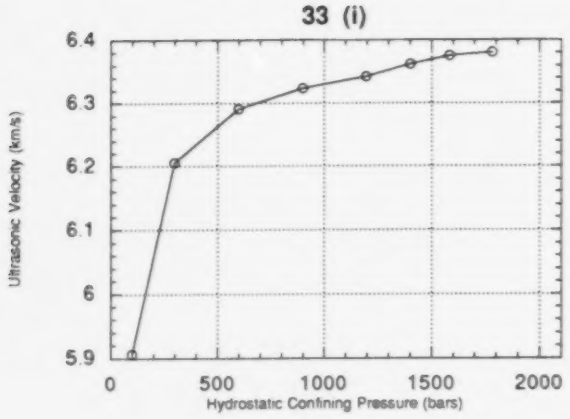
33 (i)
Ultrasonic Velocity (km/s)
6.4
6.3
6.2
6.1
6
5.9
0
500
1000
1500
2000
Hydrostatic Confining Pressure (bars)

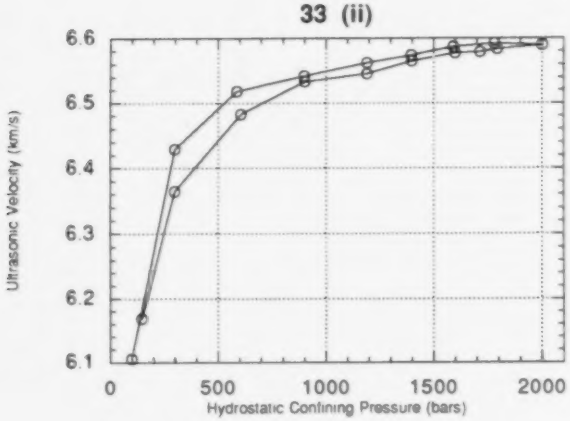
33 (ii)
Ultrasonic Velocity (km/s)
6.6
6.5
6.4
6.3
6.2
6.1
0
500
1000
1500
2000
Hydrostatic Confining Pressure (bars)

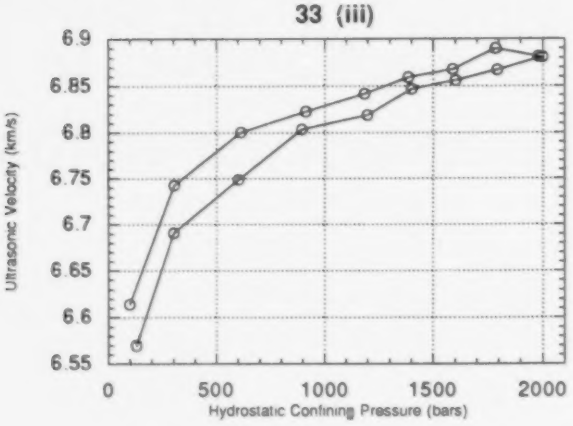
33 (iii)
Ultrasonic Velocity (km/s)
6.9
6.85
6.8
6.75
6.7
6.65
6.6
6.55
0
500
1000
1500
2000
Hydrostatic Confining Pressure (bars)

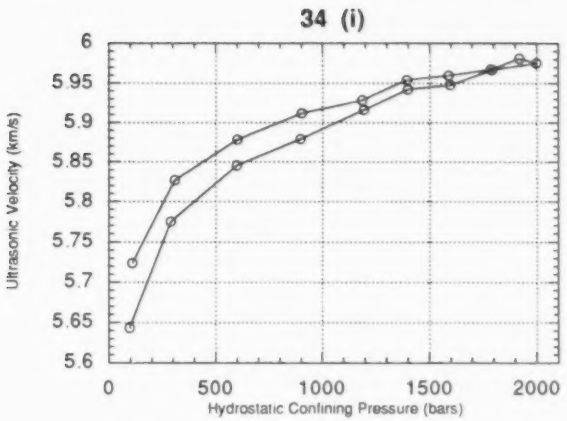
34 (i)
Ultrasonic Velocity (km/s)
6
5.95
5.9
5.85
5.8
5.75
5.7
5.65
5.6
0
500
1000
1500
2000
Hydrostatic Confining Pressure (bars)

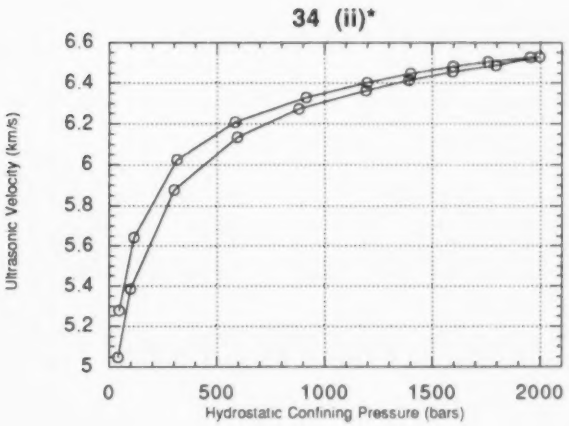
34 (ii)*
Ultrasonic Velocity (km/s)
6.6
6.4
6.2
6
5.8
5.6
5.4
5.2
5
0
500
1000
1500
2000
Hydrostatic Confining Pressure (bars)